Anelastic Strain Recovery Method for In-situ Stress Measurements:

A novel analysis procedure based on Bayesian statistical modeling and application to active fault drilling

2021

Tatsuhiro Sugimoto

Abstract

The in-situ stress state in the earth's crust is a vital parameter in various fields of geoengineering and geosciences, such as resource engineering and structural geology. Various methods have been applied to determine the crustal stress. The anelastic strain recovery (ASR) method is used to measure the three-dimensional in-situ stress and can be applied to deep drilling up to approximately 10 km. The ASR method has been used in previous studies, yielding numerous successful results.

The ASR method is mostly applied for sandstone and mudstone, and the range of applicable rock types has not yet been sufficiently confirmed. Additionally, the existing ASR analysis method requires several assumptions for the measurement, but their validity has not been sufficiently verified. Furthermore, the measurement accuracy has not yet been quantitatively evaluated.

To address these challenges, in this thesis, the conventional stress measurement technique using ASR data is applied to rock types other than sandstone and mudstone in active fault drilling. A novel analysis procedure of ASR data based on Bayesian statistical modeling was proposed, and a core sample reorientation method capable of evaluating the reorientation quality was proposed.

A novel reorientation method is proposed to evaluate the accuracy of the reorientation results. This method involved cutting out nine specimens from a single core sample and measuring their remanent magnetization to evaluate the reliability of the results. The results obtained by this method indicate the possibility of assessing the influence of drilling on the reorientation processes.

A novel analysis procedure based on Bayesian statistical modeling for the ASR analysis is proposed to quantitatively determine the uncertainty of stress measurement. The validity of the procedure was verified using the simulated ASR data. The results show that the uncertainty of the diagonal component of the stress tensor is larger than that of the non-diagonal component. Sensitivity analysis was conducted to investigate this difference. The results of the sensitivity analysis indicated a certain correlation between the sensitivity of the parameter and the uncertainty of the parameter inference.

The proposed ASR procedure is also applied to real ASR data to confirm its applicability. Markov chain Monte Carlo (MCMC) simulations converged for all inferred parameters of all the samples analyzed in this study. The principal stress orientations as a result of stress measurements by hydraulic fracturing and borehole breakout methods are compared with those obtained by the novel procedure; similar results are obtained by all three methods. Additionally, the comparison of the magnitude of minimum horizontal principal stress obtained by the hydraulic fracturing method with the results obtained by the novel procedure also shows consistent results. These results indicate that this method can be applied to real ASR data.

Stress measurements using the conventional ASR method were conducted near the Futagawa Fault, one of the source faults of the 2016 Kumamoto earthquakes. The measurements were successfully conducted on six rock core samples, including a conglomerate rock. The results indicate that the normal faulting stress regime is dominant near the Futagawa Fault. The results indicating that the post-earthquake stress state is the normal faulting stress regime is consistent with those of stress measurements in the area, which were obtained using hydraulic fracturing and focal mechanism analysis. Furthermore, the direction of minimum horizontal principal stress is almost orthogonal to the strike of the Futagawa Fault, indicating that the horizontal shear stress that causes lateral slip on the fault plane is small.

The novel ASR analysis procedure proposed and the results obtained in this study are expected to contribute to research and practice in various fields of earth engineering, such as underground resource development and an array of earth science fields, such as structural geology.

Acknowledgements

This thesis is the summary of my five-year study in my master and Ph. D. course in Kyoto University. Throughout the writing of this thesis I have received a great deal of support and assistance.

First of all, I greatly acknowledge my supervisor Prof. Weiren Lin. He introduced me ASR method for in situ stress measurements. He gave me fruitful advices and helps on my research. I learned a lot from him and the opportunities he provided with me. Without his help, I am not hear.

I would like to acknowledge Prof. Eiichi Fukuyama and Assoc. Prof. Sumihiko Murata for reviewing my thesis and providing me with a lot of insightful comments and suggestions.

I would also like to thank Asst. Prof. Kazuya Ishitsuka. He introduced me a new tool, Bayesian statistical modeling, which let me move on to a new stage of my research. He also reviewed my thesis and provided me with many insights. Without his help, I could not complete my thesis.

I would like to appreciate Prof. Yuhji Yamamoto at Kochi University for his support on conducting remanent magnetization measurements and analyzing the results. I also like to thank Prof. Yuzuru Yamamoto at Kobe University. The core samples used for core's reorientation researches were collected mainly by him.

I would like to acknowledge Dr. Osamu Tadai at Marin Works Japan. He trained me how to prepare samples and conduct experiments. Thanks to his support, my time in Kochi has been a fruitful one. He is one of my best tutors.

I have to appreciate Susumu Shibutani for his support on conducting ASR measurements. He also gave me a lot of suggestions in discussing ASR results. His support at the drilling site was invaluable.

I am grateful to Dr. Nana Kamiya for her advice about my doctoral program. I really appreciate Maki Kataoka for her encouragement and support of my life in Katsura Campus. I would like to thank all the past and present members of the laboratory for giving me a wonderful time.

Last but not least, I would like to express my best thankfulness to my father, mother and brother. They have supported me in so many ways.

2021

Tatsuhiro Sugimoto

Contents

Abstract i

Acknowledgements iii

Contents v

List of Figures viii

List of Tables xiii

Chapter 1 Introduction 1

1.1 Motivation 1

1.2 Outline of the thesis 1

Chapter 2 Review of In-situ Stress Measuring Methods 9

2.1 Why in-situ stress measurements? 9

2.2 Methods of in-situ stress measurements 14

2.2.1 Core-based method 14

2.2.2 Non core-based method 19

Chapter 3 Anelastic Strain Recovery Method for In-situ Stress Measurement 34

3.1 History of ASR method 34

3.2 Constitutive equation of ASR 35

3.3 Determination of in-situ Stress Tensor 41

3.3.1 Orientation of principal stresses 41

3.3.2 Magnitude of principal stresses 43

3.4 Challenges of the ASR method 44

Chapter 4 Core's Reorientation Based on Natural Remanent Magnetization 50

4.1 Introduction 50

4.2 Background 51

4.2.1 Geomagnetism 51

4.2.2 Natural remanent magnetization (NRM) 52

4.2.3 Demagnetization 54

4.3 Methodology 56

4.3.1 Sample preparation 57

4.3.2 Demagnetization and measurement of remanent magnetization 58

4.3.3 Determination of rank of reorientation result 59

4.4 Application to sedimentary soft rock sample 60

4.4.1 Sample information 60

4.4.2 Result 62

4.4.3 Assessment of drilling influence 69

4.5 Summary 70

Chapter 5 A Novel analyzing procedure of ASR Method: Theory 74

5.1 Introduction 74

5.2 Bayesian statistical modeling 75

5.3 Novel ASR method analytic procedure 77

5.4 Simulated ASR data 82

5.5 Results of novel procedure 85

5.6 Sensitivity analysis 90

5.7 Summary 93

Chapter 6 A Novel Analyzing Procedure of ASR Method: Application 97

6.1 Introduction 97

6.2 Core sample information 97

6.2.1 Drilling site 97

6.2.2 Core samples 100
6.3 ASR data 100
6.4 Probability model used for inference 102
6.4.1 Likelihood function 102
6.4.2 Prior information 103
6.5 Results 103
6.6 Discussion 114
6.7 Summary 117
References 118

Chapter 7 Stress State Around the Source Fault of the 2016 Kumamoto Earthquakes 119

7.1 Introduction 119
7.2 Drilling site 120
7.3 Core samples 121
7.4 Measuring System 124
7.5 Result 128
7.5.1 Result of ASR measurement 128
7.5.2 Orientations of principal stresses 130
7.5.3 Magnitudes of principal stresses 135
7.6 In-situ stress state after 2016 Kumamoto earthquake sequence 138
7.7 Results obtained by the novel analysis procedure 139
7.7.1 Prior information 139
7.7.2 Results of inference 140
7.8 Summary 146

Chapter 8 Conclusions 150

List of Figures

Fig. 1-1 Structure of this thesis. Roman numbers shown in this figure indicate the published, accepted (in-press) and in-preparation papers on these topics mentioned in each chapter (I: Sugimoto et al., 2020; II: Sugimoto et al., in press (a); III: Sugimoto et al., in prep; IV: Sugimoto et al., in press (b)). 6

Fig. 2-1 (a) Plot of vertical stress against depth, z, below the surface; (b) variation of the average horizontal to vertical stress ratio with depth (After Brown & Hoek, 1978). 10

Fig. 2-2 Terminology of in-situ stress. (Modified from Amadei & Stephansson, 1997).. 12

Fig. 2-3 Stress sources composing the tectonic stress. (After Zoback et al., 1989).. 13

Fig. 2-4 Two strain recoveries occuring on a drillied rock core sample: elastic and anelastic strain recoveries. 16

Fig. 2-5 Elastic strain recovery caused by in situ stress release (After Ito et al., 2013). 17

Fig. 2-6 Measuring system of the DCDA method (After Funato & Ito, 2017). 18

Fig. 2-7 Polar coordinate system and the stress elements in this coordinate system. 22

Fig. 2-8 Schematic diagram of the fracture initiated by the pumped fluid. (Modified from Amadei & Stephansson (1997)). 25

Fig. 2-9 Pressure-time and flow rate-time record of the idealized fracturing test (Amadei & Stephansson, 1997). 26

Fig. 2-10 Image of borehole breakout. (a) Section of borehole televiewer log showing zones of borehole breakouts (black batches). (b) Horizontal cross-section of borehole breakout at a depth of 1475.8 m (arrow in (a)). (Modified from Amadei & Stephansson, 1997; Hickman et al. 1985). 27

Fig. 3-1 Normal strain in an arbitrary direction in a viscoelastic body. n is the

directional cosine vector indicating the direction of the measured strain. 39
Fig. 3-2 Flow chart of the ASR method. (After Matsuki & Takeuchi 1993)..... 46
Fig. 4-1 Definitions of inclination and declination. 54
Fig. 4-2 Schematic graph showing progressive demagnetization steps. Two-dot chain lines show primary natural remanent magnetization (NRM). One-dot chain lines show secondary NRM on each demagnetization steps, which are demagnetized in order to extract primary NRM. Black solid lines show sums of primary NRM and secondary NRM (resultant NRM) on each demagnetization steps. Broken lines show demagnetized secondary NRMs. Resultant NRMs are measured on each step and plotted on a Zijderveld diagram..... 55
Fig. 4-3 (a) Projections of NRM onto the horizontal and vertical planes. (b) Schematic diagram of a Zijderveld diagram. The numbers in the figures show the number of steps in demagnetization process. Solid black circles are projections of the end points of the NRM vector onto the horizontal plane and open circles are those onto a vertical plane oriented north-south..... 56
Fig. 4-4 Pictures of sample preparation. (a) A whole round core sample. Strain gages attached to the sample were used for another measurement. (b) A disc-shaped sample cut from a whole round core sample. The numbers show those of specimens used in Fig. 4-9. (c) Specimens wrapped by parafilms. White allow show the direction of the reference line of the whole-round core sample..... 58
Fig. 4-5 2-G Enterprise (Model 760R) at Kochi University, Japan..... 59
Fig. 4-6 Location of the drilling site named C0023A. (After Heuer et al., 2017.). 61
Fig. 4-7 Lithostratigraphy of Hole C0023A and sampling depths. (After Heuer et al., 2017.)..... 62
Fig. 4-8 Zijderveld diagram with the demagnetization results of specimen 1 from sample core-1 in each demagnetization step. Black solid circles represent projections of the end points of the NRM vectors in each demagnetization step onto the horizontal plane, and black open circles are those onto a vertical plane oriented north-south. Gray circles (both solid and open) show the secondary components of the NRM vector. The vector length represents the magnetization

magnitude. The two black dashed lines in the figure are regression lines fitted to the primary NRM. 63
Fig. 4-9 Zijderveld diagrams of NRM obtained from Core-1. The numbers show those of the specimens. 65
Fig. 4-10 Zijderveld diagrams of NRM obtained from Core-6. 66
Fig. 4-11 Zijderveld diagrams of NRM obtained from Core-4. 67
Fig. 4-12 Equal area projections of the primary components of the normalized NRM vectors for (a) Core-1, which has rank A, (b) Core-6, which has rank B and (c) Core-4, which has rank C, respectively. Black solid and open circles indicate lower and upper hemisphere projections, respectively. Gray circles (solid and open) indicate specimens that were not used for averaging. Triangles show the averaged direction using the results from specimens, except..... 68
Fig. 5-1 (a) Real anelastic normal strain recovery data measured on a sedimentary rock core collected in the eastern Nankai Trough (Modified from Nagano et al. 2014). The labels (*xx*, *xy*, and so on) indicate the nine directions in which anelastic normal strains were measured and correspond to those shown in (b). The temperature of the measured rock core is also shown. (b) Nine directions in which anelastic normal strains are measured with strain gauges. The directions of ±*xy*, ±*yz*, and ±*zx* are tilted at 45 degrees with respect to those of *xx*, *yy*, and *zz*. 78
Fig. 5-2 Flow chart showing the concept of proposed analytic procedure. 82
Fig. 5-3 Simulated ASR data developed by using (5-5) and values shown in Table 5-1. The labels (*xx*, *xy*, and so on) correspond to those shown in Fig. 5-1 (b). 83
Fig. 5-4 Results of inference for $\sigma 11$ in Case-1. (a) Three Markov chains with different initial values. Each chain consists of 1500 samples. (b) Marginal posterior distribution obtained from three chains in (a). 86
Fig. 5-5 Results of inference for $\sigma 12$ in Case-1. (a) Three Markov chains with different initial values. Each chain consists of 1500 samples. (b) Marginal posterior distribution obtained from three chains in (a). 86

Fig. 5-6 Total sensitivity indices for each parameter in Case-2. (a) Sensitivities calculated using anelastic normal strain recovery in the 92
Fig. 6-1 Maps of the tectonic setting and geological structures around the NFD-1. (a) Tectonic setting of Japanese Islands. (b) Geological map of the northern part of Awaji Island. (c)Location of the NFD-1. (d) Geological section, fracture density and composite logging profiles of NFD-1 (After Nishiwaki & Lin, 2019). 99
Fig. 6-2 ASR data of ASR-17 filtered by simple moving average using 11 data points (depth 710.78 m). 101
Fig. 6-3 Prior distribution of $\sigma 11$ obtained from ASR-17 data. 104
Fig. 6-4 Lower hemisphere equal area projection of the three principal stresses of each sample.....110
Fig. 6-5 Rose diagrams showing S_{Hmax} orientation obtained by the procedure proposed in this study. The north is located $0\circ$.....112
Fig. 6-6 S_{Hmax} orientations obtained by borehole breakout method. (After Nishiwaki et al., 2018). 114
Fig. 6-7 S_{Hmax} orientations obtained by hydraulic fracturing method. (After Kyoto University, 2018). 115
Fig. 7-1 Map around the drilling site. A black circle (FDB) in the figure indicates the location of the borehole, and black and white stars indicate the epicenter of the foreshock (April 14, 2016) and the mainshock (April 16, 2016), respectively. Small circles in the figure indicate the epicenters of earthquakes of magnitude 2.0 or greater that occurred between the mainshock and May 4, 2016. (Modified from Toda et al. 2016). 121
Fig. 7-2 Figure showing the geological column of the FDB. Fault depths and sampling locations are also indicated in Fig. 7-1. The depth of the lithological boundary was confirmed by FDB-1, and fault 598 is the same fault as fault 576, which was confirmed by FDB-1R. (Modified from Shibutani et al., 2021). 123
Fig. 7-3 Schematic diagram of ASR meausring system. 124
Fig. 7-4 ASR measuring system. 125

Fig. 7-5 Nine directions in which anelastic normal strains are measured with strain gauges. 126
Fig. 7-6 Picture of used core sample (FDB-11). 127
Fig. 7-7 Core sample packed by aluminium bag. 127
Fig. 7-8 ASR results for sample FDB-12 (FDB-1 hole, 523.00 m depth). (a) Anelastic normal strain recovery in nine directions and room and water temperatures with time. (b) ASR in the three principal strain directions and mean normal strain direction, as well as changes in room and water temperature with time. 128
Fig. 7-9 Examples of ASR measurement results for which stress analysis was not possible. (a) FDB-02 (FDB-1 hole, depth 336.84 m). (b) FDB-10 (FDB-1 hole, depth 505.53 m). 130
Fig. 7-10 Results of FDB-12(a, b) and FDB-19(c, d) reorientation. (a, c) Projection of the progressive demagnetization onto Zijderveld diagrams. The xx, yy, and zz axes in the figure are those of the core coordinate system shown in Fig. 7-5. The numbers in the figure indicate the number of steps for progressive demagnetization. (b, d) Schmidt net lower hemisphere projection of the orientation results of eight cut-out specimens. The angles in the figure are measured clockwise with the reference line on the core sample set at 0°. Triangles are the average orientation of the eight specimens and circles are the $\alpha 95$ confidence limits. 131
Fig. 7-11 Projection of the principal stress directions. Schmidt net lower hemisphere projection is shown. The three principal stresses and the maximum and minimum horizontal stresses are described in the figure. 134
Fig. 7-12 Lower hemisphere equal area projection of the three principal stresses of each sample. 146

List of Tables

Table 4-1 Results of core reorientation based on the Natural Remanent Magnetization Measurements. 64
Table 5-1 Parameters, values for simulated data, and prior distributions for each case. U[a, b] denotes a uniform distribution from a to b, and N[c, d] denotes a normal distribution with mean c and standard deviation d, respectively. 84
Table 5-2 Results of inference. True values are the same as those shown in Table 5-1. Mean and SD are the mean values and standard deviations calculated using the three chains excluding the warm-up samples. 89
Table 6-1 Core sample information. 100
Table 6-2 Inference results (Part 1). 105
Table 6-3 Inference results (Part 2). 106
Table 6-4 Inference result for the maximum principal stress $\sigma 1$. 107
Table 6-5 Inference result for the intermediate principal stress $\sigma 2$. 108
Table 6-6 Inference result for the minimum principal stress $\sigma 3$. 109
Table 6-7 Inference results of horizontal stresses. 113
Table 6-8 Hydraulic fracturing results obtained in the AFD-1 borehole. (After Yokoyama et al., 2019). 116
Table 7-1 Information of the core samples. 124
Table 7-2 Results of reorientation. 133
Table 7-3 Magnitudes of stresses. 137
Table 7-4 Inference results (Part 1). 141
Table 7-5 Inference results (Part 2). 142
Table 7-6 Inference results for the maximum principal stress. 143
Table 7-7 Inference results for the intermediate principal stress. 144
Table 7-8 Inference results for the minimum principal stress. 145

This page intentionally left blank

Chapter 1

Introduction

1.1 Motivation

The in-situ stress state in the earth's crust is a vital parameter in various fields of geoengineering and geosciences, such as resource engineering and structural geology (Haakon, 2016; Zoback, 2007). Various methods have been proposed to determine the crustal stress, such as the focal mechanism analysis, borehole breakout analysis, hydraulic fracturing method, and methods using core samples (hereinafter called core-based methods) (Amadei & Stephansson, 1997). In general, core-based methods are advantageous in terms of the cost and simplicity of measurement, and their applications have increased in recent years. The anelastic strain recovery (ASR) method, a core-based method, is a three-dimensional stress measurement method that can be applied to deep drilling up to approximately 10 km. The ASR method is mostly applied for sandstone and mudstone, and the range of applicable rock types has not yet been sufficiently confirmed. Additionally, the existing ASR analysis method requires several assumptions in the analysis, but their validity has not been sufficiently verified. In this thesis, the author focuses on solving such problems of the ASR method for its improvement.

1.2 Outline of the thesis

This thesis consists of eight chapters, the outline of which is as follows. Chapter 2 reviews

existing stress measurement methods. A wide range of in-situ stress measurement methods have been proposed so far. Stress measurement methods can be categorized from various perspectives, and in this thesis, the methods are categorized into two groups: "core-based methods" and "non-core methods." The core-based methods include the anelastic strain recovery (ASR) method and the diametrical core deformation analysis (DCDA) method etc., which measure stresses using laboratory tests on drilled rock core samples. Non-core methods include the borehole breakout and drilling induced tensile fracture (DITF) analysis, hydraulic fracturing, and other methods wherein the measurement equipment is lowered into the borehole. The measurement of crustal stress is more difficult and less accurate than that of physical properties such as the strength, elastic modulus, thermal conductivity, and resistivity. Therefore, it is desirable to combine several measurement methods for a certain drilling project. By using the stress measurement methods detailed in this chapter to complement the ASR method, it is possible to obtain more accurate stress measurements.

Chapter 3 describes the basic principles, hypotheses, and theoretical equations of the ASR method, which is a core-based methods and the subject of this study. Subsequently, the existing analytical methods used in previous studies and problems are described in detail. In general, strain recovery occurs in rock core samples immediately after drilling because of the in-situ stress release. Strain recovery can be classified into two categories. The first is the elastic strain recovery that completes instantaneously on stress release. The second is anelastic strain recovery (ASR), which starts on stress release and gradually recovers over several days. As the name suggests, the ASR method is based on the ASR that occurs in drilling core samples. This method has a clear theoretical basis and is highly applicable to large depths up to approximately 10 km, where implementing the non-core method is difficult, and is expected to enable stress measurement in regions with complex stress fields such as subduction zones.

Chapter 4 describes the core reorientation required when using core-based methods. In order to determine the in-situ principal stress directions using core-based methods, the in-situ orientation information of the core sample is required. However, the core sample is rotated during drilling and the orientation information is lost; therefore, it

is necessary to recover the orientation through a process called core reorientation. Rock remanent magnetization, especially natural remanent magnetization (NRM), has been used for core reorientation in previous studies. However, the objective evaluation of the quality of the results cannot be conducted with the reorientation method used in these studies. To rectify this problem, the author proposed a method to cut out nine specimens from a single core sample and measure the remanent magnetization of eight of them to evaluate the reliability of the results. In this chapter, the results of the application of this method to semi-pelagic sediment samples collected off Cape Muroto, Kochi Prefecture, during Expedition 370 of the International Ocean Discovery Program (IODP), were reported. Additionally, the effect of secondary remanent magnetization due to drilling on the orientation of the core was examined, and an approach for data quality evaluation was described. The orientation of core samples is an essential technique not only in the field of stress measurement using core-based methods but also in that of geological structural analysis, and the results of this chapter are expected to have a significant impact.

In Chapter 5, the author proposes a novel analysis method for the ASR method. A problem of stress measurement is the difficulty in evaluating the uncertainty of the measurement results. Uncertainty quantification (UQ) is a potential solution for this problem. Bayesian statistical modeling, which is an uncertainty evaluation method, facilitates the evaluation of uncertainty even with less measurement data by utilizing the information obtained separately from the ASR measurement. Therefore, its effectiveness has been confirmed in fields such as earth and planetary sciences and rock mechanics, where the measurement data generally tends to be scarce. Conversely, no previous studies have been conducted on the application of uncertainty evaluation to stress measurement. In this study, the author aims to develop a new analysis method for the ASR method that can evaluate the uncertainty based on Bayesian statistical modeling. In this chapter, the validity of the novel method is verified using simulated ASR data. The results show that the uncertainty of the diagonal element of the stress tensor is larger than that of the non-diagonal element. Sensitivity analysis was conducted to examine the cause of this phenomenon. By using the method proposed in this chapter, it is possible to quantitatively evaluate the uncertainty of the stress measurement results.

Chapter 6 describes the results of applying the novel analysis procedure described in Chapter 5 to a real ASR dataset. The ASR data used were obtained from eight samples obtained in the vicinity of the Nojima Fault, the source fault of the 1995 Mw 6.9 Kobe earthquake. Markov chain Monte Carlo (MCMC) simulations converged for all the inferred parameters of the eight samples. Borehole breakout analyses and hydraulic fracturing tests were conducted in the same and adjacent boreholes from which the core samples were obtained. A comparison of the direction of maximum horizontal principal stresses showed that all three methods had similar trends. Additionally, a comparison of the minimum horizontal principal stress values obtained by the hydraulic fracturing method and the results of this study also showed similarity. The results of this study indicate that this method can be applied to real data. Further application of this method to other regions and different rock types will be desirable in the future, and verifying the accuracy of the newly proposed method is also necessary.

In Chapter 7, as an example of the application of the ASR method to rocks others than sandstone and mudstone, the results of stress measurements on rocks, including pyroclastic flow deposits and andesite near the Futagawa Fault (the source faults of the 2016 Kumamoto earthquake mainshock), are described. The stress state in the source region is a critical parameter when considering the rupture mechanism and slip behavior of an earthquake's source fault. In this study, the conventional ASR method was applied to a total of 20 rock core samples obtained from boreholes penetrated through the Futagawa Fault, and in-situ stress measurements after earthquakes were successfully conducted on six samples. The results show that a normal faulting stress regime, wherein the vertical stress is the maximum principal stress (σ_1), is dominant near the Futagawa Fault after the earthquake. This suggests that the maximum principal stress, inferred to have been in the horizontal plane before the earthquake, was significantly reduced by the strike-slip faulting movement during the earthquake. The results suggesting that the post-earthquake stress state is a normal faulting stress regime is consistent with those of stress measurements in the area, which were obtained by the hydraulic fracturing and focal mechanism analysis (Kyoto University, 2018; Yoshida et al., 2016; Yu et al., 2019). Additionally, the direction of minimum horizontal principal stress (S_{hmin}) determined

from the ASR measurements is almost orthogonal to the strike of the Futagawa Fault, indicating that the horizontal shear stress causing lateral slip on the fault plane is small.

Finally, in Chapter 8, a summary of this thesis is provided in conclusion. In this study, both experimental and simulation studies were conducted to solve the problems of the existing ASR method. This study suggests that the ASR method can be applied to a wider range of rock types, not limited to sedimentary rocks such as sandstone and mudstone. Additionally, by applying Bayesian statistical modeling to the ASR method, an effective approach to quantitatively evaluate the uncertainty of measurements and significantly improve the reliability of the measurement results was provided for the first time. The results of this study are expected to contribute to research and practice in various fields of earth engineering, such as underground resource development and an array of earth science fields, such as structural geology.

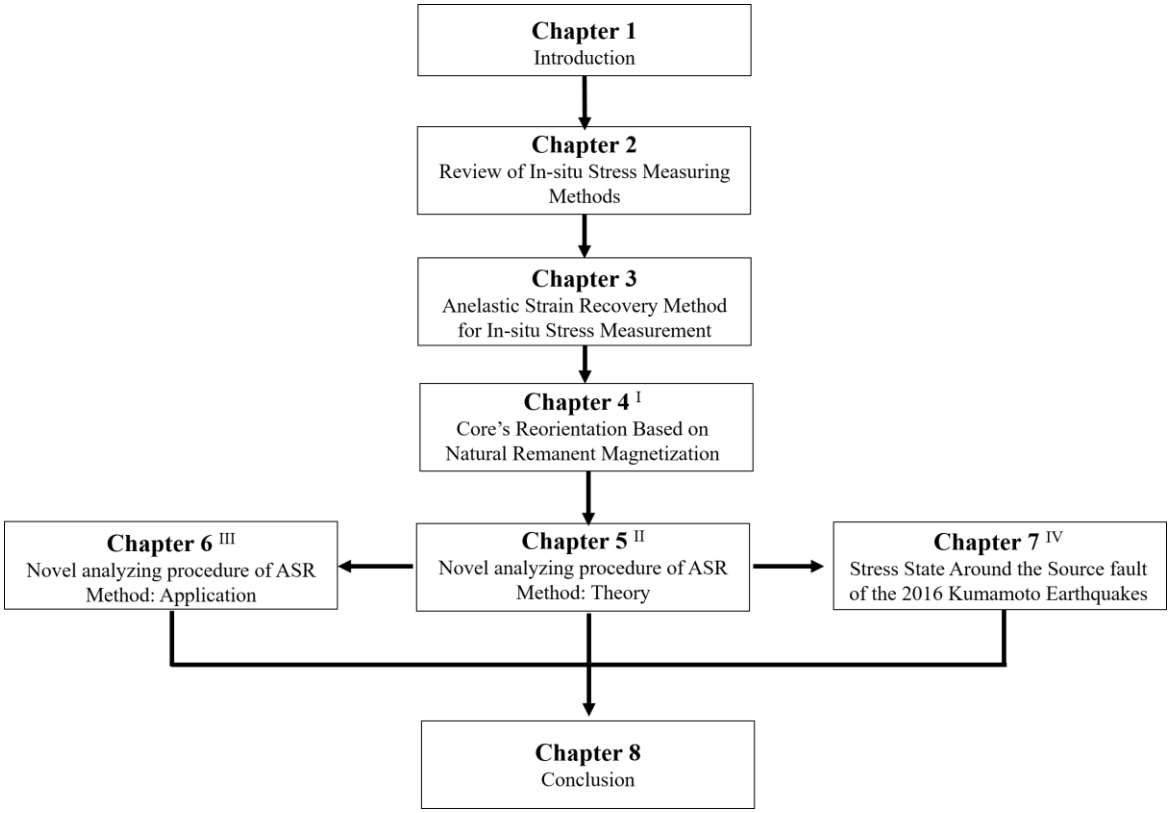

Fig. 1-1 Structure of this thesis. Roman numbers shown in this figure indicate the published, accepted (in-press) and in-preparation papers on these topics mentioned in each chapter (I: Sugimoto et al., 2020; II: Sugimoto et al., in press (a); III: Sugimoto et al., in prep; IV: Sugimoto et al., in press (b)).

Reference

Amadei, B., & Stephansson, O. (1997). *Rock stress and its measurement*. *Springer Science & Business Media*. https://doi.org/10.1007/978-94-011-5346-1

Haakon, F. (2016). *Structural Geology* (2nd ed.). Cambridge University Press.

Kyoto University. (2018). FY29 Commissioned for the disaster prevention on nuclear facilities (Dating Analyses of Drilling cores at the Futagawa fault), Technical Report (in Japanese), 208. Retrieved from https://www.nsr.go.jp/nra/chotatsu/yosanshikou/itaku_houkoku_h29.html

Sugimoto, T., Yano, S., Ishitsuka, K., & Lin, W. (n.d.). Application of Novel Analyzing Procedure of Anelastic Strain Recovery Method to Real Data Set.

Sugimoto, T., Shibutani, S., Lin, W., & Murata, S. (n.d.). Measurements of Post-seismic Stress State to 700 meters Depth using Anelastic Strain Recovery Method in Source Area of the 2016 Kumamoto Earthquakes. *Journal of the Japan Society of Engineering Geology*.

Sugimoto, T., Ishitsuka, K., & Lin, W. (n.d.). Theoretical Investigation on New Analyzing Procedure of Anelastic Strain Recovery Method for Stress Measurements based on Bayesian Statistical Modeling. *Journal of The Society of Materials Science, Japan*.

Sugimoto, T., Yamamoto, Y., Yamamoto, Y., & Lin, W. (2020). A Method for Core Reorientation Based on Rock Remanent Magnetization: Application to Hemipelagic Sedimentary Soft Rock. *Materials Transactions*, *61*(8), 1638–1644. https://doi.org/10.2320/matertrans.Z-M2020832

Yoshida, K., Hasegawa, A., Saito, T., Asano, Y., Tanaka, S., Sawazaki, K., et al. (2016). Stress rotations due to the M6.5 foreshock and M7.3 main shock in the 2016 Kumamoto, SW Japan, earthquake sequence. *Geophysical Research Letters, 43*(19), 10, 097–10, 104. https://doi.org/10.1002/2016GL070581

Yu, Z., Zhao, D., Li, J., Huang, Z., Nishizono, Y., & Inakura, H. (2019). Stress Field in the 2016 Kumamoto Earthquake (M 7.3) Area. *Journal of Geophysical Research:*

Solid Earth, *124*(3), 2638–2652. https://doi.org/10.1029/2018JB017079

Zoback, M. D. (2007). *Reservoir geomechanics*. *Cambridge University Press*.

Chapter 2

Review of In-situ Stress Measuring Methods

2.1 Why in-situ stress measurements?

In this section, the methods of in-situ stress measurement are described. In this study, the in-situ stress is defined as the present stress. In-situ stress measurement is a vital aspect of various geoengineering and geoscience fields. Understanding the stress state is important for high efficiency and safety, especially in oil and gas development or underground space utilization.

The stress state can be estimated to a certain extent. For example, in regions with flat ground surfaces and horizontal strata, vertical stress is considered to be one of the principal stresses. Additionally, a certain relationship is known to exist between stress in the horizontal plane and vertical stress (Amadei & Stephansson, 1997).

Several previous studies have proposed relationships between the depth and magnitude of vertical stress or the ratio of magnitudes of vertical stress and mean horizontal stress, based on the measured data in different regions of the world (Haimson, 1975; Hast, 1969, 1973; Rummel, 1986; Ove Stephansson, 1993; Zoback & Healy, 1992). As an illustrative example, Fig. 2-1 shows the variations in vertical stress and the ratio of the mean horizontal stress to the vertical stress with depth for different regions of the world, as proposed by Brown and Hoek (1978). In this chapter, all stresses are total

stresses, unless stated otherwise. Notably, the compressive stresses and extensional strain and displacement are defined as positive.

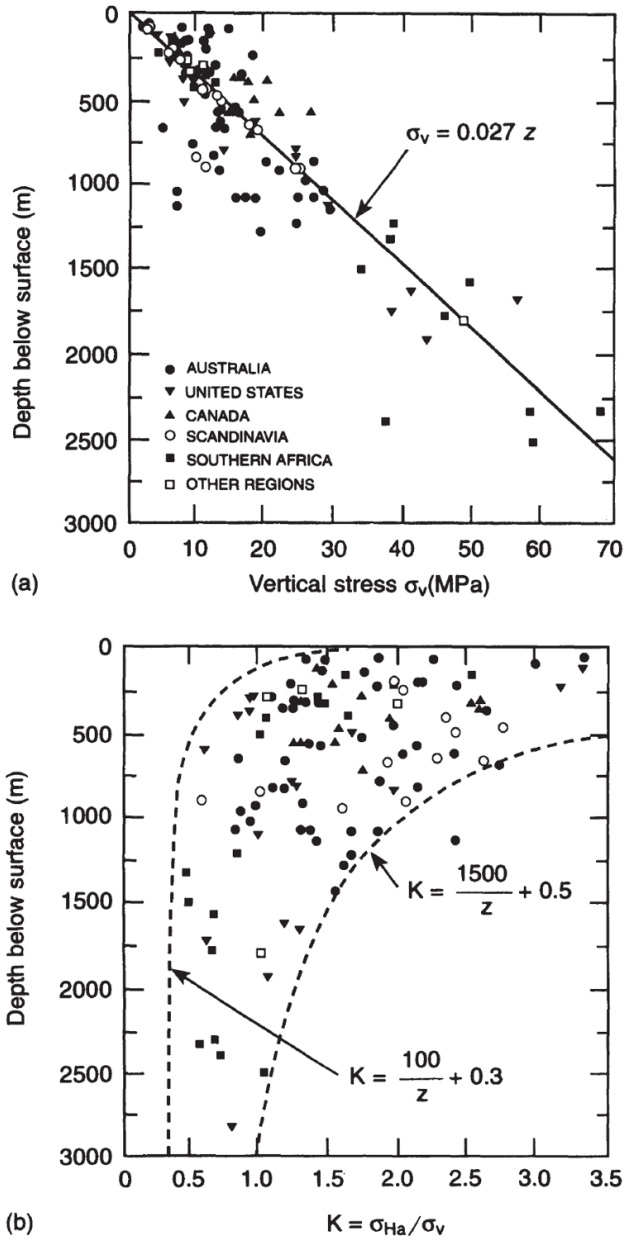

Fig. 2-1 (a) Plot of vertical stress against depth, z, below the surface; (b) variation of the average horizontal to vertical stress ratio with depth (After Brown & Hoek, 1978).

In regions with a flat topography, the "static" vertical stress can be approximated with high accuracy using the overburden weight $\rho g z$, calculated using the rock density

profile. Fig. 2-1(a) plots the values of the vertical stress σ_{v} measured in many regions, including the straight line expressed by $\sigma_{\mathrm{v}} = \rho g z$ when $\rho = 2.7 \times 10^3\ \mathrm{kg/m^3}$. This figure shows that the vertical stress can be expressed using the value of the overburden weight to some extent.

Alternatively, horizontal stresses are generally discussed based on the ratio of the magnitudes of the horizontal and vertical stresses:

$$K = \sigma_{\mathrm{Ha}}/\sigma_{\mathrm{v}}, \tag{2-1}$$

where

$$\sigma_{\mathrm{Ha}} = \frac{(S_{\mathrm{Hmax}} + S_{\mathrm{hmin}})}{2} \tag{2-2}$$

is the averaged horizontal stress, and S_{Hmax} and S_{hmin} are the maximum and minimum horizontal stresses, respectively. Assuming that: (1) the rock mass is an ideal, homogeneous, linearly isotropic continuous half-space with a horizontal surface, (2) the rock mass is under the influence of gravity alone with vanishing horizontal displacements, and (3) the loading history has no influence on how the in-situ stresses build up, σ_{Ha} can be expressed by:

$$\sigma_{\mathrm{Ha}} = K\sigma_{\mathrm{v}} \tag{2-3}$$

where

$$K = \frac{\nu}{1-\nu} \tag{2-4}$$

and ν is Poisson's ratio of the rock formation. In particular, it is expected that the stress in the horizontal plane increases linearly with depth along with the vertical stress. However, Fig. 2-1(b) shows that the ratio of the magnitudes of horizontal and vertical stress varies greatly with depth.

As Fig. 2-2 shows, there are many factors controlling the in-situ stress. For example, tectonic stress, one such factors affecting the in-situ stress, is controlled by a combination of various factors associated with plate motion (Fig. 2-3). Therefore, the stress state explained based only on the current geological conditions or some past events is incomplete. Therefore, to obtain the true in-situ stress, it is necessary to conduct in-situ stress measurements. From this perspective, many stress measurement methods have been proposed.

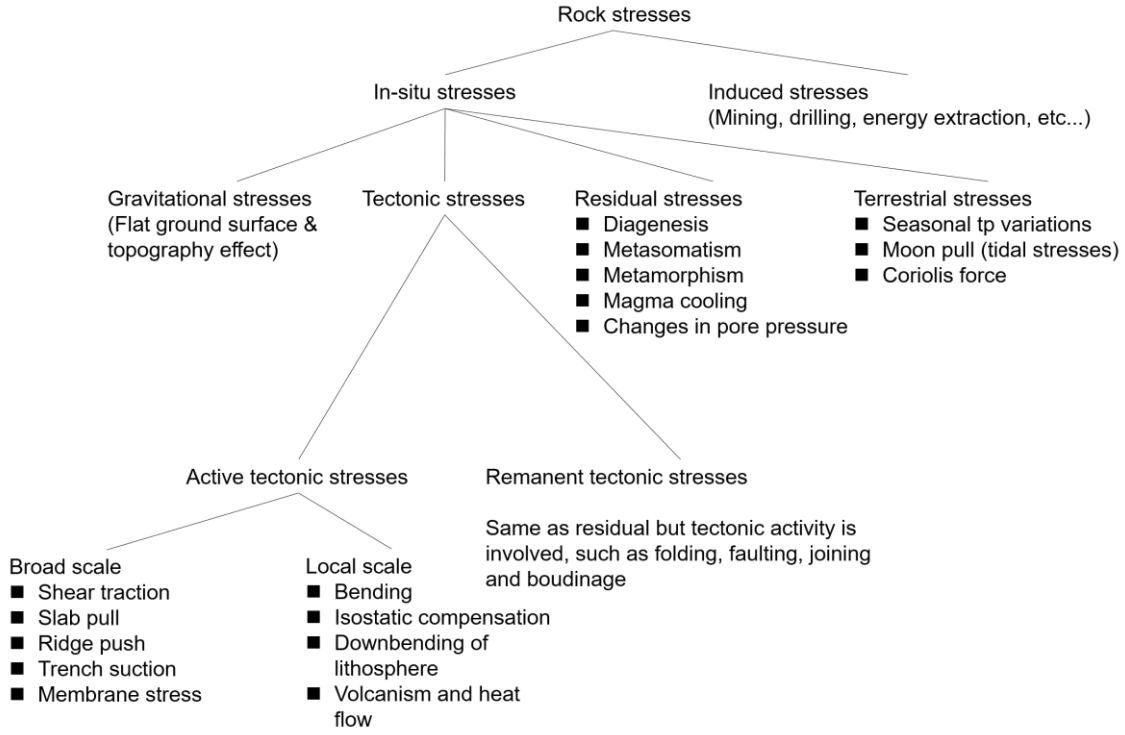

Fig. 2-2 Terminology of in-situ stress. (Modified from Amadei & Stephansson, 1997)..

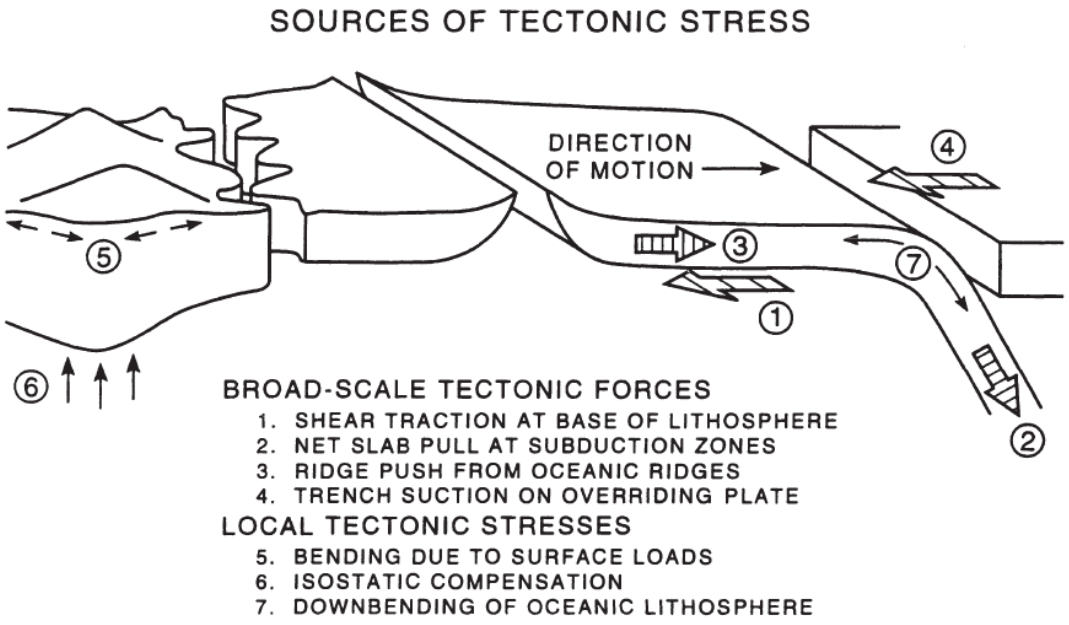

Fig. 2-3 Stress sources composing the tectonic stress. (After Zoback et al., 1989)..

Many in-situ stress measurements are conducted under the assumption of a two-dimensional stress state wherein one of the principal stresses becomes a vertical stress. However, there is no guarantee that this assumption holds in geological formations with complex structures such as faults. Therefore, conducting three-dimensional stress measurements such as the ASR method is necessary to determine stresses more precisely. The following provides an overview of existing stress measurement methods.

2.2 Methods of in-situ stress measurements

In this section, I review the methods of in-situ stress measurements used today. These methods can be classified according to several aspects. In this thesis, methods are classified as core-based or non-core-based. Core-based methods determine the in-situ stress using rock core samples retrieved from boreholes. Non-core-based methods determine the in-situ stress based on the information obtained without rock core samples, such as from borehole images, pressure data of hydraulic fracturing in boreholes, and seismic wave velocities from vertical seismic profiles (VSPs).

Core-based methods include the ASR method, DCDA, differential strain curve analysis (DSCA), deformation rate analysis (DRA), acoustic emission (AE), core disking, and others. Conversely, non-core-based methods include hydraulic fracturing, borehole breakout method, drilling induced tensile fracture (DITF) analysis, focal mechanism solution, over-coring, and others. In the following sections, the details of the DCDA, ASR method, hydraulic fracturing method, and borehole breakout method, which are relevant to this study, are described among these stress measurement methods.

2.2.1 Core-based method

In core-based methods, the in-situ stress is determined by conducting laboratory tests on the drilled core. In this section, the DCDA and ASR methods, which are stress measurement methods based on the strain recovery of the rock, are described. When a core sample is drilled and released from the in-situ stress, elastic and anelastic strain recoveries occur in the core sample. The DCDA and ASR method use the former and latter strain recoveries, respectively, for the in-situ stress measurement (Fig. 2-4).

The ASR method evaluates stress by measuring the ASR of a core sample after stress release by drilling. ASR is relatively small and requires high measurement accuracy (~10 μstrain). One feature of this method is that the three-dimensional stress can be determined with a single rock core sample. This method is applicable to rock types with

large ASR. The problem is its inapplicability to rock types with significant anisotropy. Additionally, the measurement must be conducted immediately after the stress release, at or near the site; therefore, it is subject to the drilling schedule.

When a rock core sample is released from anisotropic in-situ stresses by drilling, the cross-sectional shape of the core, which is initially a circle, becomes an ellipse. The DCDA method regards the direction of the major axis of the ellipse as the direction of the maximum horizontal principal stress. The difference between the lengths of the major and minor axes can be used to evaluate the difference between the magnitudes of maximum and minimum horizontal principal stresses. The measurement is simple and nondestructive. One problem of this method is the high dependency of the measurement to the quality of the core surface. Additionally, the current method does not consider the anisotropy of the rock.

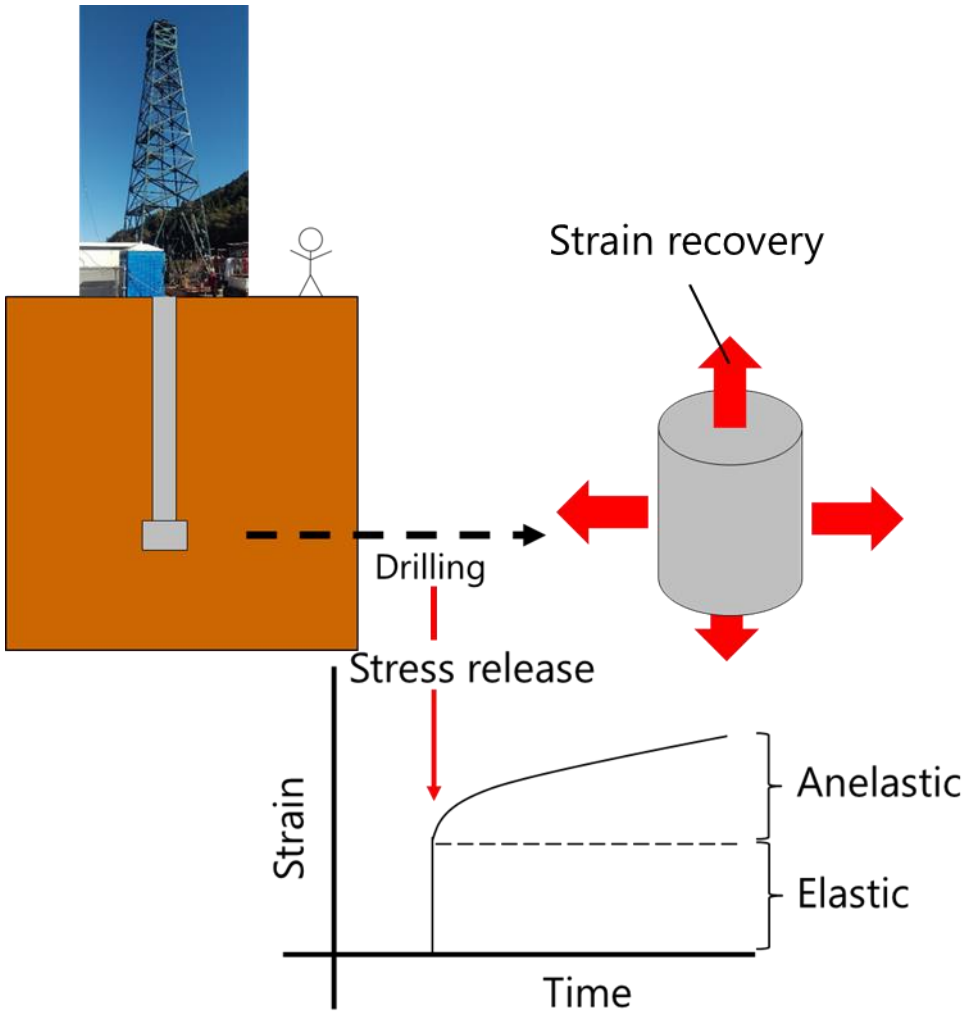

Fig. 2-4 Two strain recoveries occuring on a drillied rock core sample: elastic and anelastic strain recoveries.

Diametrical core deformation analysis (DCDA)

The DCDA method (Funato & Ito, 2017; Ito et al., 2013) is a two-dimensional stress measurement method wherein the core axis is assumed to be one of the principal stresses. The DCDA method can determine the directions of maximum and minimum principal stresses, and the difference between the maximum principal stress and the minimum principal stress in the plane orthogonal to the core axis. In the case of vertical drilling, they are the maximum and minimum horizontal stresses, respectively. As mentioned above, the DCDA method determines the stress based on the elastic strain recovery that occurs in the drilled core sample. Elastic strain recovery is completed instantaneously on

drilling; thus, measurement using strain gauges is not possible. Therefore, the DCDA method cannot directly measure the amount of elastic strain recovery, but instead uses the deformation generated by the stress release during drilling to determine the stress.

The measurement principle is as follows: in a plane perpendicular to the core axis, the magnitudes of maximum and minimum principal stresses are generally different; thus, the amount of elastic strain recovery generated by the stress release also differs depending on the stress magnitudes. Therefore, the cross-sectional shape of the core sample after drilling is elliptical. If the rock can be assumed to be an isotropic elastic body, the displacement in the direction of maximum principal stress will be the largest and the that in the direction of minimum principal stress will be the smallest (Fig. 2-5).

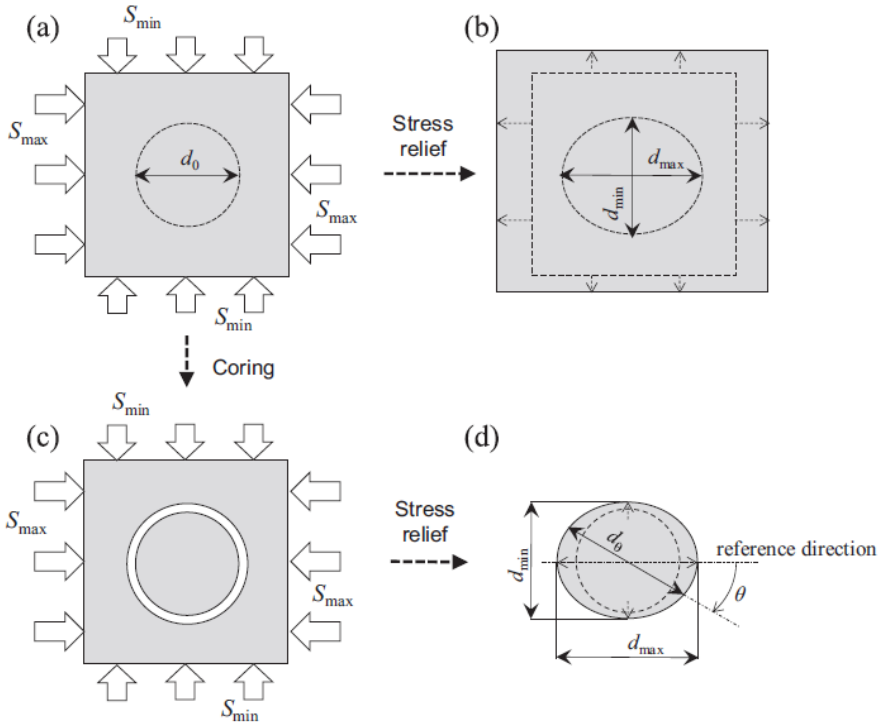

Fig. 2-5 Elastic strain recovery caused by in situ stress release (After Ito et al., 2013).

Therefore, if the core sample can be reoriented, the horizontal principal stress direction can be determined by the DCDA method. Assuming that the rock constituting the core sample is an isotropic homogeneous elastic body, the differential stress can be obtained by using the difference between the major and minor axes as follows:

$$S_{\mathrm{Hmax}} - S_{\mathrm{hmin}} = \frac{E}{1+\nu}\frac{(d_{\max} - d_{\min})}{d_0} \approx \frac{E}{1+\nu}\frac{(d_{\max} - d_{\min})}{d_{\min}}, \qquad (2\text{-}5)$$

where S_{Hmax} and S_{hmin} are the maximum and minimum horizontal principal stresses, respectively, E and ν are the Young's modulus and Poisson's ratio of the rock core, and $d_{\max}$, $d_{\min}$, and d_0 are the maximum, minimum, and original diameter of the cross section of the rock core, respectively. The original diameter d_0 is the diameter before the deformation caused by the elastic strain recovery and cannot be measured after drilling. In actual measurements, neglecting the difference between d_0 and $d_{\min}$ does not cause a significant difference in the measurement results. Therefore, in previous studies, $d_{\min}$ was used instead of d_0.

Fig. 2-6 shows a schematic diagram of the measuring system for the DCDA method.

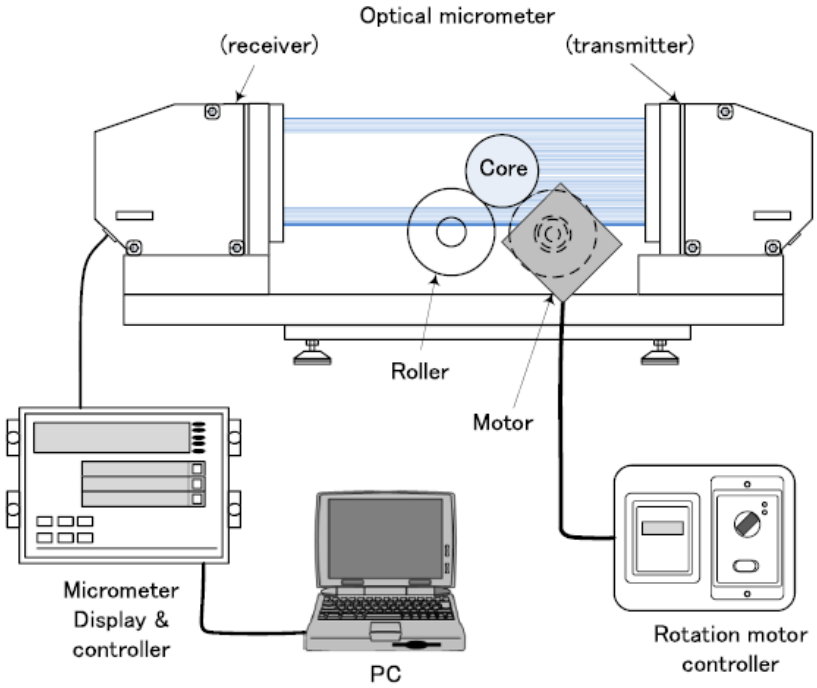

Fig. 2-6 Measuring system of the DCDA method (After Funato & Ito, 2017).

The DCDA method is simple and non-destructive, and can thus easily be applied to many

core samples to obtain considerable data.

Anelastic strain recovery method (ASR method)

The ASR method is a method of stress measurement based on the ASR in core samples. This method is the main subject of this study and is described in detail in Chapter 3.

2.2.2 Non core-based method

Owing to the classification of stress measurement methods in this thesis, various stress measurement methods are classified into non-core-based methods. In this section, we focus on the hydraulic fracturing and borehole breakout methods, which are the two most frequently used methods and are relevant to this study.

In the hydraulic fracturing method, mud pressure is applied to a drilled borehole to fracture the borehole wall. One of the features of this method is that the stress magnitudes are measured directly by the mud pressure; therefore, the reliability of the measurement of the minimum principal stress in the horizontal plane is relatively high. The problems of this method are that: (i) the measured values of maximum principal stress are not as reliable, (ii) a collapse of the borehole wall makes it impossible to conduct the measurement, and (iii) as the depth increases, conducting the measurement can become difficult.

The borehole breakout method conducts stress measurements based on compressive (breakouts) and tensile fractures (DITF) that occur in the borehole wall as a result of drilling. One feature of this method is its ease while being applied to large depths. Additionally, when borehole breakout or DITF occur, they can be observed at many points; therefore, it is easy to obtain the depth profile of stress, and obtaining relatively reliable data by statistical processing is possible. One problem with this method is that it cannot be applied without the occurrence of breakout and DITF.

Hydraulic fracturing method

Hydraulic methods of in-situ stress measurements can determine the in-situ stresses by isolating a short section in a borehole and applying a hydraulic pressure on its wall. Hydraulic methods can be divided into three subgroups: the hydraulic fracturing method, sleeve fracturing method, and hydraulic tests on pre-existing fractures (HTPF). One advantage of the hydraulic methods is that they can be used to determine the in-situ stress without knowledge of the rock deformation properties. While applying the hydraulic fracturing method and sleeve fracturing method, the borehole direction is required to be the direction of one of the principal stresses. Conversely, the HTPF method does not require this assumption. In this thesis, only fundamental concepts of the HF method are explained in detail.

The concept of hydraulic fracturing was first proposed by Clark (1949). However, his objective was to improve oil recovery by fracturing the formation. Fairhurst (1964) first showed that hydraulic fracturing could be used for stress measurement. For further details on the sleeve fracturing method, please refer to Ljunggren & Stephansson (1986) and Stephansson (1983a, 1983b). For further details on HTPF, please refer to Cornet (1986), Cornet (1993), and Cornet & Valette (1984).

In the following, the theoretical solution derived by Haimson and Fairhurst (1969 and 1967), and the stress measurement method based on the theoretical solution are described. In this section, it is assumed that the rock formation is subjected to a non-hydrostatic state of stress with one of the three principal stresses acting parallel to the vertical direction and along the borehole axis. The general equations of the in-situ stress fields $\sigma_{ij}^{(1)}$ around the circular borehole drilled in the rock formation, which is linearly elastic, porous, isotropic, and homogeneous, are given by the Kirsch solution:

$$\sigma_{rr}^{(1)} = \left(1 - \frac{R^2}{r^2}\right)\frac{(S_{\mathrm{Hmax}} + S_{\mathrm{hmin}} - 2p_0)}{2} + \left(1 + 3\frac{R^4}{r^4} - 4\frac{R^2}{r^2}\right)\frac{(S_{\mathrm{Hmax}} - S_{\mathrm{hmin}})}{2}\cos 2\theta + p_0 \tag{2-6}$$

$$\sigma_{\theta\theta}^{(1)} = \left(1 + \frac{R^2}{r^2}\right)\frac{(S_{\mathrm{Hmax}} + S_{\mathrm{hmin}} - 2p_0)}{2} - \left(1 + 3\frac{R^4}{r^4}\right)\frac{(S_{\mathrm{Hmax}} - S_{\mathrm{hmin}})}{2}\cos 2\theta + p_0 \quad (2\text{-}7)$$

$$\sigma_{r\theta}^{(1)} = \left(1 - 3\frac{R^4}{r^4} + 2\frac{R^2}{r^2}\right)\frac{(S_{\mathrm{Hmax}} - S_{\mathrm{hmin}})}{2}\sin 2\theta, \quad (2\text{-}8)$$

where $\sigma_{rr}^{(1)}$ is the radial stress, $\sigma_{\theta\theta}^{(1)}$ is the circumferential stress, $\sigma_{r\theta}^{(1)}$ is the tangential shear stress, p_0 is the fluid pressure in the rock formation, R is the radius of the borehole, r is the distance from the center of the borehole, and θ is the angle measured from the direction of S_{Hmax}.

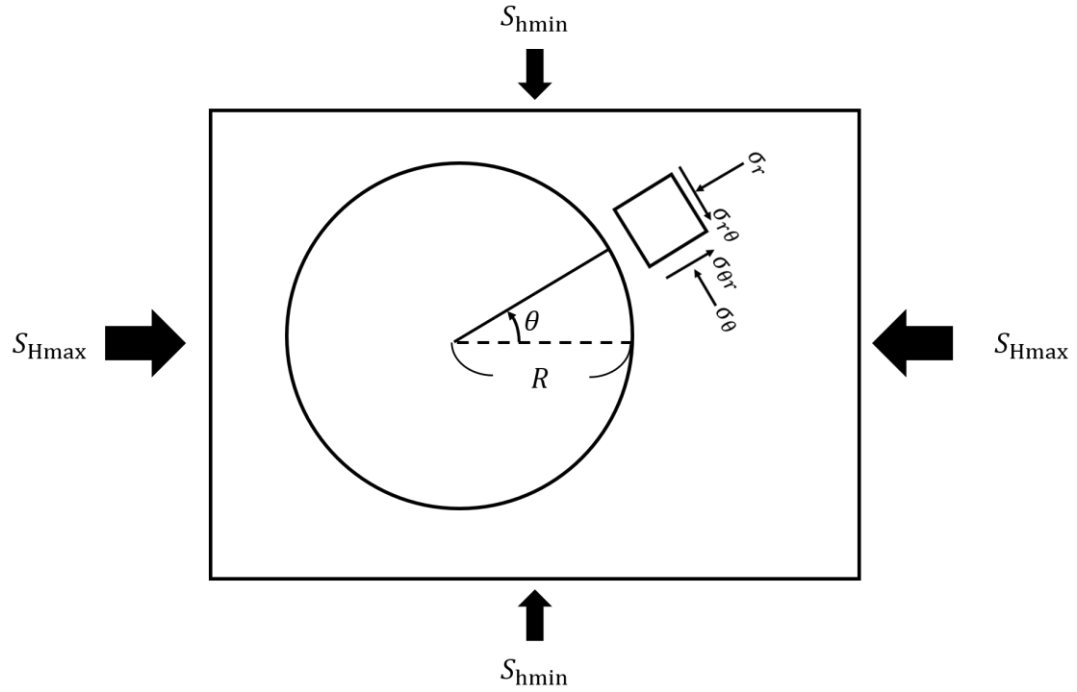

Fig. 2-7 Polar coordinate system and the stress elements in this coordinate system.

When the fluid is pumped into the borehole, two additional stress fields are introduced. The first is introduced by the increase in pressure from the original pressure p_0 to the injected fluid pressure p_b. The equations for the stress fields $\sigma_{ij}^{(2)}$ are

$$\begin{aligned} \sigma_{rr}^{(2)} &= \frac{R^2}{r^2}\Delta p \\ \sigma_{\theta\theta}^{(2)} &= -\frac{R^2}{r^2}\Delta p \\ \sigma_{r\theta}^{(2)} &= 0, \end{aligned} \tag{2-9}$$

where $\Delta p = p_\mathrm{b} - p_0$ is the difference between the fluid pressure in the borehole p_b and p_0.

The second stress field is introduced when the rock formation is permeable to the injected fluid. This stress field is called $\sigma_{ij}^{(3)}$. If the injected fluid penetrates the rock formation, an outward radial flow occurs. The assumption that the fluid flow is axisymmetric leads to the equations derived by the poroelasticity theory:

$$\begin{aligned}\sigma_{rr}^{(3)} &= \frac{\alpha(1-2\nu)}{r^2(1-\nu)}\int_R^r p(r)r\mathrm{d}r \\ \sigma_{\theta\theta}^{(3)} &= -\frac{\alpha(1-2\nu)}{1-\nu}\left[\frac{1}{r^2}\int_R^r p(r)r\mathrm{d}r - p(r)\right] \\ \sigma_{r\theta}^{(3)} &= 0,\end{aligned} \tag{2-10}$$

Here, $p(r)$ is the increase in pressure above p_0 at any distance r, ν is the Poisson's ratio of the rock formation, and α is the Biot coefficient

$$\alpha = 1 - \frac{K}{K_\mathrm{s}}, \tag{2-11}$$

where K_s and K are the bulk moduli of the rock constituents (grains) and the rock itself (grains, pores, and microcracks), respectively.

The stress field around the borehole is then given by the superposition of the three different stress fields:

$$\sigma_{ij} = \sigma_{ij}^{(1)} + \sigma_{ij}^{(2)} + \sigma_{ij}^{(3)}. \tag{2-12}$$

From (2-6) to (2-12), the stress elements at the borehole wall ($r = R$) with the direction of maximum horizontal principal stress can be expressed by:

$$\begin{aligned}\sigma_{rr} &= p_0 + \Delta p = p_b \\ \sigma_{\theta\theta} &= 3S_{\mathrm{hmin}} - S_{\mathrm{Hmax}} - 2p_0 + p_0 - \Delta p + \alpha\Delta p\frac{(1-2\nu)}{1-\nu} \\ &= 3S_{\mathrm{hmin}} - S_{\mathrm{Hmax}} - p_b + \alpha\Delta p\frac{(1-2\nu)}{1-\nu} \\ \sigma_{r\theta} &= 0.\end{aligned} \tag{2-13}$$

The tangential effective stress $\sigma'_{\theta\theta} = \sigma_{\theta\theta} - p_\mathrm{b}$ is given by:

$$\sigma'_{\theta\theta} = \sigma_{\theta\theta} - p_{\mathrm{b}} = 3S_{\mathrm{hmin}} - S_{\mathrm{Hmax}} - 2p_b + \alpha\Delta p\frac{(1-2\nu)}{1-\nu}, \qquad (2\text{-}14)$$

which becomes the first tensile fracture around the borehole wall. The directions of the horizontal principal stresses are then determined by the tensile fracture initiated by hydraulic fracturing (Fig. 2-8). I now postulate that the breakdown of the borehole wall occurs when the tangential effective stress is equal to the tensile strength T:

$$\sigma'_{\theta\theta} = -T. \qquad (2\text{-}15)$$

Combining (2-14) and (2-15), the minimum pressure at the borehole wall to induce fracture, also known as the breakdown pressure p_{c}, is given by the equation:

$$p_{\mathrm{c}} = \frac{T + 3S_{\mathrm{hmin}} - S_{\mathrm{Hmax}} - 2\eta p_0}{2(1-\eta)}. \qquad (2\text{-}16)$$

where

$$\eta = \frac{\alpha(1-2\nu)}{2(1-\nu)}. \qquad (2\text{-}17)$$

When the rock formation is non-permeable, the above equations are replaced by the following equations:

$$p_{\mathrm{c}} = T + 3S_{\mathrm{hmin}} - S_{\mathrm{Hmax}} - p_0. \qquad (2\text{-}18)$$

Bredehoeft et al. (1976) first suggested that the tensile strength of the non-permeable formation could be determined from the borehole reopening pressure and the first breakdown pressure from the equation:

$$T = p'_{\mathrm{c}} - p_{\mathrm{r}}. \tag{2-19}$$

When the formation is permeable, the tensile strength is

$$T = 2(1-\eta)(p'_{\mathrm{c}} - p_{\mathrm{r}}). \tag{2-20}$$

The maximum horizontal principal stress is then given by

$$S_{\mathrm{Hmax}} = 3S_{\mathrm{hmin}} - 2(1-\eta)p_{\mathrm{r}} - 2\eta p_0. \tag{2-21}$$

The determination of S_{hmin} is straightforward using the shut-in pressure p_{s}, which is the pressure when the fracture closes:

$$S_{\mathrm{hmin}} = p_{\mathrm{s}}. \tag{2-22}$$

The p'_{c}, p_{r} and p_{s} are determined using the pressure-time record of the fracturing test (Fig. 2-9).

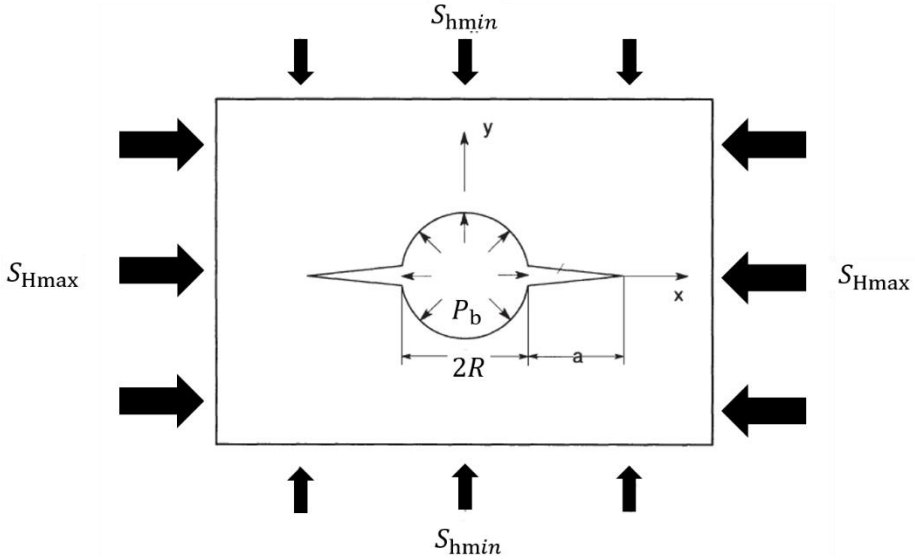

Fig. 2-8 Schematic diagram of the fracture initiated by the pumped fluid. (Modified from Amadei & Stephansson (1997)).

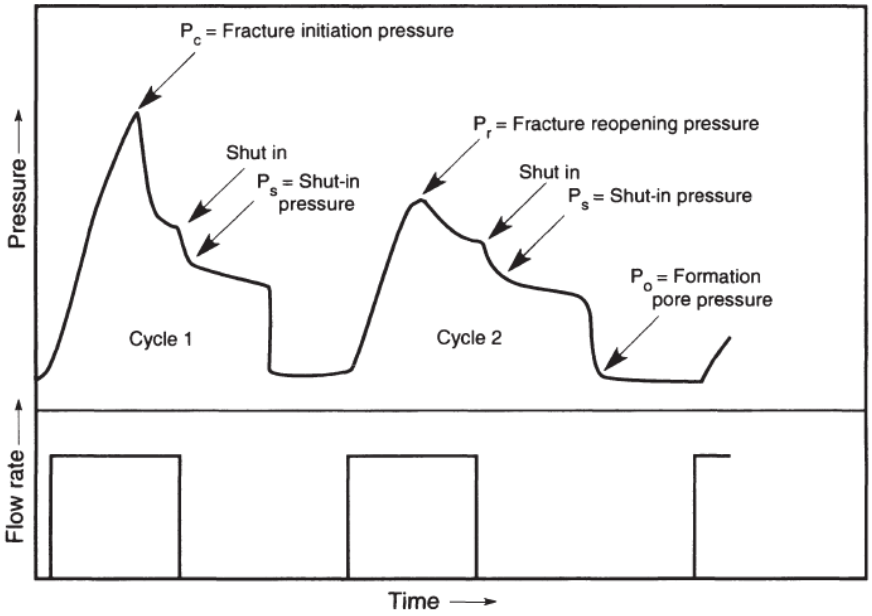

Fig. 2-9 Pressure-time and flow rate-time record of the idealized fracturing test (Amadei & Stephansson, 1997).

Borehole breakout method

Borehole breakout is a phenomenon wherein the borehole wall breaks due to the shear stress concentration around the borehole caused by drilling. Borehole breakout elongates the borehole diameter in the direction of the wall, where the shear stress concentration occurs. As the direction of elongation is determined by the stress state around the borehole, it is possible to estimate the in-situ stress direction from this (Fig. 2-10).

Leeman (1964) was the first to realize that breakout could be used for the in-situ stress measurement. Several previous studies have since verified the principle of borehole breakout generation and its reliability for stress measurement (Babcock, 1978; Cox, 1970; Dart & Zoback, 1989; Hickman et al., 1985; Zoback et al., 1985).

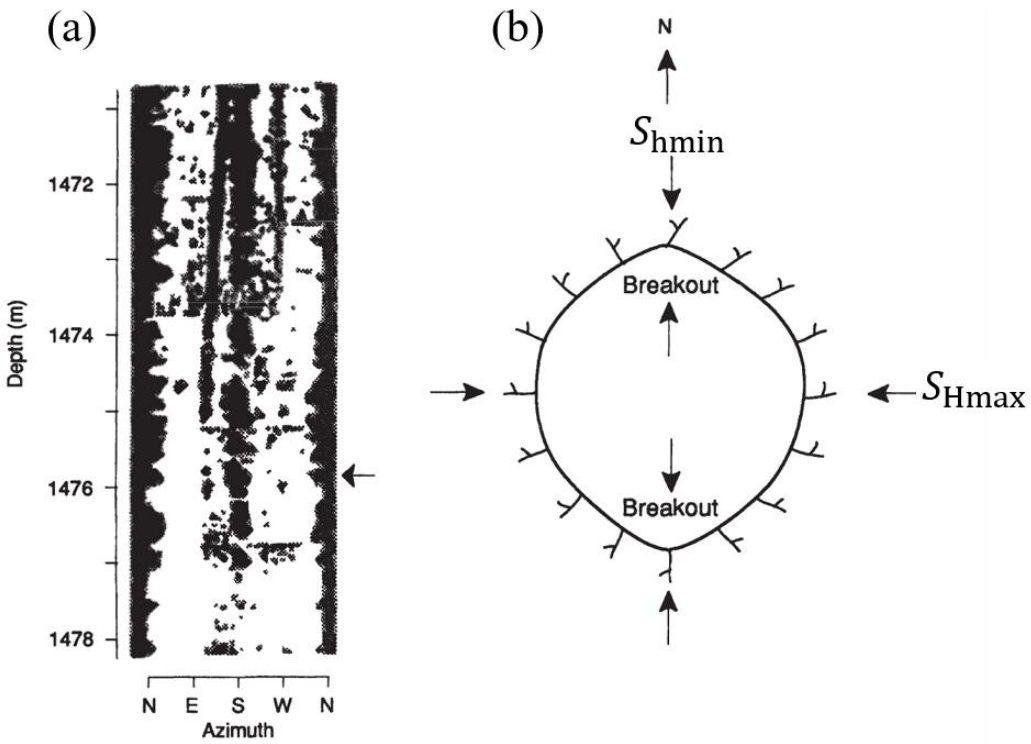

Fig. 2-10 Image of borehole breakout. (a) Section of borehole televiewer log showing zones of borehole breakouts (black batches). (b) Horizontal cross-section of borehole breakout at a depth of 1475.8 m (arrow in (a)). (Modified from Amadei & Stephansson, 1997; Hickman et al. 1985).

The theory of the borehole breakout method is described below. The analytical method usually used is based on the Kirsch solution for isotropic homogeneous linear elastic bodies in three dimensions (Jaeger et al., 2007; Kirsch, 1898), which was proposed by Zoback et al. (1985) and improved by Singh & Digby (1989b, 1989a).

When drilling mud is injected into a vertical hole of radius R drilled in a rock mass assumed to be an isotropic homogeneous linear elastic material, the stress state around the hole can be expressed as follows:

$$\sigma_{rr} = \left(1 - \frac{R^2}{r^2}\right)\frac{(S_{\mathrm{Hmax}} + S_{\mathrm{hmin}} - 2p_0)}{2} + \left(1 + 3\frac{R^4}{r^4} - 4\frac{R^2}{r^2}\right)\frac{(S_{\mathrm{Hmax}} - S_{\mathrm{hmin}})}{2}\cos 2\theta + \Delta p\frac{R^2}{r^2} \tag{2-23}$$

$$\sigma_{\theta\theta} = \left(1 + \frac{R^2}{r^2}\right)\frac{(S_{\mathrm{Hmax}} + S_{\mathrm{hmin}} - 2p_0)}{2} - \left(1 + 3\frac{R^4}{r^4}\right)\frac{(S_{\mathrm{Hmax}} - S_{\mathrm{hmin}})}{2}\cos 2\theta - \Delta p\frac{R^2}{r^2} \tag{2-24}$$

$$\sigma_{r\theta} = \left(1 - 3\frac{R^4}{r^4} + 2\frac{R^2}{r^2}\right)\frac{(S_{\mathrm{Hmax}} - S_{\mathrm{hmin}})}{2}\sin 2\theta, \tag{2-25}$$

where σ_{rr} is the radial stress, $\sigma_{\theta\theta}$ is the circumferential stress, $\sigma_{r\theta}$ is the tangential shear stress, R is the radius of the borehole, r is the distance from the center of the borehole, θ is the angle measured from the direction of S_{Hmax}, and $\Delta p = p_{\mathrm{b}} - p_0$ is the difference between the fluid pressure in the borehole p_{b} and that in the rock formation p_0.

(2-25) shows that the maximum shear stress around the borehole is located at 90° and 270° from the direction of maximum principal stress in the horizontal plane, namely, the direction of minimum principal stress in the horizontal plane. This implies that borehole breakout occurs in the direction of minimum principal stress in the horizontal plane. In the borehole breakout method, the direction of principal stress in the horizontal plane is determined based on this fact.

In the borehole breakout method, it is theoretically possible to obtain the magnitude of stress by assuming that one of the principal stresses is vertical, the failure surface is parallel to the borehole axis, and the failure of the rock follows the Mohr–Coulomb failure criterion. For further details, please refer to Amadei and Stephansson (1997).

In addition to the borehole breakout method, the DITF method exists as an in-

situ stress measurement method based on the phenomenon of hole wall fracture induced by drilling (Brudy & Zoback, 1999). While the borehole breakout method measures the stress based on the shear failure phenomenon around the borehole wall caused by drilling, the DITF method measures it based on the tensile failure around the borehole wall caused by drilling. Similar to the borehole breakout method, the DITF method is also based on the Kirsch solution. For details of this method, please refer to Brudy and Zoback (1999) and Zoback (2007).

References

Amadei, B., & Stephansson, O. (1997). *Rock stress and its measurement*. *Springer Science & Business Media*. https://doi.org/10.1007/978-94-011-5346-1

Babcock, E. A. (1978). Measurement of subsurface fractures from dipmeter logs. Retrieved from https://www.osti.gov/biblio/5821025

Bredehoeft, J. D., Wolff, R. G., Keys, W. S., & Shuter, E. (1976). Hydraulic fracturing to determine the regional in situ stress field, Piceance Basin, Colorado. *GSA Bulletin*, *87*(2), 250–258. https://doi.org/10.1130/0016-7606(1976)87<250:HFTDTR>2.0.CO;2

Brown, E. T., & Hoek, E. (1978). Trends in relationships between measured in-situ stresses and depth. *International Journal of Rock Mechanics and Mining Sciences And*, *15*(4), 211–215. https://doi.org/10.1016/0148-9062(78)91227-5

Brudy, M., & Zoback, M. D. (1999). Drilling-induced tensile wall-fractures: Implications for determination of in-situ stress orientation and magnitude. *International Journal of Rock Mechanics and Mining Sciences*, *36*(2), 191–215. https://doi.org/10.1016/S0148-9062(98)00182-X

Clark, J. B. (1949). A Hydraulic Process for Increasing the Productivity of Wells. *Journal of Petroleum Technology*, *1*(01), 1–8. https://doi.org/10.2118/949001-G

Cornet, F. H. (1986). Stress Determination From Hydraulic Tests On Preexisting Fractures - the H.T.P.F. Method. *ISRM International Symposium*. Stockholm, Sweden: International Society for Rock Mechanics and Rock Engineering. Retrieved from https://doi.org/

Cornet, F. H. (1993). 15 - The HTPF and the Integrated Stress Determination Methods. In J. A. B. T.-R. T. and S. C. HUDSON (Ed.) (pp. 413–432). Oxford: Pergamon. https://doi.org/https://doi.org/10.1016/B978-0-08-042066-0.50022-7

Cornet, F. H., & Valette, B. (1984). In situ stress determination from hydraulic injection test data. *Journal of Geophysical Research*, *89*(B13), 11527–11537. https://doi.org/10.1029/JB089iB13p11527

Cox, J. W. (1970). The High Resolution Dipmeter Reveals Dip-Related Borehole And

Formation Characteristics. *SPWLA 11th Annual Logging Symposium*. Los Angeles, California: Society of Petrophysicists and Well-Log Analysts. Retrieved from https://doi.org/

Dart, R. L., & Zoback, M. Lou. (1989). Wellbore Breakout Stress Analysis Within The Central And Eastern Continental United States. *The Log Analyst*, *30*(01), 14. Retrieved from https://doi.org/

Fairhurst, C. (1964). Measurement of in-situ rock stresses. With particular reference to hydraulic fracturing. Retrieved from https://www.osti.gov/biblio/7056203

Funato, A., & Ito, T. (2017). A new method of diametrical core deformation analysis for in-situ stress measurements. *International Journal of Rock Mechanics and Mining Sciences*, *91*(May 2016), 112–118. https://doi.org/10.1016/j.ijrmms.2016.11.002

Haimson, B. C. (1975). The state of stress in the Earth's crust. *Reviews of Geophysics*, *13*(3), 350–352. https://doi.org/10.1029/RG013i003p00350

Haimson, B, & Fairhurst, C. (1969). In-Situ Stress Determination At Great Depth By Means Of Hydraulic Fracturing. *The 11th U.S. Symposium on Rock Mechanics (USRMS)*. Berkeley, California: American Rock Mechanics Association. Retrieved from https://doi.org/

Haimson, Bezalel, & Fairhurst, C. (1967). Initiation and Extension of Hydraulic Fractures in Rocks. *Society of Petroleum Engineers Journal*, *7*(03), 310–318. https://doi.org/10.2118/1710-PA

Hast, N. (1969). The state of stress in the upper part of the earth's crust. *Tectonophysics*, *8*(3), 169–211. https://doi.org/https://doi.org/10.1016/0040-1951(69)90097-3

Hast, N. (1973). Global measurements of absolute stress. *Philosophical Transactions of the Royal Society of London. Series A, Mathematical and Physical Sciences*, *274*(1239), 409–419.

Hickman, S. H., Healy, J. H., & Zoback, M. D. (1985). In situ stress, natural fracture distribution, and borehole elongation in the Auburn geothermal well, Auburn, New York. *Journal of Geophysical Research: Solid Earth*, *90*(B7), 5497–5512.

Ito, T., Funato, A., Lin, W., Doan, M.-L., Boutt, D. F., Kano, Y., et al. (2013). Determination of stress state in deep subsea formation by combination of hydraulic

fracturing in situ test and core analysis: A case study in the IODP Expedition 319. *Journal of Geophysical Research: Solid Earth*, *118*(3), 1203–1215. https://doi.org/https://doi.org/10.1002/jgrb.50086

Jaeger, J. C., Cook, N. G. W., & Zimmerman, R. (2007). *Fundamentals of rock mechanics*. Wiley-Blackwell.

Kirsch, G. (1898). Die Theorie der Elastizitat und die Bedurfnisse der Festigkeitslehre. *Zantralblatt Verlin Deutscher Ingenieure*, *42*, 797–807.

Leeman, E. R. (1964). The measurement of stress in rock : Part I : The principles of rock stress measurements. *Journal of the Southern African Institute of Mining and Metallurgy*, *65*(2), 45–81. Retrieved from https://journals.co.za/content/saimm/65/2/AJA0038223X_4882

Ljunggren, C., & Stephansson, O. (1986). Sleeve Fracturing - A Borehole Technique For In-situ Determination of Rock Deformability And Rock Stresses. *Proc. Int. Conf. Applied Rock Engieering*, 323–330. Retrieved from https://doi.org/

Rummel, F. (1986). Stresses and tectonics of the upper continental crust-a review. In *ISRM International Symposium* (pp. 177–186). International Society for Rock Mechanics and Rock Engineering.

Singh, U. K., & Digby, P. J. (1989a). A continuum damage model for simulation of the progressive failure of brittle rocks. *International Journal of Solids and Structures*, *25*(6), 647–663. https://doi.org/10.1016/0020-7683(89)90031-0

Singh, U. K., & Digby, P. J. (1989b). The application of a continuum damage model in the finite element simulation of the progressive failure and localization of deformation in brittle rock structures. *International Journal of Solids and Structures*, *25*(9), 1023–1038. https://doi.org/10.1016/0020-7683(89)90019-X

Stephansson, O. (1983a). Rock Stress Measurement By Sleeve Fracturing. *5th ISRM Congress*. Melbourne, Australia: International Society for Rock Mechanics and Rock Engineering. Retrieved from https://doi.org/

Stephansson, O. (1983b). Sleeve fracturing for rock stress measurement in boreholes. *International Symposium Soil and Rock Investigations by In-Situ Testing : 18/05/1983 - 20/05/1983*. Luleå tekniska universitet. Retrieved from

http://urn.kb.se/resolve?urn=urn:nbn:se:ltu:diva-28453

Stephansson, Ove. (1993). Rock stress in the Fennoscandian shield. In *Rock Testing and Site Characterization* (pp. 445–459). Elsevier.

Zoback, M. D. (2007). *Reservoir geomechanics*. *Cambridge University Press*.

Zoback, M. D., & Healy, J. H. (1992). In situ stress measurements to 3.5 km depth in the Cajon Pass scientific research borehole: Implications for the mechanics of crustal faulting. *Journal of Geophysical Research: Solid Earth*, *97*(B4), 5039–5057.

Zoback, M. D., Moos, D., Mastin, L., & Anderson, R. N. (1985). Well Bore Breakouts and in Situ Stress. *Journal of Geophysical Research*, *90*(B7), 5523–5530. https://doi.org/10.1029/JB090iB07p05523

Zoback, M. L., Zoback, M. D., Adams, J., Assumpção, M., Bell, S., Bergman, E. A., et al. (1989). Global patterns of tectonic stress. *Nature*, *341*(6240), 291–298. https://doi.org/10.1038/341291a0

Chapter 3

Anelastic Strain Recovery Method for In-situ Stress Measurement

3.1 History of ASR method

When a rock core sample is retrieved from a borehole, two strain recovery (SR) processes occur on the core sample: elastic strain recovery (instantaneously recovering strain) and anelastic strain recovery (time-dependent recovering strain, ASR). Anelastic strain recovery method is an in-situ stress measuring technique based on rock cores' ASR data.

Voight (1968) first realized that ASR was able to be used to measure in-situ stress. Voight (1968) suggested if partial recovery of strains is assumed to be proportional to total recovery of strain, in-situ stress estimation can be conducted by instrumenting an oriented drilled core immediately after its removal The first success in using ASR for determining the directions and rations of in-situ stresses was reported by Teufel (1982). In his paper, good agreement was obtained between horizontal principal stress directions inferred from ASR measurements and the azimuth of hydraulic fractures in volcanic tuff at the Nevada Test Site in the USA. After the success, a lot of researches were conducted applying the same technique to the different geological settings and good agreements were found between ASR results and other stress measurements (Perreau et al., 1989; Smith et al., 1986; Teufel & Farrell, 1990; Warpinski & Teufel, 1989a).

To determine the magnitude of stress using the ASR method, a constitutive

viscoelastic model for ASR is required. Blanton (1983) first derived the two dimensional constitutive equation of ASR for isotropic and transversely isotropic rocks, where the direction of one of the principal stresses is assumed to be vertical. After the first derivation, Blanton & Teufel (1983) included the effect of pore pressure in the viscoelastic model. Matsuki (1991) and Matsuki & Takeuchi (1993) extended viscoelastic model to a three dimensional model that can be used to determine both the magnitude and orientation of in-situ stresses from ASR data of reoriented core samples. They showed theoretically that i) for an isotropic and linear viscoelastic material, the directions of the three principal stresses coincide with the directions of the three principal anelastic strains, ii) anelastic normal strain depends on the in-situ stress tensor, the pore pressure and the ASR compliances (recovered ASR after unloading of unit stress) of volumetric and shear deformations. Therefore, the directions of the in-situ principal stresses can be determined by the calculation of the directions of the principal anelastic strains. Recently, many studies have adopted the three dimensional method to perform stress measurements (Byrne et al., 2009; Lin et al., 2007; Nagano et al., 2014; Oohashi et al., 2017; Sun et al., 2017; Yamamoto et al., 2013).

3.2 Constitutive equation of ASR

In this section, the constitutive equation of ASR is described. The derivation of the constitutive equation is based on Matsuki & Takeuchi (1993). In the theory of the ASR method, rock samples are modeled as linear viscoelastic material of Voight. In addition, the rock is assumed to be homogeneous and isotropic. According to viscoelastic theory, the general constitutive equation of isotropic material is given by

$$\begin{aligned} P_{\mathrm{S}} s_{ij}(t) &= Q_{\mathrm{S}} e_{ij}(t) \\ P_{\mathrm{V}} \sigma_{\mathrm{m}}(t) &= Q_{\mathrm{V}} \varepsilon_{\mathrm{m}}(t), \end{aligned} \tag{3-1}$$

where σ_{ij} is constant in-situ stress, $\sigma_{\mathrm{m}} = \sigma_{ll}/3$ is mean normal stress, $s_{ij} = \sigma_{ij} - \sigma_{\mathrm{m}}$ is deviatoric stress, ε_{ij} is measured anelastic strain recovery, $\varepsilon_{\mathrm{m}} = \varepsilon_{ll}/3$ is mean

normal anelastic strain and $e_{ij} = \varepsilon_{ij} - \varepsilon_{\mathrm{m}}$ is anelastic deviatoric strain. In this thesis, Einstein summation convention is adopted. That is, when an index variable appears twice in a single term, it implies summation of that term over all the values of the index. In this section, $i,\ j = 1, 2, 3$.

The suffixes V and S means volumetric and shear mode respectively. P_{V}, Q_{V}, P_{S}, Q_{S} are

$$\begin{aligned} P_{\mathrm{S}} &= a_0 + a_1\frac{\mathrm{d}}{\mathrm{d}t} + a_2\frac{\mathrm{d}^2}{\mathrm{d}t^2} + \cdots + a_n\frac{\mathrm{d}^n}{\mathrm{d}t^n} = \sum_{i=0}^{n} a_i\frac{\mathrm{d}^i}{\mathrm{d}t^i} \\ Q_{\mathrm{S}} &= b_0 + b_1\frac{\mathrm{d}}{\mathrm{d}t} + b_2\frac{\mathrm{d}^2}{\mathrm{d}t^2} + \cdots + b_n\frac{\mathrm{d}^n}{\mathrm{d}t^n} = \sum_{i=0}^{n} b_i\frac{\mathrm{d}^i}{\mathrm{d}t^i} \\ P_{\mathrm{V}} &= \alpha_0 + \alpha_1\frac{\mathrm{d}}{\mathrm{d}t} + \alpha_2\frac{\mathrm{d}^2}{\mathrm{d}t^2} + \cdots + \alpha_n\frac{\mathrm{d}^n}{\mathrm{d}t^n} = \sum_{i=0}^{n} \alpha_i\frac{\mathrm{d}^i}{\mathrm{d}t^i} \\ Q_{\mathrm{V}} &= \beta_0 + \beta_1\frac{\mathrm{d}}{\mathrm{d}t} + \beta_2\frac{\mathrm{d}^2}{\mathrm{d}t^2} + \cdots + \beta_n\frac{\mathrm{d}^n}{\mathrm{d}t^n} = \sum_{i=0}^{n} \beta_i\frac{\mathrm{d}^i}{\mathrm{d}t^i}. \end{aligned} \tag{3-2}$$

The constant coefficients a_i, b_i, α_i and β_i are related to the elastic and viscosity modulus of the material, which are determined from physical experiments. By applying Laplace transformation

$$\mathcal{L}[f(t)] = \bar{f}(s) = \int_0^{\infty} f(t)\mathrm{e}^{-st}\mathrm{d}t \tag{3-3}$$

to (3-1), we have following viscoelastic constitutive equation in the Laplace domain:

$$\begin{aligned} P_{\mathrm{S}}(s)\bar{s}_{ij}(s) &= Q_{\mathrm{S}}(s)\bar{e}_{ij}(s) \\ P_{\mathrm{V}}(s)\bar{\sigma}_{\mathrm{m}}(s) &= Q_{\mathrm{V}}(s)\bar{\varepsilon}_{\mathrm{m}}(s) \end{aligned} \tag{3-4}$$

or

$$\begin{aligned} \bar{s}_{ij}(s) &= \bar{J}_{\mathrm{S}}(s)\bar{e}_{ij}(s) \\ \overline{\sigma_{\mathrm{m}}}(s) &= \bar{J}_{\mathrm{V}}(s)\overline{\varepsilon_{\mathrm{m}}}(s), \end{aligned} \tag{3-5}$$

where

$$\begin{aligned} P_{\mathrm{S}}(s) &= a_0 + a_1 s + a_2 s^2 + \cdots + a_n s^n + R_1 = \sum_{i=0}^{n} a_i s^i + R_1 \\ Q_{\mathrm{S}}(s) &= b_0 + b_1 s + b_2 s^2 + \cdots + b_n s^n + R_2 = \sum_{i=0}^{n} b_i s^i + R_2 \\ P_{\mathrm{V}}(s) &= \alpha_0 + \alpha_1 s + \alpha_2 s^2 + \cdots + \alpha_n s^n + R_3 = \sum_{i=0}^{n} \alpha_i s^i + R_3 \\ Q_{\mathrm{V}}(s) &= \beta_0 + \beta_1 s + \beta_2 s^2 + \cdots + \beta_n s^n + R_4 = \sum_{i=0}^{n} \beta_i s^i + R_4 \end{aligned} \tag{3-6}$$

and

$$\begin{aligned} \bar{J}_{\mathrm{S}}(s) &= \frac{P_{\mathrm{S}}(s)}{Q_{\mathrm{S}}(s)} \\ \bar{J}_{\mathrm{V}}(s) &= \frac{P_{\mathrm{V}}(s)}{Q_{\mathrm{V}}(s)}, \end{aligned} \tag{3-7}$$

where s is Laplace variable and R_i $(i = 1\sim4)$ are values determined by initial values of stress and strain. J_{S}, and J_{V} are called anelastic strain recovery compliances of shear and volumetric modes respectively.

According to correspondence principle (Flügge, 1975), the solution for a viscoelastic problem is obtained by replacing the elastic constants in the solution of the corresponding elastic problem with viscoelastic coefficients. The constitutive equations of an isotropic elastic material are

$$\begin{aligned} s_{ij} &= 2G\hat{e}_{ij} \\ \sigma_{\mathrm{m}} &= 3K\hat{\varepsilon}_{\mathrm{m}}, \end{aligned} \tag{3-8}$$

where $\hat{e}_{ij}$ is elastic deviatoric strain, $\hat{\varepsilon}_{\mathrm{m}}$ is elastic mean strain, G is shear modulus and K is bulk modulus. From (3-5) and (3-8), viscoelastic solutions are led by following replacement:

$$\begin{aligned} 2G &\leftrightarrow \frac{Q_{\mathrm{S}}(s)}{P_{\mathrm{S}}(s)} \\ 3K &\leftrightarrow \frac{Q_{\mathrm{V}}(s)}{P_{\mathrm{V}}(s)} \end{aligned} \tag{3-9}$$

and then

$$\begin{aligned} E &\leftrightarrow \frac{3Q_{\mathrm{S}}(s)Q_{\mathrm{V}}(s)}{2P_{\mathrm{S}}(s)Q_{\mathrm{V}}(s) + Q_{\mathrm{S}}(s)P_{\mathrm{V}}(s)} \\ \nu &\leftrightarrow \frac{P_{\mathrm{S}}(s)Q_{\mathrm{V}}(s) - P_{\mathrm{V}}(s)Q_{\mathrm{S}}(s)}{2P_{\mathrm{S}}(s)Q_{\mathrm{V}}(s) + Q_{\mathrm{S}}(s)P_{\mathrm{V}}(s)}, \end{aligned} \tag{3-10}$$

where E is the Young's modulus and ν is the Poisson's ratio.
The corresponding equation of elastic strain is given by the following equation:

$$\hat{\varepsilon}_{ij} = \frac{1}{E}\sigma_{ij} + \frac{\nu}{E}\left[\sigma_{ij} - 3\sigma_{\mathrm{m}}\delta_{ij}\right] - \frac{1}{3}\left(\frac{1}{K} - \frac{1}{K_{\mathrm{S}}}\right)p\delta_{ij} - \alpha\delta_{ij}\Delta T, \tag{3-11}$$

where K_{S} is bulk modulus of matrix, p is pore pressure, ΔT is temperature change, α is the coefficient of linear thermal expansion, which is assumed to be scalar. Therefore, the corresponding equation of elastic normal strain in direction $\mathbf{n}$ is given by the following equation:

$$\hat{\varepsilon}_{\mathrm{n}} = \frac{1}{E} n_i n_j \sigma_{ij} + \frac{\nu}{E}\left[n_i n_j \sigma_{ij} - 3\sigma_{\mathrm{m}}\right] - \frac{1}{3}\left(\frac{1}{K} - \frac{1}{K_{\mathrm{S}}}\right) p - \alpha \Delta T, \tag{3-12}$$

where $\hat{\varepsilon}_{\mathrm{n}}$ is elastic normal strain and n_i is the component of the directional cosine vector of measured normal strain. $|\mathbf{n}| = n_l n_l = 1$.

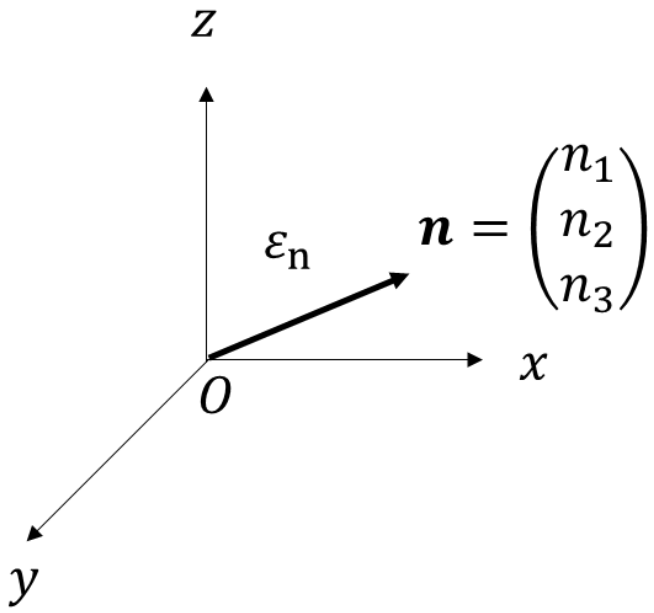

Fig. 3-1 Normal strain in an arbitrary direction in a viscoelastic body. **n** is the directional cosine vector indicating the direction of the measured strain.

By applying the replacement (3-10), we have the equation of anelastic normal strain in the Laplace domain:

$$\begin{aligned} \bar{\varepsilon}(s, \mathbf{n}) = {} & \frac{2P_{\mathrm{S}}(s)Q_{\mathrm{V}}(s) + Q_{\mathrm{S}}(s)P_{\mathrm{V}}(s)}{3Q_{\mathrm{S}}(s)Q_{\mathrm{V}}(s)} n_i n_j \overline{\sigma_{ij}}(s) \\ & + \frac{P_{\mathrm{S}}(s)Q_{\mathrm{V}}(s) - P_{\mathrm{V}}(s)Q_{\mathrm{S}}(s)}{3Q_{\mathrm{S}}(s)Q_{\mathrm{V}}(s)} \left(n_i n_j \overline{\sigma_{ij}}(s) - 3\overline{\sigma_{\mathrm{m}}}(s)\right) \\ & - \frac{1}{3}\left(\frac{3P_{\mathrm{V}}(s)}{Q_{\mathrm{V}}(s)} - \frac{1}{K_{\mathrm{S}}}\right) \bar{p}(s) - \alpha \overline{\Delta T}(s), \end{aligned} \tag{3-13}$$

where it is assumed that K_S is not a viscoelastic parameter (Warpinski & Teufel, 1989b). Using (3-7), (3-13) becomes

$$\bar{\varepsilon}(s,\mathbf{n}) = \bar{J}_S(s)\left(n_i n_j \overline{\sigma_{ij}}(s) - \overline{\sigma_m}(s)\right) + \bar{J}_V(s)\left(\overline{\sigma_m}(s) - \bar{p}(s)\right) + \frac{\bar{p}(s)}{3K_S} - \alpha\overline{\Delta T}(s). \tag{3-14}$$

In applying ASR method, in-situ stress and pore pressure are assumed to relieve stepwise at time $t = 0$. Therefore

$$\sigma_{ij}(t) = \begin{cases} \sigma_{ij} & (t < 0) \\ 0 & (t \geq 0) \end{cases}$$
$$p(t) = \begin{cases} p & (t < 0) \\ 0 & (t \geq 0) \end{cases}. \tag{3-15}$$

By using Laplace inverse transformation

$$\mathcal{L}^{-1}[\bar{f}(s)] = \frac{1}{2\pi i}\lim_{T\to\infty}\int_{\gamma-iT}^{\gamma+iT} \mathrm{e}^{st}\,\bar{f}(s)\mathrm{d}s \tag{3-16}$$

the equation of anelastic normal strain recovery, which is the fundamental equation of ASR theory is given:

$$\varepsilon(t,\mathbf{n}) = \left(\sigma_{ij}n_i n_j - \sigma_m\right)J_S(t) + (\sigma_m - p_0)J_V(t). \tag{3-17}$$

From (3-17), anelastic mean normal strain is given by

$$\varepsilon_m(t) = (\sigma_m - p)J_V(t) - \alpha\Delta T(t) \tag{3-18}$$

and anelastic deviatoric strains are given by

$$e_{ij}(t) = s_{ij} J_S(t). \tag{3-19}$$

From (3-19), the characteristic polynomial of the s_{ij} is

$$\begin{aligned} \det(s\delta_{ij} - s_{ij}) &= \det\left(s\delta_{ij} - \frac{e_{ij}(t)}{J_S(t)}\right) \\ &= J_S(t)^{-3} \det\left(sJ_S(t)\delta_{ij} - e_{ij}(t)\right), \end{aligned} \tag{3-20}$$

where δ_{ij} is delta function

$$\delta_{ij} = \begin{cases} 0 \ (i \neq j) \\ 1 \ (i = j) \end{cases}. \tag{3-21}$$

This means the three eigenvectors of s_{ij} are the same as that of $e_{ij}(t)$, that is, the directions of the principal deviatoric stresses are correspond to those of the principal anelastic deviatoric strains. Therefore, we are able to determine the in-situ stress orientations from the orientations of the anelastic strain.

3.3 Determination of in-situ Stress Tensor

In the conventional ASR method, the orientations and magnitudes of principal stresses are determined separately.

3.3.1 Orientation of principal stresses

We first calculate the three-dimensional strain tensor from the measured nine normal strain recoveries. The relation between normal strains in the direction of an **n** vector and

the six components of three-dimensional strain tensor are given as follow:

$$\begin{aligned}\varepsilon(t,\mathbf{n}) &= n_i n_j \varepsilon_{ij}(t) \\ &= l^2\varepsilon_{11}(t) + m^2\varepsilon_{22}(t) + n^2\varepsilon_{33}(t) + 2lm\varepsilon_{12}(t) \\ &\quad + 2mn\varepsilon_{23}(t) + 2nl\varepsilon_{13}(t).\end{aligned} \tag{3-22}$$

If we measure the anelastic normal strain recovery in k directions, we have following matrix equation:

$$\begin{pmatrix} l_1^2 & m_1^2 & n_1^2 & 2l_1m_1 & 2m_1n_1 & 2n_1l_1 \\ l_2^2 & m_2^2 & n_2^2 & 2l_2m_2 & 2m_2n_2 & 2n_2l_2 \\ \vdots & \vdots & \vdots & \vdots & \vdots & \vdots \\ l_k^2 & m_k^2 & n_k^2 & 2l_km_k & 2m_kn_k & 2n_kl_k \end{pmatrix} \begin{pmatrix} \varepsilon_{11}(t) \\ \varepsilon_{22}(t) \\ \varepsilon_{33}(t) \\ \varepsilon_{12}(t) \\ \varepsilon_{23}(t) \\ \varepsilon_{13}(t) \end{pmatrix} = \begin{pmatrix} \varepsilon(t,\mathbf{n}_1) \\ \varepsilon(t,\mathbf{n}_2) \\ \vdots \\ \varepsilon(t,\mathbf{n}_k) \end{pmatrix} \tag{3-23}$$

or

$$[n]\left(\varepsilon_{ij}(t)\right) = \left(\varepsilon(t,\mathbf{n}_i)\right). \tag{3-24}$$

We want to know the six components of the strain tensor $\varepsilon_{ij}(t)$ from (3-23) or (3-24). If the number of k is larger than six, i.e. the anelastic normal strains are measured in six independent directions, this inverse problem becomes well-posed problem and can be solved by least squares method. The calculated six components of the strain tensor are given by

$$\left(\varepsilon_{ij}(t)\right) = ([n]^T[n])^{-1}[n]^T\left(\varepsilon(t,\mathbf{n}_i)\right). \tag{3-25}$$

Three principal strains are calculated from the strain tensor given by (3-25).

3.3.2 Magnitude of principal stresses

From (3-19), the relations between the magnitudes of anelastic principal deviatoric strains e_i and those of principal deviatoric stresses s_i are given by

$$s_i = \frac{e_i(t)}{J_S(t)} \ (i = 1, 2, 3) \tag{3-26}$$

and then the relations between the magnitudes of principal stresses and these of anelastic strains are given:

$$\sigma_i = \frac{e_i(t)}{J_S(t)} + \frac{\varepsilon_m(t)}{J_V(t)} + p_0, \tag{3-27}$$

where σ_i and e_i ($i = 1, 2, 3$) represent the magnitudes of principal stresses and anelastic principal deviatoric strains, respectively. Here, stress is defined as $\sigma_1 > \sigma_2 > \sigma_3$ with compression being positive, and strain recovery is defined as $e_1 > e_2 > e_3$ with expansion being positive. In the conventional method, the stress tensor can be calculated by determining J_S, J_V, and p_0 in addition to ε_{ij}. ASR compliances J_S and J_V should be measured by conducting a triaxial compression test on the rock core used for the ASR measurement. However, it has been suggested by Matsuki & Takeuchi (1993) that ASR compliances depend on the magnitude of mean normal stress, which generally makes the measurement difficult to conduct in the laboratory.

To determine the in-situ stress tensor using (3-27), it is necessary to know the ASR compliance J_S and J_V of the core samples used. In the conventional method, therefore, the in-situ stress tensor is calculated using the ratio of ASR compliances $r = J_V/J_S$, vertical stress σ_v and pore pressure p_0. These values are determined as follows: Using eq. (3), the vertical stress σ_v is calculated as follows:

$$\begin{aligned}\sigma_{\mathrm{v}} &= \sigma_1 l_1^2 + \sigma_2 l_2^2 + \sigma_3 l_3^2 \\ &= \frac{1}{J_{\mathrm{V}}(t)}\Big(r(t) l_i l_j e_{ij}(t) + \varepsilon_{\mathrm{m}}(t)\Big) + p_0.\end{aligned} \tag{3-28}$$

In (3-28), the principal strain coordinate system is used as the basis, and $\mathbf{l} = (l_1, l_2, l_3)^{\mathrm{T}}$ is the directional cosine vector in the vertical direction with respect to the coordinate system. ASR compliances can be expressed using r and σ_{v}

$$\begin{aligned}J_{\mathrm{V}}(t) &= \frac{\Big(r(t) l_i l_j e_{ij}(t) + \varepsilon_{\mathrm{m}}(t)\Big)}{(\sigma_{\mathrm{v}} - p_0)} \\ J_{\mathrm{S}}(t) &= \frac{1}{r(t)} J_{\mathrm{V}}(t).\end{aligned} \tag{3-29}$$

In the conventional method, r is usually assumed to be the constant r_{c}, and r_{c}=0.64±0.14, which is the value at 14 hours after measurement was initiated, as determined by Matsuki (2008) for six rocks, is used. In (3-29), it is also necessary to determine the values of σ_{v} and p_0. In Yamamoto et al. (2013), the vertical stress σ_{v} was assumed to be equal to $\rho_{\mathrm{r}} g h$, the overburden stress was calculated using the average wet density of the rocks above the measurement point (sampling depth), and the pore pressure p_0 was assumed to be equal to the hydrostatic pressure $\rho_{\mathrm{w}} g h_{\mathrm{w}}$, where g is the gravitational acceleration, h is the depth of the measurement point, h_{w} is the distance between the measurement point and the groundwater surface, and ρ_{r} and ρ_{w} are the average wet density of the rock and water density, respectively. Fig. 3-2 shows the flow chart of the ASR method.

3.4 Challenges of the ASR method

As we have mentioned, the ASR method is a relatively reliable stress measurement method with a clear theoretical background. Meanwhile, the ASR method has some

challenges to be solved as described below. As mentioned above, in order to determine the stress magnitude, it is necessary to assume that the ASR compliance ratio is constant regardless of the rock type. However, this assumption has not been confirmed for all rock types, so the validity of the assumption is still open to debate. An analysis method that does not require such an assumption is considered necessary.

Current ASR method assumes that the rock to be analyzed is isotropic. However, this assumption does not necessarily apply to sedimentary rocks, where orthotropic anisotropy tends to prevail. Therefore, there is a need for an analysis method that can take anisotropy into account.

Thus, the ASR method is a useful stress measurement method, but it has many challenges to be solved. In this study, I aimed to solve these challenges.

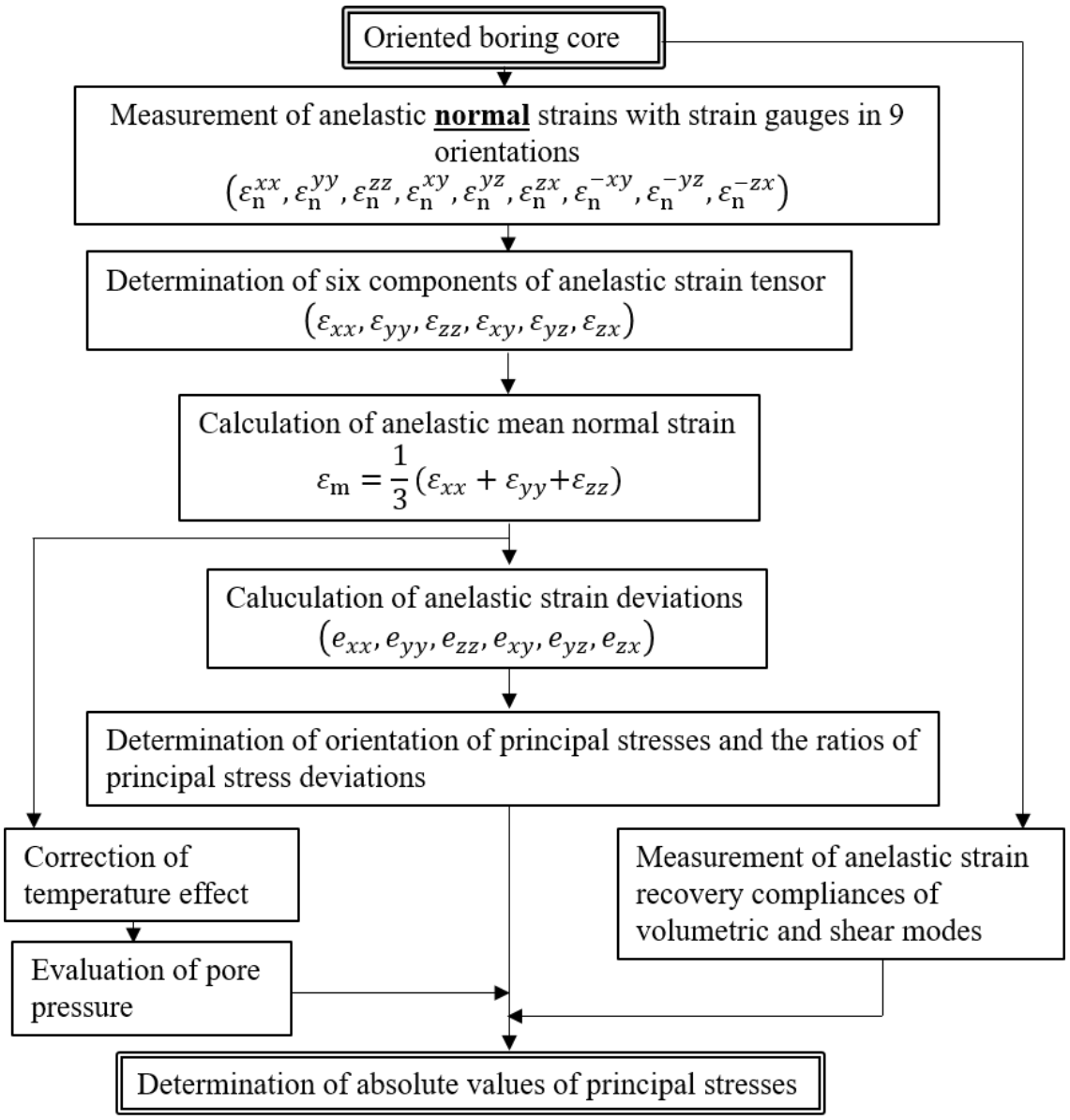

Fig. 3-2 Flow chart of the ASR method. (After Matsuki & Takeuchi 1993).

References

Blanton, T. L. (1983). The Relation Between Recovery Deformation and In-Situ Stress Magnitudes. *SPE/DOE Low Permeability Gas Reservoirs Symposium*. Denver, Colorado: Society of Petroleum Engineers. https://doi.org/10.2118/11624-MS

Blanton, T. L., & Teufel, L. W. (1983). A Field Test of the Strain Recovery Method of Stress Determination in Devonian Shale. *SPE Eastern Regional Meeting*. Pittsburgh, Pennsylvania: Society of Petroleum Engineers. https://doi.org/10.2118/12304-MS

Byrne, T. B., Lin, W., Tsutsumi, A., Yamamoto, Y., Lewis, J. C., Kanagawa, K., et al. (2009). Anelastic strain recovery reveals extension across SW Japan subduction zone. *Geophysical Research Letters*, *36*(23), 1–6. https://doi.org/10.1029/2009GL040749

Flügge, W. (1975). Viscoelasticity. *Springer-Verlag*, 203. https://doi.org/10.1007/978-3-662-02276-4

Lin, W., Yeh, E. C., Ito, H., Hirono, T., Soh, W., Wang, C. Y., et al. (2007). Preliminary results of stress measurement using drill cores of TCDP Hole-A: An application of anelastic strain recovery method to three-dimensional in-situ stress determination. *Terrestrial, Atmospheric and Oceanic Sciences*, *18*(2), 379–393. https://doi.org/10.3319/TAO.2007.18.2.379(TCDP)

Matsuki, K. (1991). Three-dimensional In-situ Stress Measurement With Anelastic Strain Recovery of a Rock Core. *Proc. 7th Congress ISRM*. Aachen, Germany: International Society for Rock Mechanics and Rock Engineering. Retrieved from https://doi.org/

Matsuki, K. (2008). Anelastic strain recovery compliance of rocks and its application to in situ stress measurement. *International Journal of Rock Mechanics and Mining Sciences*, *45*(6), 952–965. https://doi.org/https://doi.org/10.1016/j.ijrmms.2007.10.005

Matsuki, K., & Takeuchi, K. (1993). Three-dimensional in situ stress determination by anelastic strain recovery of a rock core. *International Journal of Rock Mechanics*

and Mining Sciences & Geomechanics Abstracts, *30*(7), 1019–1022. https://doi.org/https://doi.org/10.1016/0148-9062(93)90064-K

Nagano, Y., Lin, W., & Yamamoto, K. (2014). In-situ stress analysis using the anelastic strain recovery (ASR) method at the first offshore gas production test site in the eastern Nankai Trough, Japan. *Marine and Petroleum Geology*, *66*, 418–424. https://doi.org/10.1016/j.marpetgeo.2015.02.027

Oohashi, K., Lin, W., Wu, H. Y., Yamaguchi, A., & Yamamoto, Y. (2017). Stress State in the Kumano Basin and in Slope Sediment Determined From Anelastic Strain Recovery: Results From IODP Expedition 338 to the Nankai Trough. *Geochemistry, Geophysics, Geosystems*, *18*(10), 3608–3616. https://doi.org/10.1002/2017GC007137

Perreau, P. J., Heugas, O., & Santarelli, F. J. (1989). Tests of ASR, DSCA, and Core Discing Analyses To Evaluate In-Situ Stresses. *Middle East Oil Show*. Bahrain: Society of Petroleum Engineers. https://doi.org/10.2118/17960-MS

Smith, M. B., Ren, N.-K., Sorrells, G. G., & Teufel, L. W. (1986). A Comprehensive Fracture Diagnostics Experiment: Part 2- Comparison of Fracture Azimuth Measuring Procedures. *SPE Production Engineering*, *1*(06), 423–431. https://doi.org/10.2118/13894-PA

Sun, D., Sone, H., Lin, W., Cui, J., He, B., Lv, H., & Cao, Z. (2017). Stress state measured at ~7 km depth in the Tarim Basin, NW China. *Scientific Reports*, *7*(1), 1–10. https://doi.org/10.1038/s41598-017-04516-9

Teufel, L. W. (1982). Prediction Of Hydraulic Fracture Azimuth From Anelastic Strain Recovery Measurements Of Oriented Core. *The 23rd U.S Symposium on Rock Mechanics (USRMS)*. Berkeley, California: American Rock Mechanics Association. Retrieved from https://doi.org/

Teufel, L. W., & Farrell, H. E. (1990). In situ stress and natural fracture distribution in the Ekofisk Field, North Sea. United States. Retrieved from https://www.osti.gov/biblio/6911560

Voight, B. (1968). Determination of Virgin State of Stress in Vicinity of Borehole From Measurements of Partial Anelastic Strain Tensor in Drill Cores. *Felsmechanik u*

Ingenieurgeologie, *6*(4), 201–215.

Warpinski, N. R., & Teufel, L. W. (1989a). In situ stress measurements in nonmarine rocks. *Journal of Petroleum Technology*, *41*, 405–414.

Warpinski, N. R., & Teufel, L. W. (1989b). Viscoelastic constitutive model for determining in-situ stress magnitudes from anelastic strain recovery of core. *SPE Production Engineering*, *4*(3), 272-280 15368.

Yamamoto, Y., Lin, W., Oda, H., Byrne, T., & Yamamoto, Y. (2013). Stress states at the subduction input site, Nankai Subduction Zone, using anelastic strain recovery (ASR) data in the basement basalt and overlying sediments. *Tectonophysics*, *600*, 91–98. https://doi.org/10.1016/j.tecto.2013.01.028

Chapter 4

Core's Reorientation Based on Natural Remanent Magnetization

4.1 Introduction

To determine the orientations of three principal stresses with a core-based stress measuring method, we require the in-situ orientation of an analyzed rock core sample. However, core samples are rotated during conventional drilling and the in-situ orientation is lost. Therefore, we have to restore the in-situ orientation of a core sample. This process is called "reorientation of core sample", and several methods of reorientation have been proposed to restore the in-situ orientation of core samples (Nelson et al., 1987; Shigematsu et al., 2014; Tamaki et al., 2015).

The natural remanent magnetization (NRM) of a core sample has been successfully used for core's reorientation with some variations according to differences in the sample preparation (Byrne et al., 2009; Nagano et al., 2014; Yamamoto et al., 2013). The most common method uses a small cylindrical specimen drilled from a core sample, and the specimen NRM is measured. However, this method cannot estimate measurement errors. To address this problem, I propose a new method of preparing nine small specimens from a single core sample and measuring the NRM of eight of the specimens to obtain a statistical evaluation of the measurement error. While some previous studies have performed NRM measurements on several specimens from a single rock sample (Jin

& Liu, 2010), those studies did not undertake core reorientation.

In this chapter, we first present some basic concepts and definitions used in this chapter and the principle of core reorientation based on NRM, followed by a detailed explanation of specimen preparation from a core sample. An application of the method to hemipelagic sedimentary soft rock core samples is shown as a specific example. I then discuss the results of the application of this method. I also discuss the effects of secondary remanent magnetization owing to drilling process on core reorientation and propose a data quality assessment criterion.

4.2 Background

In this section, several basic definitions and concepts included in this chapter are described.

4.2.1 Geomagnetism

Geomagnetism is the magnetism of the earth and the magnetic field generated by the earth. Most of the geomagnetic field is generated in the earth's outer core. The geomagnetic field is thought to be generated by the electric current generated by the fluid motion of this highly conductive iron, and has been actively studied. However, the details are still unknown.

Geocentric axial dipole model

When averaged over a very long period of time (several thousand years or more), the tilt of the geomagnetic dipole becomes negligible, and the geomagnetic pole can be equated with the geographic pole. Such a dipole at the center of the earth with a magnetic axis coinciding with the axis of rotation is called a geocentric dipole. In this study, the analysis is based on the geocentric axis dipole model.

Reversal of geomagnetism

The geomagnetic field reverses its polarity once every few hundred thousand years. The same polarity as at present, i.e., N pole pointing south, is called normal polarity, and the opposite, N pole pointing north, is called reversed polarity.

4.2.2 Natural remanent magnetization (NRM)

Almost all materials, including rocks, contain ferromagnetic minerals such as iron oxide, which can be magnetized by themselves without the application of an external magnetic field. This is called natural remanent magnetization (NRM). There are multiple mechanisms for the acquisition of NRMs, and the following sections describe the ones relevant to this study.

Thermoremanent magnetization (ThRM)

In general, when a ferromagnetic material is cooled from a temperature above the Curie point while a magnetic field is applied, it acquires a very stable remanent magnetization. This remanent magnetization is called thermal remanent magnetization (ThRM). The strong magnetization of volcanic rocks is the thermal remanent magnetization acquired during the cooling and solidification process of lava in the earth's magnetic field.

Detrital remanent magnetization (DRM)

Sedimentary rocks, such as sandstone and mudstone, acquire magnetization when they are deposited in a magnetic field. This is called detrital remanent magnetization (DRM). The DRM can be classified into two types according to the time of acquisition after deposition: depositional detrital remanent magnetization (dDRM) and post detrital remanent magnetization (pDRM).

The dDRM represents the magnetization acquired during or immediately after deposition. If the consolidation is not so advanced immediately after deposition, the ferromagnetic minerals in the sediment can rotate to magnetize in the direction of the magnetic field in the gap between the nonmagnetic particles. The magnetization that is

acquired in this way is the dDRM.

On the other hand, the pDRM represents the magnetization that is acquired after a while of deposition. This is due to the fact that even if the gap between the nonmagnetic particles becomes small due to the progress of consolidation, the magnetic particles can rotate and align their magnetization in the direction of the magnetic field if their particle shape is small enough.

Viscous remanent magnetization (VRM)

When a ferromagnetic material is subjected to a magnetic field and then returned to zero, it acquires a magnetization called isothermal remanent magnetization (IRM). The longer the magnetic field is applied, the larger the isothermal remanent magnetization becomes in proportion to the logarithm of the time. This magnetization that increases with time in a magnetic field is called viscous remanent magnetization (VRM).

Definitions of inclination and declination in this chapter

Two angles are usually used to represent the NRM orientation, namely, inclination and declination. In this study, declination is defined as the angle between an arbitrary determined reference line and the horizontal NRM component (Fig. 4-1), although it generally refers to the angle between the latter and true north. Inclination is defined as the angle between the horizontal plane and NRM vector.

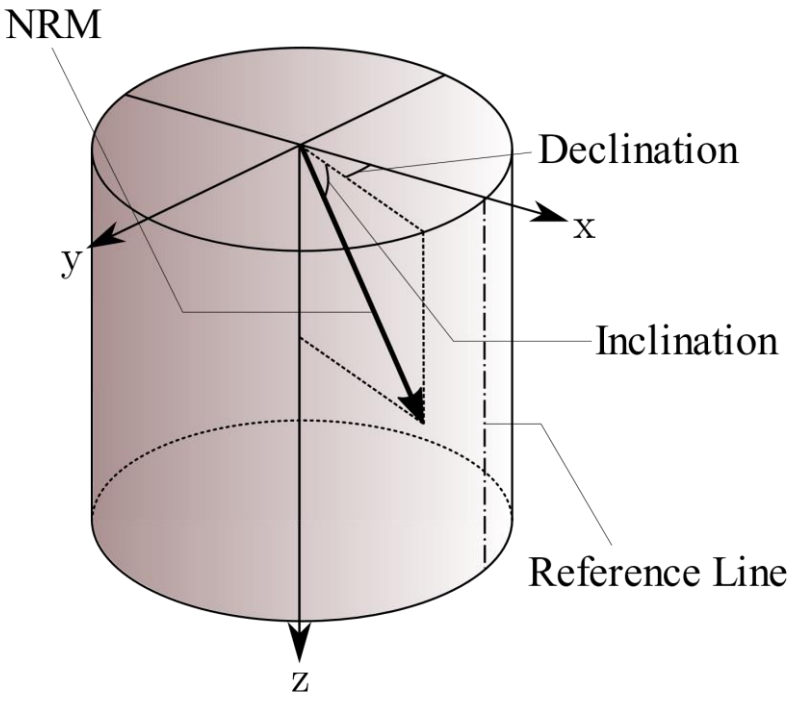

Fig. 4-1 Definitions of inclination and declination.

4.2.3 Demagnetization

After a rock forms and gain primary NRM, it can acquire secondary remanent magnetizations owing to changes in the external environment, such as an artificial magnetic field caused by drilling. This type of remanent magnetization is called secondary NRM. The resultant NRM of a core sample immediately after drilling is a vector sum of primary and secondary NRMs (Fig. 4-2). To reorientate a core sample based on the primary NRM, it is necessary to eliminate the secondary NRM. This process is called demagnetization.

There are two main demagnetization techniques: i) thermal demagnetization (ThD), which demagnetizes secondary NRM by heating a sample in a zero magnetic field; or ii) alternating field demagnetization (AFD), which demagnetizes secondary NRM by applying an alternating magnetic field to a sample in a zero magnetic field.

In this study, we used the AFD technique, which can effectively demagnetize multiple samples simultaneously. The demagnetization process is usually plotted on a Zijderveld diagram, as shown in Fig. 4-3.

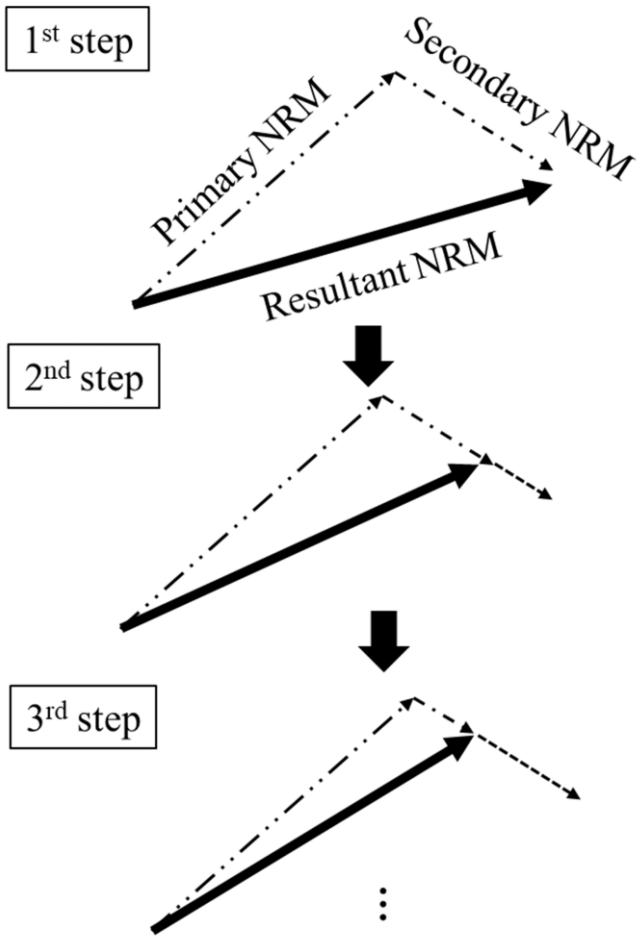

Fig. 4-2 Schematic graph showing progressive demagnetization steps. Two-dot chain lines show primary natural remanent magnetization (NRM). One-dot chain lines show secondary NRM on each demagnetization steps, which are demagnetized in order to extract primary NRM. Black solid lines show sums of primary NRM and secondary NRM (resultant NRM) on each demagnetization steps. Broken lines show demagnetized secondary NRMs. Resultant NRMs are measured on each step and plotted on a Zijderveld diagram.

Two important hypotheses are as follows: i) the measured NRM is the vector sum of primary and secondary NRMs; and ii) demagnetization of primary NRM begins after the secondary NRM is completely demagnetized. Then projections of the vector end points of the primary NRM during the demagnetization process form a line that passes through the origin on the Zijderveld diagram. Previous studies have used this fact to distinguish primary NRM from secondary NRM and we also adopt this approach. To visualize the progressive demagnetization, Zijderveld projection is usually adopted. Fig. 4-3 shows the definition of the plot.

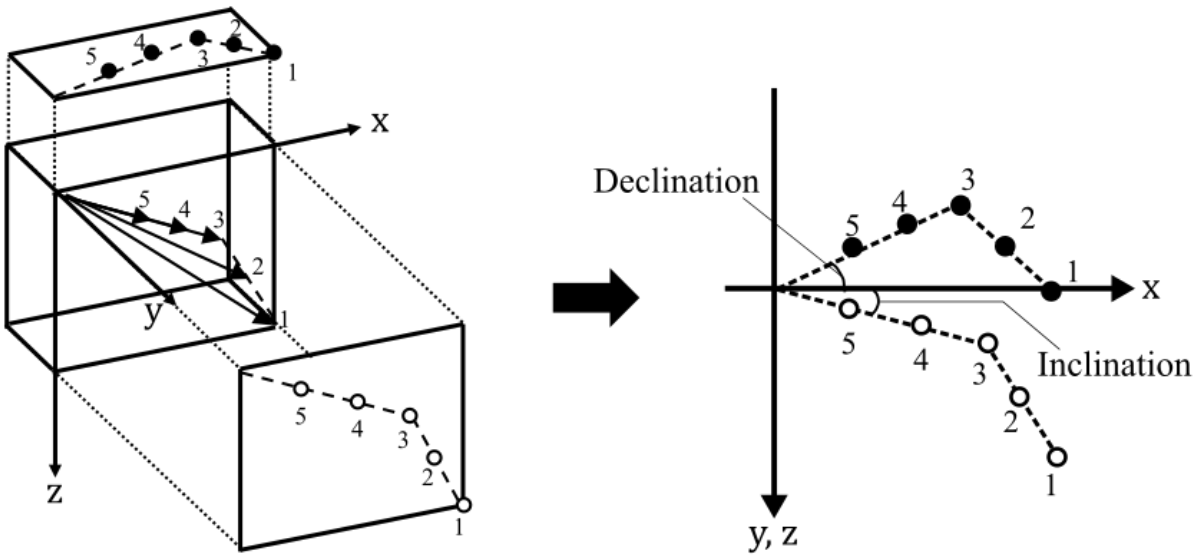

Fig. 4-3 (a) Projections of NRM onto the horizontal and vertical planes. (b) Schematic diagram of a Zijderveld diagram. The numbers in the figures show the number of steps in demagnetization process. Solid black circles are projections of the end points of the NRM vector onto the horizontal plane and open circles are those onto a vertical plane oriented north-south.

4.3 Methodology

In this section, the reorientation method proposed in this research is shown. The method consists of three steps. They are i) sample preparation, ii) demagnetization and measurement of NRM and iii) determination of reorientation rank. Details are shown in the following subsections.

4.3.1 Sample preparation

In the reorientation method proposed in this research, eight specimens cut from one whole round core sample are used to determine the core's in-situ orientation and the rank of the reorientation result. The eight specimens are shaped as follows.

First, a disc-shaped sample with a thickness of about 2 cm is cut from the upper or lower end of the core sample (Fig. 4-4(a)) using a diamond saw. The thickness is determined by the maximum specimen height measured by the NRM-measuring instrument because larger specimen volumes may increase data quality. The disc-shaped sample is then cut into nine specimens, as shown in Fig. 4-4(b). The reasons for separating the disc-shaped sample are 1) limited sample size by the measuring equipment, 2) the remaining core sample can be used for other measurements, 3) the quality of the results can be determined statistically.

When cutting a sample, an IRM can be added owing to the artificial magnetic field around the diamond saw. However, this mainly affects the specimen surface, which is small compared with the total volume (~8 cm^3). In the case that the influence cannot be ignored, the IRM formed from the saw is also considered as a part of the secondary NRM. An assessment of the influence of cutting therefore requires consideration based on the final result. To prevent drying, specimens were wrapped in parafilm (Fig. 4-4(c)). Because the number of specimens that can be simultaneously measured is eight according to the equipment specifications, eight specimens including specimen 1, which is the central specimen shown in Fig. 4-4 (b), are selected from nine specimens. Specimens with sufficient volume are selected.

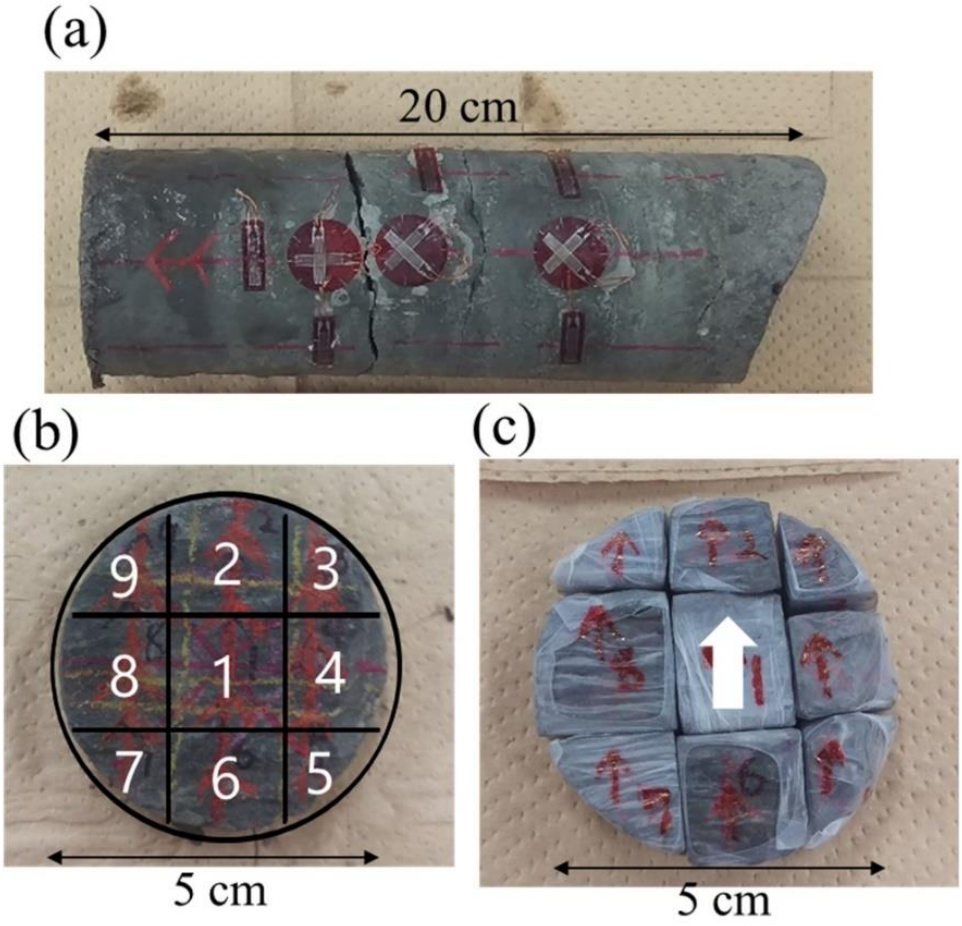

Fig. 4-4 Pictures of sample preparation. (a) A whole round core sample. Strain gages attached to the sample were used for another measurement. (b) A disc-shaped sample cut from a whole round core sample. The numbers show those of specimens used in Fig. 4-9. (c) Specimens wrapped by parafilms. White allow show the direction of the reference line of the whole-round core sample.

4.3.2 Demagnetization and measurement of remanent magnetization

NRM demagnetization and measurement are conducted using Progressive AFD was performed by applying an alternating magnetic field to specimens, typically in 24 steps between 0 and 80 mT. NRM vector end points at each demagnetization step were plotted

on a Zijderveld diagram and the primary NRM was extracted as the line passing through the origin (Fig. 4-3).

It is known that the Earth's magnetic field varies over time and the two angles of primary NRM usually correspond to the averaged direction of the field over time for formation of a rock. If a rock formed over a few thousand years, the geocentric axial dipole hypothesis (Butler, 1992) allows the declination of the primary NRM to be regarded as corresponding to the present geographic north. These two angles were calculated by linear regression analysis on components that linearly decay to the origin on a Zijderveld diagram. In this study, the demagnetizations were conducted with a pass-through superconducting rock magnetometer manufactured by 2-G Enterprise (Model 760R) at Kochi University, Japan (Fig. 4-5).

Fig. 4-5 2-G Enterprise (Model 760R) at Kochi University, Japan.

4.3.3 Determination of rank of reorientation result

This subsection describes the quality assessment of reorientation results, with particular attention given to quantifying the influence of drilling. Reorientation results were classified into three ranks indicating good (A), fair (B), and poor (C) quality according to the following procedures.

Step 1 Determination of rank C

This classification was based on the demagnetization results of specimen 1 (Fig. 4-4 (b)), which was located at the center of the disc-shaped sample and thought to be less influenced by drilling than the other specimens. Rank C is defined if a demagnetized component that does not linearly decay to the origin on the Zijderveld diagram and thus primary NRM is not recognized. Consequently, the core sample cannot be reoriented by NRM analysis. If the line can be confirmed, further analysis is conducted in Step 2.

Step 2 Classification of the remaining results into ranks A or B

If the result is not classified into rank C, that is, primary NRM can be determined in specimen 1, the 95% confidence limit of the mean angle (α_{95}) of the primary NRM (Butler, 1992) is calculated using the demagnetization results from the eight specimens from the same core sample including specimen 1. A result of $\alpha_{95} \leq 5^\circ$ is classified as rank A and $\alpha_{95} > 5^\circ$ as rank B. Rank A results can be used for reorientations without problems. On the other hand, we suggest that the use of rank B results depends on the number of core samples and/or the importance of the location where the sample is retrieved.

4.4 Application to sedimentary soft rock sample

This section shows one of the applications of the NRM-based reorientation method.

4.4.1 Sample information

The core samples used in the case study were retrieved from borehole C0023A during the IODP Expedition 370 (Heuer et al., 2017). C0023A is a vertical borehole located at the toe of the subduction zone of the Nankai Trough about 120 km southeast of Muroto, Kochi (32° 22.00'N, 134° 57.98' E, 4,776 m water depth (Fig. 4-6)). The core samples are composed of Miocene to Quaternary soft sedimentary rocks (Fig. 4-7 and Table 4-1) (430–1123 m below seafloor) with porosities of 25%–45%.

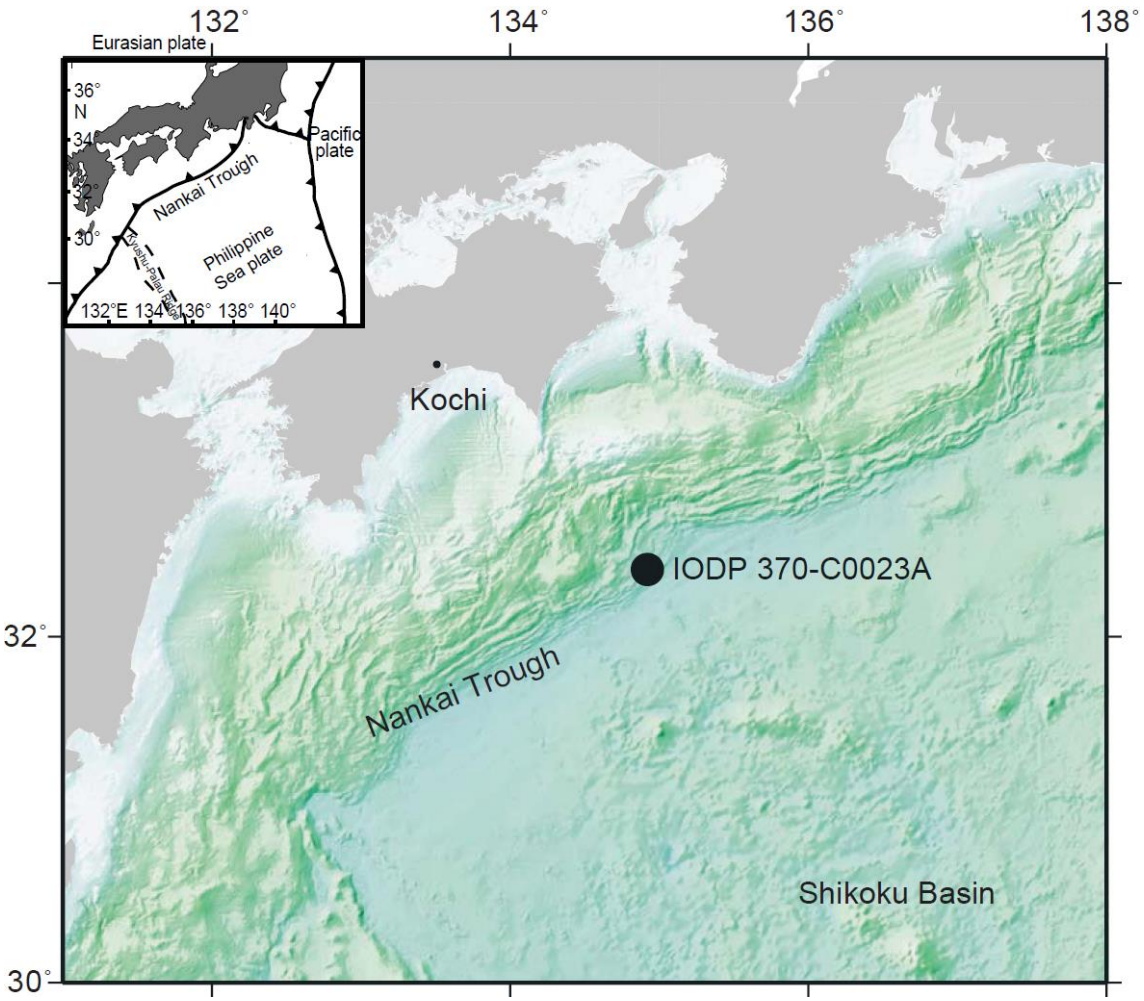

Fig. 4-6 Location of the drilling site named C0023A. (After Heuer et al., 2017.)

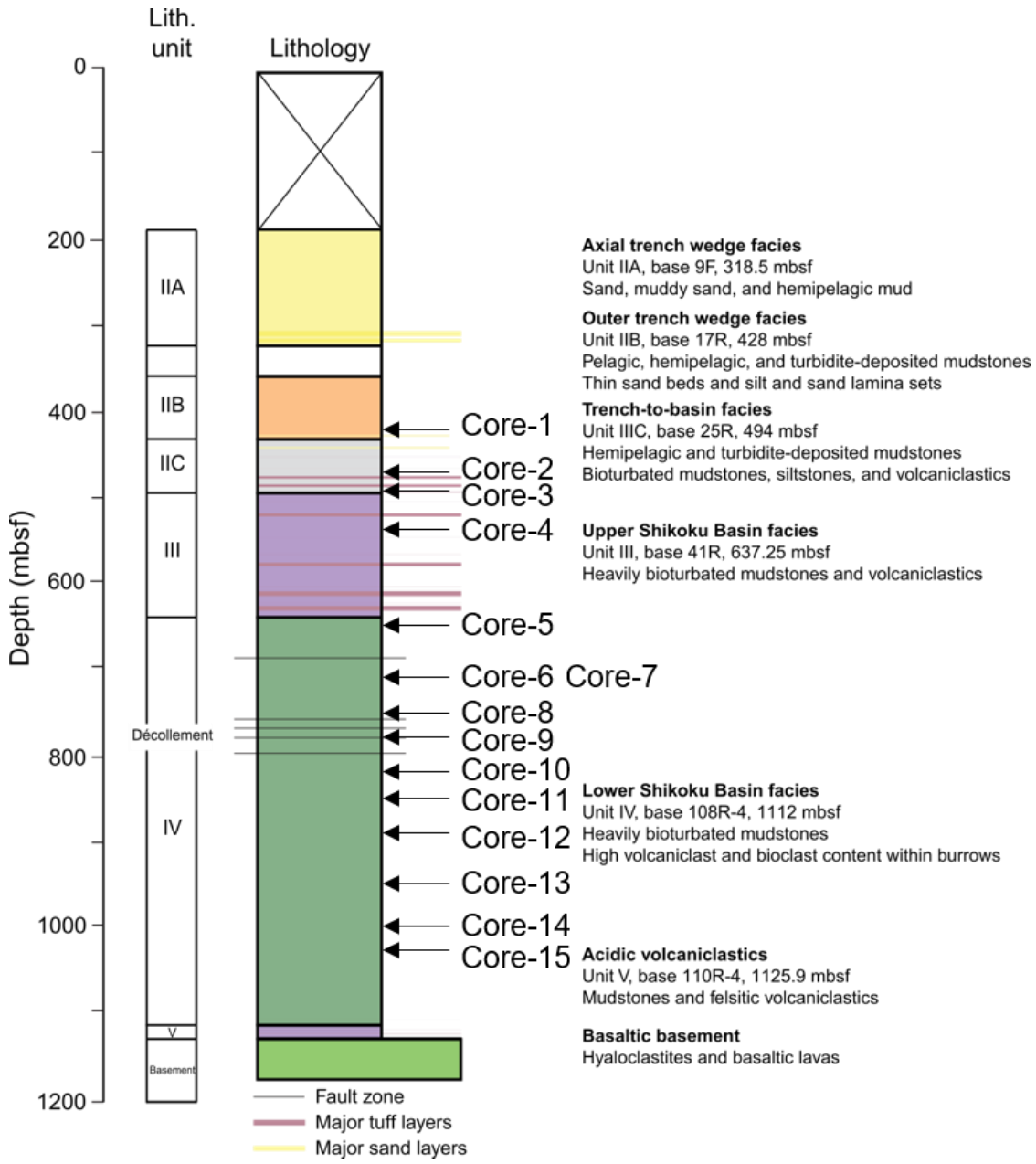

Fig. 4-7 Lithostratigraphy of Hole C0023A and sampling depths. (After Heuer et al., 2017.)

4.4.2 Result

Fig. 4-8 shows the Zijderveld diagram with the demagnetization results of specimen 1 from sample core-1 in each demagnetization step. To extract the primary NRM, a straight line is fitted to a component that linearly decays to the origin. The inclination and declination can be determined from the angles between the lines and the x-axis. Table 4-1

lists the inclinations and declinations obtained from each core sample. Some inclinations show negative values, which are due to magnetization recorded in the reversed polarity chron.

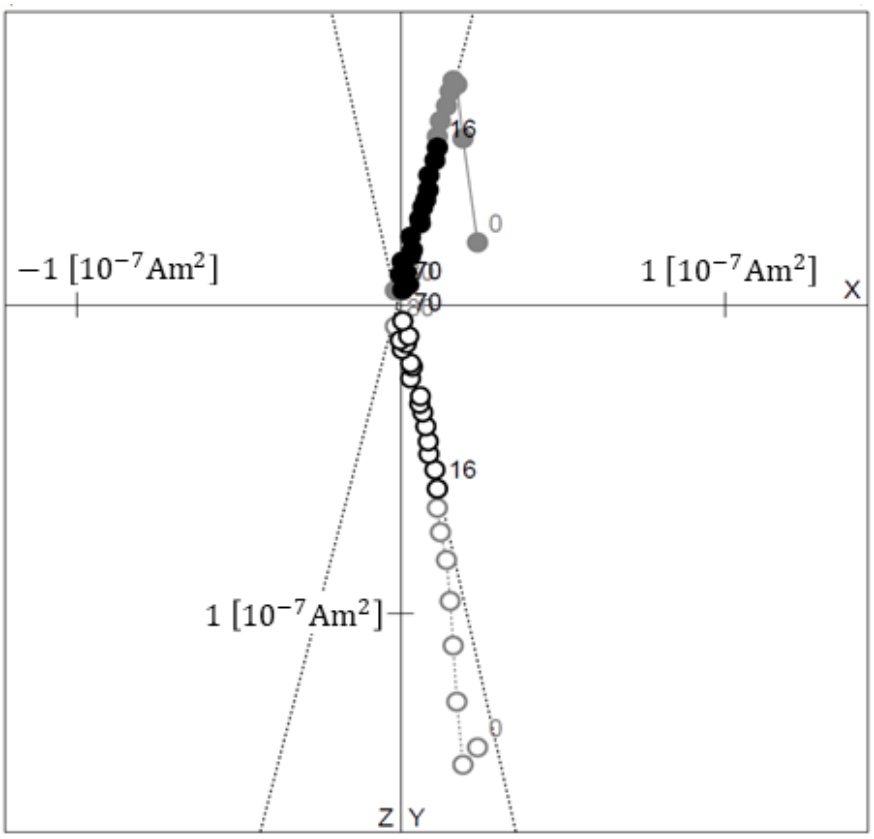

Fig. 4-8 Zijderveld diagram with the demagnetization results of specimen 1 from sample core-1 in each demagnetization step. Black solid circles represent projections of the end points of the NRM vectors in each demagnetization step onto the horizontal plane, and black open circles are those onto a vertical plane oriented north-south. Gray circles (both solid and open) show the secondary components of the NRM vector. The vector length represents the magnetization magnitude. The two black dashed lines in the figure are regression lines fitted to the primary NRM.

Table 4-1 Results of core reorientation based on the Natural Remanent Magnetization Measurements.

Sample ID	IODP core sample source	Core top depth (mbsf)	Inclination (degree)	Declination (degree)	α_{95}	Rank
Core-1	C0023A-18R-1-WR 101.0-121.0 cm	429.01	54.4	286.7	3.8	A
Core-2	C0023A-23R-1-WR 98.0-109.0 cm	475.98	55.6	137.8	3.3	A
Core-3	C0023A-24R-7-WR 25.0-45.0 cm	491.17	45.5	317.1	2.2	A
Core-4	C0023A-33R-7-WR 70.0-85.0 cm	567.13	-52.0	214.5	7.8	C
Core-5	C0023A-43R-5-WR 60.0-81.0 cm	654.87	63.5	215.2	1.8	A
Core-6	C0023A-54R-2-WR 20.0-37.0 cm	713.80	-37.1	36.7	13.7	B
Core-7	C0023A-55R-1-WR 112.0-131.0 cm	718.62	63.4	180.5	4.1	A
Core-8	C0023A-61R-2-WR 0.0-19.0 cm	748.34	56.9	102.2	1.9	A
Core-9	C0023A-67R-1-WR 108.0-121.0 cm	776.08	-16.7	188.5	4.7	A
Core-10	C0023A-77R-2-WR 127.0-146.5 cm	822.02	-17.9	18.2	2.7	A
Core-11	C0023A-81R-4-WR 15.0-35.0 cm	846.48	56.4	290.7	2.4	A
Core-12	C0023A-86R-3-WR 131.0-151.0 cm	892.99	-54.4	117.5	3.8	A
Core-13	C0023A-92R-3-WR 70.0-96.0 cm	950.11	-73.8	156.6	18.4	C
Core-14	C0023A-99R-3-WR 20.0-40.0 cm	1023.11	71.9	116.7	5.3	C
Core-15	C0023A-110R-2-WR 46.0-65.0 cm	1122.74	80.2	71.5	2.5	A

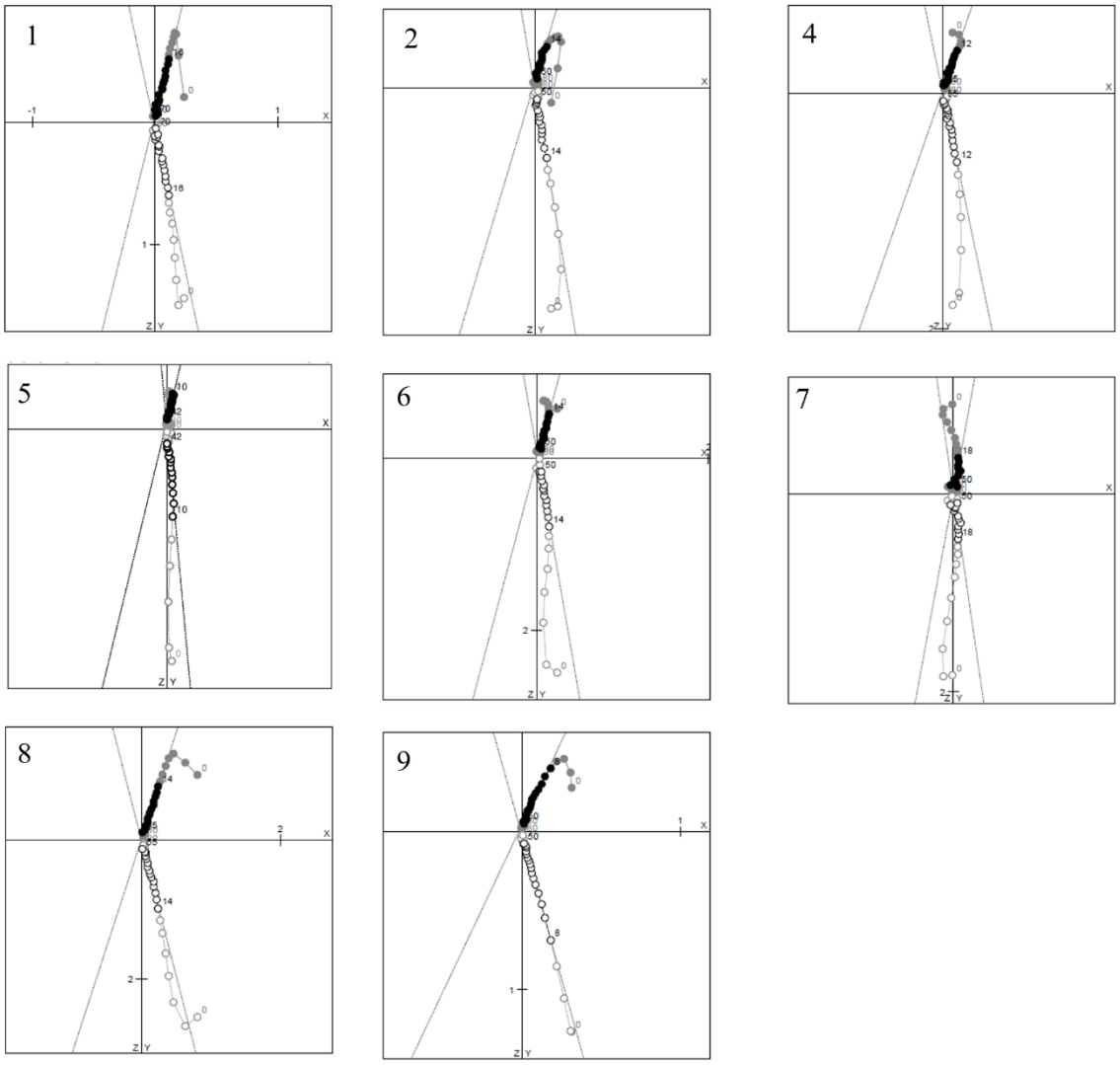

Fig. 4-9 Zijderveld diagrams of NRM obtained from Core-1. The numbers show those of the specimens.

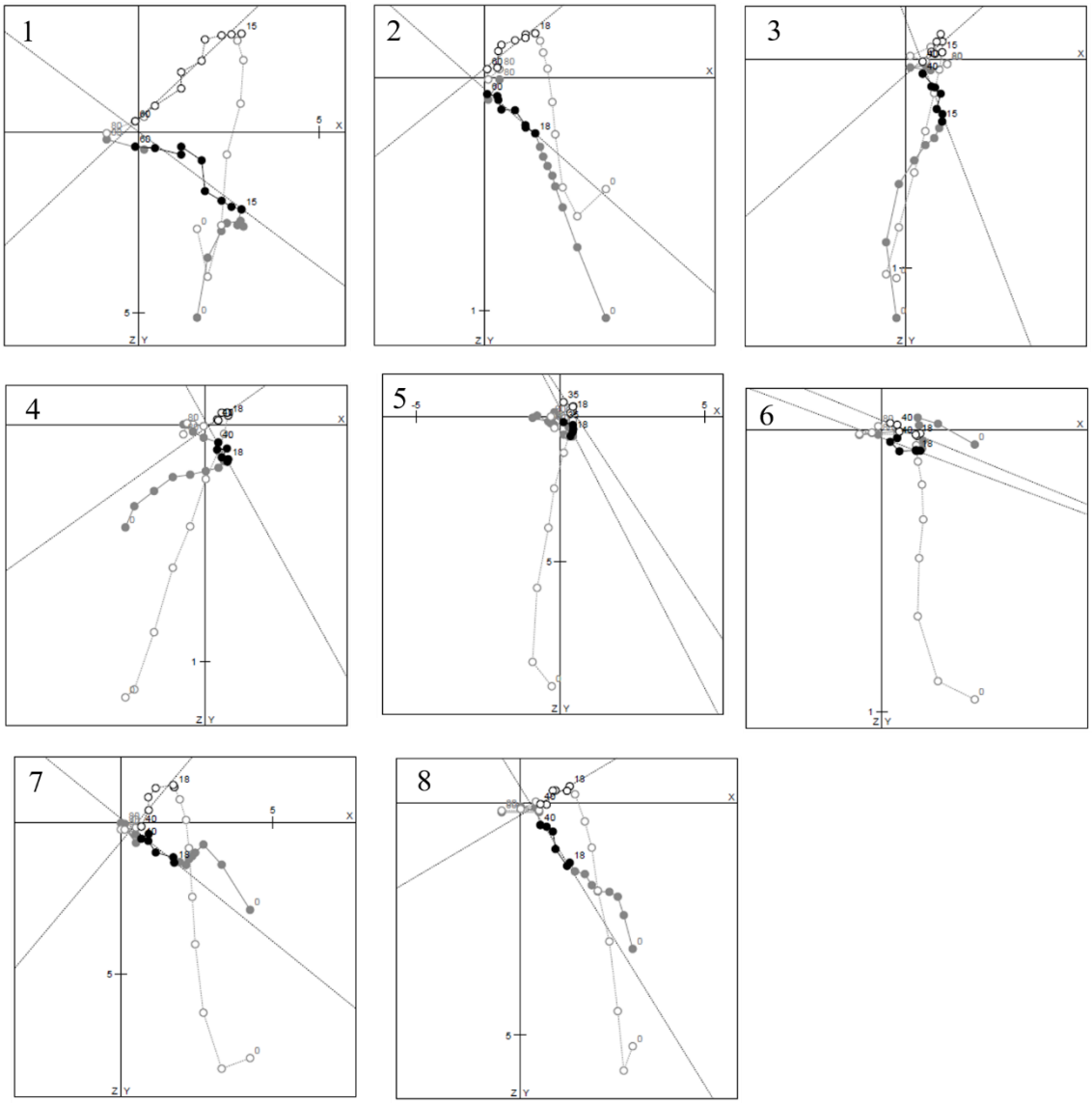

Fig. 4-10 Zijderveld diagrams of NRM obtained from Core-6.

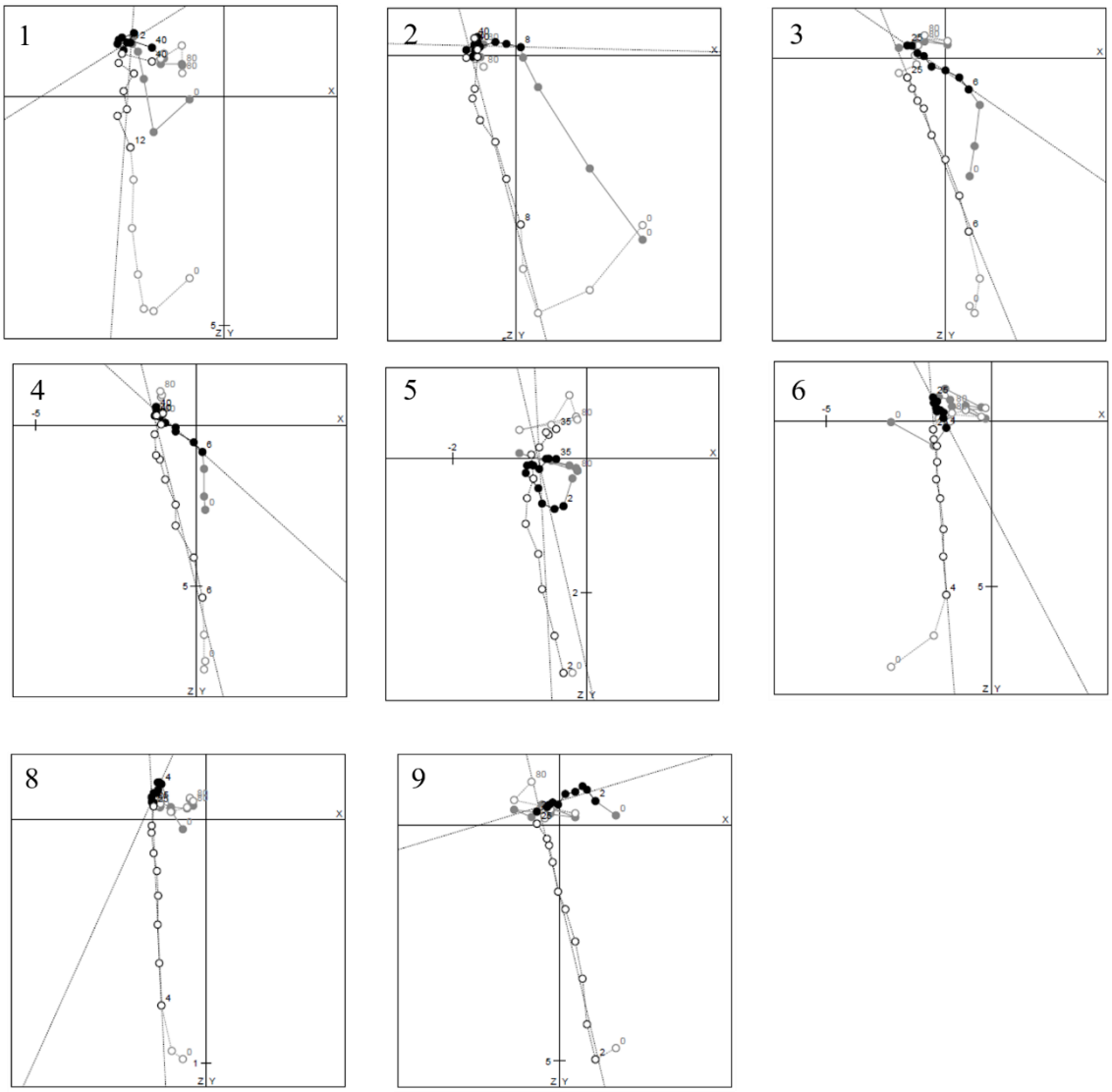

Fig. 4-11 Zijderveld diagrams of NRM obtained from Core-4.

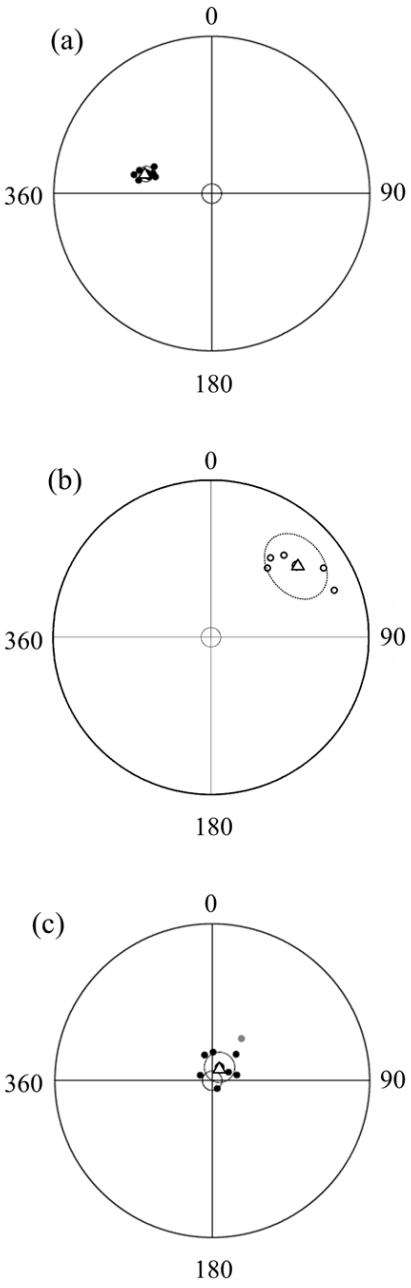

Fig. 4-12 Equal area projections of the primary components of the normalized NRM vectors for (a) Core-1, which has rank A, (b) Core-6, which has rank B and (c) Core-4, which has rank C, respectively. Black solid and open circles indicate lower and upper hemisphere projections, respectively. Gray circles (solid and open) indicate specimens that were not used for averaging. Triangles show the averaged direction using the results from specimens, except

for those marked by gray circles. Dotted ellipses show the 95% confidence areas.

Following the geocentric axial dipole hypothesis, the inclination at each latitude of Earth's surface can be calculated as follows (Butler, 1992):

$$I = \arctan(2\tan\lambda), \tag{4-1}$$

where I represents inclination and λ is the latitude of the drilling site. Substituting the latitude of the drilling site into (4-1), the calculated inclination is ~52°. Although it is seemingly possible to assess the quality of the reorientation based on this theoretical value, the actual inclination value has been reported to potentially differ substantially from theory owing to the consolidation or rotation of the formation (Butler, 1992). An evaluation of the data quality is therefore difficult using only this value.

4.4.3 Assessment of drilling influence

The most unique feature of the reorientation method proposed in this study is that it can statistically assess the influence of secondary NRM caused by drilling. In this section, we show the results of three samples (Core-1, Core-6, and Core-4) selected from each of the three ranks (Rank A, Rank B and Rank C) defined in section 2.3 and discuss the influence of drilling on the reorientation results.

Fig. 4-9 - Fig. 4-11 shows the Zijderveld diagrams of each specimen from the three core samples. Numbers 1–9 in the figure correspond to the numbers of specimens in Fig. 4-4. Fig. 4-12 shows equal area projections of the primary components of the normalized NRM vectors for each specimen. In the following, each rank is detailed based on the representative samples for the three ranks.

Rank A

Fig. 4-9 and Fig. 4-12 (a) show the results of Core-1, which is rank A. The results show no significant difference between the specimen in the center (specimen 1) and the others. We consider that this type of sample was not affected by drilling and reorientation was

accomplished. However, Core-15, which is also rank A, has an inclination of ~80° (Table 4-1), which indicates a vertical downward NRM and requires further consideration with regards to the influence of drilling.

Rank B

Fig. 4-10 and Fig. 4-12 (b) show the results of Core-6, which is rank B. α_{95} of Core-6 is 13.7°. For this type of result, the primary NRM component of specimen 1 was able to be extracted. However, specimens cut from the periphery (4, 5, 6) were affected by drilling and have secondary NRMs with inclinations of ~90°. It is therefore difficult to extract the primary NRM component from these specimens.

Rank C

Fig. 4-11 and Fig. 4-12 (c) show the results of Core-4, which is rank C. For this type of sample, almost all the specimens, including the central one, were affected by ferromagnetic materials (such as steel pipes) while drilling, and the primary NRM itself was also disturbed. There are no specimens from which the linear component decays to the origin on a Zijderveld diagram can be extracted, and the method proposed in this chapter cannot be applied.

Three different results can be obtained from the same drilling owing to the different degrees of magnetization of the drilling bit and coercive forces of the sample itself.

4.5 Summary

We applied a reorientation method using the NRM of rock to hemipelagic sedimentary soft rocks from the Nankai Trough and discuss the magnetic influence of drilling on the reorientation results. The primary NRM recorded in the central specimen must be extracted to reorientate a core sample. Because rocks can acquire secondary NRM after formation, secondary NRM must be demagnetized. When applying the reorientation method, the average calculation is the subject of a future study. The method of sample

preparation and data quality assessment proposed here offers important guidelines, especially for valuable core samples such as those retrieved from the deep drilling of the IODP.

In the case where other core orientation methods, such as pattern matching, are available, the reliability of the reorientation can be improved by using this method complementarily. This method is expected to contribute to the improvement of the reliability of stress measurement results.

References

Butler, R. F. (1992). *Paleomagnetism: magnetic domains to geologic terranes*. *Paleomagnetism: magnetic domains to geologic terranes*. Boston: Blackwell Scientific Publications. https://doi.org/10.5860/choice.29-5708

Byrne, T. B., Lin, W., Tsutsumi, A., Yamamoto, Y., Lewis, J. C., Kanagawa, K., et al. (2009). Anelastic strain recovery reveals extension across SW Japan subduction zone. *Geophysical Research Letters*, *36*(23), 1–6. https://doi.org/10.1029/2009GL040749

Heuer, V. B., Inagaki, F., Morono, Y., Kubo, Y., Maeda, L., Bowden, S., et al. (2017). Expedition 370 summary, *370*. https://doi.org/10.14379/iodp.proc.370.101.2017

Jin, C., & Liu, Q. (2010). Reliability of the natural remanent magnetization recorded in Chinese loess. *Journal of Geophysical Research*, *115*(B4), 1–15. https://doi.org/10.1029/2009jb006703

Nagano, Y., Lin, W., & Yamamoto, K. (2014). In-situ stress analysis using the anelastic strain recovery (ASR) method at the first offshore gas production test site in the eastern Nankai Trough, Japan. *Marine and Petroleum Geology*, *66*, 418–424. https://doi.org/10.1016/j.marpetgeo.2015.02.027

Nelson, R. A., Lenox, L. C., & Ward Jr, B. J. (1987). Oriented core: its use, error, and uncertainty. *American Association of Petroleum Geologists Bulletin*, *71*(4).

Shigematsu, N., Otsubo, M., Fujimoto, K., & Tanaka, N. (2014). Orienting drill core using borehole-wall image correlation analysis. *Journal of Structural Geology*, *67*(PB), 293–299. https://doi.org/https://doi.org/10.1016/j.jsg.2014.01.016

Tamaki, M., Suzuki, K., & Fujii, T. (2015). Paleocurrent analysis of Pleistocene turbidite sediments in the forearc basin inferred from anisotropy of magnetic susceptibility and paleomagnetic data at the gas hydrate production test site in the eastern Nankai Trough. *Marine and Petroleum Geology*, *66*, 404–417. https://doi.org/https://doi.org/10.1016/j.marpetgeo.2015.02.030

Yamamoto, Y., Lin, W., Oda, H., Byrne, T., & Yamamoto, Y. (2013). Stress states at the subduction input site, Nankai Subduction Zone, using anelastic strain recovery

(ASR) data in the basement basalt and overlying sediments. *Tectonophysics*, *600*, 91–98. https://doi.org/10.1016/j.tecto.2013.01.028

Chapter 5

A Novel analyzing procedure of ASR Method: Theory

5.1 Introduction

The in-situ stress state in the earth's crust, which is a subject of rock mechanics, is crucial information in geosciences, such as structural geology and earth resource engineering (Stein, 1999; Zoback, 2007). A variety of methods have been proposed to measure crustal stress, such as the inversion of earthquake focal mechanisms, analysis of borehole breakout or drilling induced tensile fracture (DITF), hydraulic fracturing, and core-based methods (Amadei & Stephansson, 1997).

One problem with stress measurements is that it is difficult to evaluate the uncertainty of the measurement results. Because it is generally difficult to perform stress measurements, multiple measurements at the same site and depth are not readily available. One possible solution is uncertainty quantification (UQ), which has been actively discussed in recent years within various fields of earth science (Scheidt et al., 2018). Bayesian statistical modeling (BSM), a UQ method, enables us to evaluate uncertainty even with limited measurement data by utilizing information that is known before the measurement. The effectiveness of this method has been confirmed in the fields of earth and planetary sciences and rock mechanics for which there is generally a paucity of measurement data (Aladejare & Wang, 2019; Atkins et al., 2016; Contreras et al., 2018;

Feng & Jimenez, 2014). However, no previous studies have investigated the application of UQ to stress measurements. In this study, I develop a novel analytic procedure for the anelastic strain recovery (ASR) for UQ using BSM. The ASR method (K Matsuki & Takeuchi, 1993) is a core-based three-dimensional stress measurement method that can be applied to deep drilling (up to approximately 10 km depth) and has been used in recent onshore and offshore drilling projects (Byrne et al., 2009; Lin et al., 2007; Sun et al., 2017; Yamamoto et al., 2013).

This research comprises two stages. In the first stage, a novel analysis procedure for the ASR method was proposed and the characteristics were examined by applying the procedure to simulated (artificial) data. In the second stage, the novel procedure was applied to appropriate real ASR data. I report on the first stage of this study in this chapter. The second stage is reported in the next chapter.

5.2 Bayesian statistical modeling

In this section, I review the general theory of BSM. The novel ASR analytic procedure is described in detail in the next section. BSM (Watanabe, 2018) is a parameter estimation method that represents the inference results by a probability distribution called posterior distribution

$$\Pi(\mathbf{w}|D) = \frac{L(D|\mathbf{w})\phi(\mathbf{w})}{Z(D)}, \tag{5-1}$$

where $\mathbf{w} = \left(w_1, w_2, \cdots, w_q\right)^{\mathrm{T}}$ is a vector of q parameters to be estimated, D is the observed data set and ϕ is a probability density function called the prior distribution, which needs to be determined for each parameter. Z is a normalizing constant defined by:

$$Z(D) = \int_{\Omega} L(D|\boldsymbol{\tau})\phi(\boldsymbol{\tau})\mathrm{d}\boldsymbol{\tau}. \tag{5-2}$$

$\Omega \subset \mathbb{R}^q$ is the set of all possible values of parameters ($\mathbb{R}$ is the set of real numbers), L is called a likelihood function, which shows the probability of obtaining data D given a set of values of parameters. It takes various forms depending on the problem to be applied. The likelihood function used in this study is explained in the next section. Although there have been various discussions on how to determine the prior distribution (Watanabe, 2012), in this study, I set the distribution based on the information obtained in the actual application. The details are described in Section 5.3.

Because the posterior distribution Π is a joint probability distribution for all parameters, it is necessary to calculate the marginal posterior distribution (MPD)

$$\pi_i(w_i|D) = \int \Pi(\mathbf{w}|D)\mathrm{d}w_1 \cdots \mathrm{d}w_{i-1}\mathrm{d}w_{i+1} \cdots \mathrm{d}w_q \tag{5-3}$$

to obtain the results for each parameter. However, it is generally difficult to obtain posterior distribution and MPDs analytically; therefore, they are often simulated by Markov Chain Monte Carlo (MCMC) method (Hoffman & Gelman, 2014). There are many excellent texts on MCMC (Bishop, 2006; Ripley, 1987), so I do not describe the details and provide only a brief overview.

In MCMC, a Markov process with a posterior distribution is generated on a computer as the stationary distribution, and the MPDs are obtained by sampling for each parameter from the Markov process. The most important point is whether the obtained sample sequences of each parameter converge to the true MPDs. There have been various methods for assessing convergence, and in this study, I adopted the widely used method of Gelman & Rubin (1992). In this method, the convergence decision is made according to the values

$$\hat{R} = \sqrt{\frac{N-1}{N} + \frac{1}{N}\frac{B}{W}} \tag{5-4}$$

computed for each parameter from the multiple sample sequences with different initial values, where N is the number of steps in the sample sequence (number of samples included), B is the variance between sample sequences, and W is the variance within a sample sequence (for the exact definition, see Brooks & Gelman (1998) and Gelman & Rubin, (1992)). In this method of determining convergence, I conclude that convergence has been achieved when the variation between multiple sample sequences starting from different initial values is less than the variation within each sample sequence. Gelman et al. (2013) proposed a criterion in which convergence is judged when there are three or more sample sequences and $\hat{R}$<1.1 for all parameters, and the same criterion was used in this study. In this study, the MCMC was executed using the program coded in Stan programing language (Carpenter et al., 2017).

The advantages of BSM are that it provides a flexible approach for using information that is known prior to the measurement in the form of prior distributions and quantitatively determines uncertainty as a probability distribution.

5.3 Novel ASR method analytic procedure

In this section, I present a novel analytic procedure of the ASR method based on BSM (hereinafter referred to as the "novel method"). In the novel method, the in-situ stress is estimated by applying a probabilistic model, which consists of a likelihood function and a prior distribution, to the anelastic normal strain recovery data. The results of the estimation are used as the results of the in-situ stress measurement. In the following sections, I provide detailed explanations on data, likelihood functions, and prior distributions used.

The ASR constitutive equation used in this research is

$$\varepsilon(t,\mathbf{n}) = \left(\sigma_{ij}n_i n_j - \sigma_{\mathrm{m}}\right)J_{\mathrm{S}}(t) + (\sigma_{\mathrm{m}} - p_0)J_{\mathrm{V}}(t), \qquad (5\text{-}5)$$

the same equation as in Chapter 3.

The data used in the novel method are the same as those used in the conventional method (Fig. 5-1), which is the time series data $D = \{(t_i, \boldsymbol{\varepsilon}_i) | i = 1 \sim m\}$ of anelastic normal strain recovery measured with strain gauges. t_i is the time elapsed from the start of the measurement, $\boldsymbol{\varepsilon}_i = \left(\varepsilon_i^1, \varepsilon_i^2, \cdots, \varepsilon_i^d\right)^{\mathrm{T}}$ is a vector of the anelastic normal strain recovery data for d directions (up to nine directions shown in Fig. 5-1 (b)), and m is the number of sampling points of the anelastic normal strain recovery data at time t_i. For details of the measurement procedure and system, see Lin et al. (2007).

In this study, I used simulated data rather than real data to examine the novel method. The details of the simulated data are shown in Section 5.4.

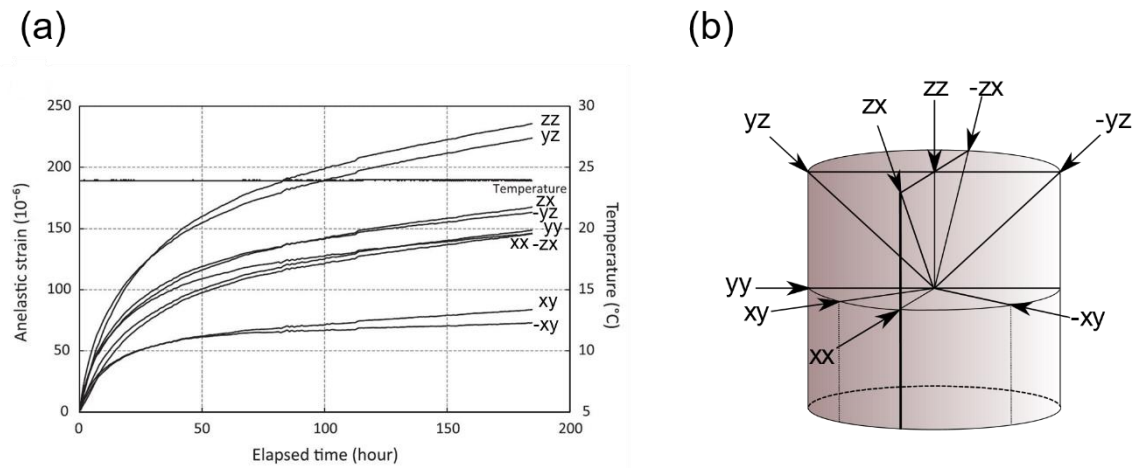

Fig. 5-1 (a) Real anelastic normal strain recovery data measured on a sedimentary rock core collected in the eastern Nankai Trough (Modified from Nagano et al. 2014). The labels (*xx*, *xy*, and so on) indicate the nine directions in which anelastic normal strains were measured and correspond to those shown in (b). The temperature of the measured rock core is also shown. (b) Nine directions in which anelastic normal strains are measured with strain gauges. The directions of ±*xy*, ±*yz*, and ±*zx* are tilted at 45 degrees with respect to those of *xx*, *yy*, and *zz*.

The likelihood function in this study consists of two components: (i) the constitutive equation (5-5) relating the anelastic normal strain recovery to the in-situ

stress tensor, and (ii) the probability density function to which the measurement error of anelastic normal strain recovery is subjected. In the conventional method, stress is calculated without assuming specific functional forms of ASR compliances in (5-5), but the novel method uses specific functional forms of these to calculate the in-situ stress. In this study, I use

$$J_{\mathrm{S}}(t) = \frac{1}{2G}\left(1 - \exp\left(-\frac{t}{\tau_{\mathrm{s}}}\right)\right)$$
$$J_{\mathrm{V}}(t) = \frac{1}{3K}\left(1 - \exp\left(-\frac{t}{\tau_{\mathrm{v}}}\right)\right), \tag{5-6}$$

which are obtained by assuming a three-element model consisting of two springs and one dashpot (Flügge, 1975). G and K are the shear modulus and bulk modulus of the rock comprising the measured rock core, τ_{s} and τ_{v} are the retardation times for the shear and volumetric deformation of the rocks, defined by

$$\tau_{\mathrm{S}} = \frac{\eta_{\mathrm{S}}}{2G}$$
$$\tau_{\mathrm{V}} = \frac{\eta_{\mathrm{V}}}{3K}, \tag{5-7}$$

where η_{S} and η_{V} represent the shear and volumetric viscosities of the rock, respectively. The retardation time is the time required for strain recovery to reach 63.2% of the total ASR. The ASR compliances used in this study have not yet been formulated to simulate dependence on the mean normal stress; therefore, the modification of ASR compliances (5-6) requires further study. The probability density function that the measurement error of the anelastic normal strain recovery obeys is considered to be a normal distribution. These conditions lead to a likelihood function

$$L(D|\mathbf{w}) = \prod_{i=1}^{m} \frac{1}{\sqrt{(2\pi)^d |\boldsymbol{\Sigma}|}} \times \exp\left[-\frac{1}{2}\left(\boldsymbol{\varepsilon}_i - \bar{\boldsymbol{\varepsilon}}(t_i)\right)^{\mathrm{T}} \boldsymbol{\Sigma}^{-1} \left(\boldsymbol{\varepsilon}_i - \bar{\boldsymbol{\varepsilon}}(t_i)\right)\right], \tag{5-8}$$

where $\boldsymbol{\varepsilon}_i$ is a vector with the measured data as elements, $\bar{\boldsymbol{\varepsilon}}$ is a vector with the theoretical value of the anelastic normal strain recovery calculated from (5-5), and $\boldsymbol{\Sigma}$ is a covariance matrix of multivariate normal distribution to which the measurement error of the anelastic normal strain recovery obeys. In this study, the measurement errors of the anelastic normal strain recovery were assumed to be constant regardless of the direction of measurement, and the measurement in each direction was independent. Therefore, $\boldsymbol{\Sigma} = s\mathbf{I}$ was used, where s is a scalar representing the value of the variance that is common in all measurement directions, and $\mathbf{I}$ is the d-dimensional unit matrix. The parameter to be estimated is $\mathbf{w} = (\sigma_{11}, \sigma_{22}, \sigma_{33}, \sigma_{12}, \sigma_{13}, \sigma_{23}, p_0, G, K, \tau_{\mathrm{S}}, \tau_{\mathrm{V}}, s)^{\mathrm{T}}$.

There are several methods for determining the prior distribution as mentioned above. In this study, I propose that the prior distributions are determined based on the information obtained separately from the stress measurement (prior information). In the following, I explain three sets of prior information and prior distributions derived from prior information.

Prior information 1

The ranges of realistic values of each parameter were used as a priori information. The ranges of stress and pore pressure in the depth interval where the ASR method can be applied is from 0 MPa to 100 MPa. The possible ranges of the elastic moduli G and K are from 0 GPa to 100 GPa, and the possible ranges of retardation times τ_{S} and τ_{V} are from 0 h to 100 h. s, which represents the measurement error, is >0. From the theory of elasticity, I can conclude that $K > G$. Based on this prior information, I define prior distributions for each parameter. These are summarized in Table 5-1.

Prior information 2

The vertical element of the stress tensor at the measurement depth is close to the overburden stress calculated from the average wet density of rocks that exist above the measurement depth, and the pore pressure at the same depth is expected to be close to the hydrostatic pressure calculated from the groundwater level. This prior information can be expressed as probability density functions of the vertical element of the stress tensor, and the pore pressure with the mean is the overburden pressure and hydrostatic pressure, respectively. In this study, the aforementioned prior information is expressed by setting the prior distribution of σ_{33}, which is the vertical element in the coordinate system used in this study, as a normal distribution with a mean of $\rho_{\mathrm{r}}gh$ and a standard deviation of 5 MPa, and by setting the prior distribution of p_0 as the normal distribution with the mean $\rho_{\mathrm{w}}gh_{\mathrm{w}}$ and standard deviation of 5 MPa. Note that the values of $\rho_{\mathrm{r}}gh$ and $\rho_{\mathrm{w}}gh_{\mathrm{w}}$ are the true values of σ_{33} and p_0 (Value in Table 5-1), which are described in the next section.

Prior information 3

In some cases, measurements of the elastic moduli G and K can be obtained from experiments. I considered using these measurements as prior information. In this study, I represent this prior information by using G and K as constants rather than parameters to be estimated. In this study, the true values of G and K in Table 5-1, which are described in the next section, are used as measurements of the moduli.

The information available varies from case to case, and many combinations of information are available for actual applications of stress measurement. Therefore, this chapter focuses on the following two patterns of case studies (combinations of prior information) to estimate the stress values. The first case is that in which both prior information 1 and 2 are available, which I call Case-1. The second case is that in which all prior information (1, 2, and 3) is available, which I call Case-2. The prior distributions of each parameter are shown in Table 5-1 for Case-1 and Case-2, respectively, where U[a, b] denotes a uniform distribution from a to b, and N[c, d] denotes a normal distribution with mean c and standard deviation d, respectively.

Summary of the novel method

The procedure of the stress measurement in the novel method is summarized as follows: (i) the anelastic normal strain recovery of a rock core is measured in the same manner as in the conventional method, (ii) (5-8) and the prior distributions shown in Table 5-1 are applied to the measured anelastic normal strain recovery data, and then sampling by MCMC to obtain the MPDs of each parameter, and (iii) the obtained MPDs are regarded as the measurement results of in-situ stress and other parameters. Fig. 5-2 shows the flow.

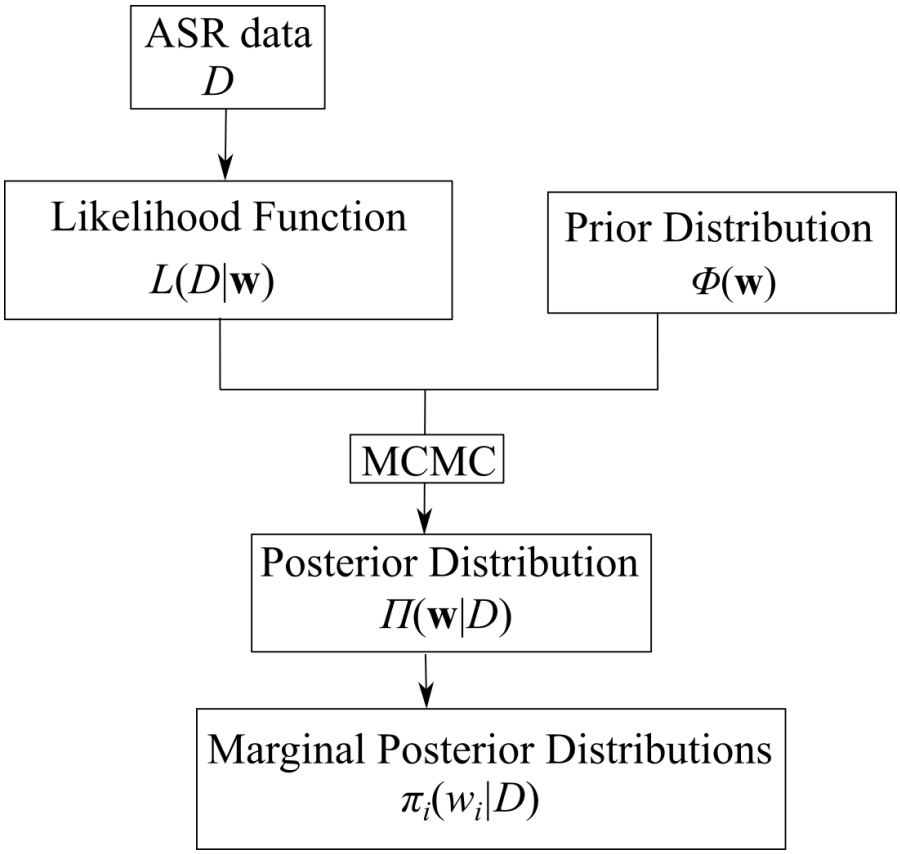

Fig. 5-2 Flow chart showing the concept of proposed analytic procedure.

5.4 Simulated ASR data

In the first stage of this study, the novel method was examined using simulated data of ASR generated from (5-5). The values of the parameters used to create the simulated data

are listed in Table 5-1. The magnitudes of the principal stresses calculated using stress tensor shown in Table 5-1 are σ_1 =39 MPa (the maximum principal stress), σ_2 =34 MPa (the intermediate principal stress), and σ_3 =29 MPa (the minimum principal stress), respectively, and the direction of the intermediate principal stress is set to be subparallel to the vertical direction. The stresses and pore pressures were determined on the basis of the values around 1.5 km depth, and the coefficients of viscoelasticity of the rocks were determined on the basis of several references (Kobayashi & Ito, 1982; Kumagai et al., 1986; Koji Matsuki, 2008), assuming that the rocks are granite. The true values of the parameters estimated in this study are shown in Table 5-1. To the simulated data, a random number following a normal distribution (mean 0, standard deviation 5×10^{-6}) was added as a measurement error. The simulated data using the values in Table 5-1 are shown in Fig. 5-3. I used 48 hours of data from the start of the measurement for estimation to limit computational costs. The sampling interval was set to 10 min, which is the same as the actual measurement, and the number of sampling points was 288 in each direction.

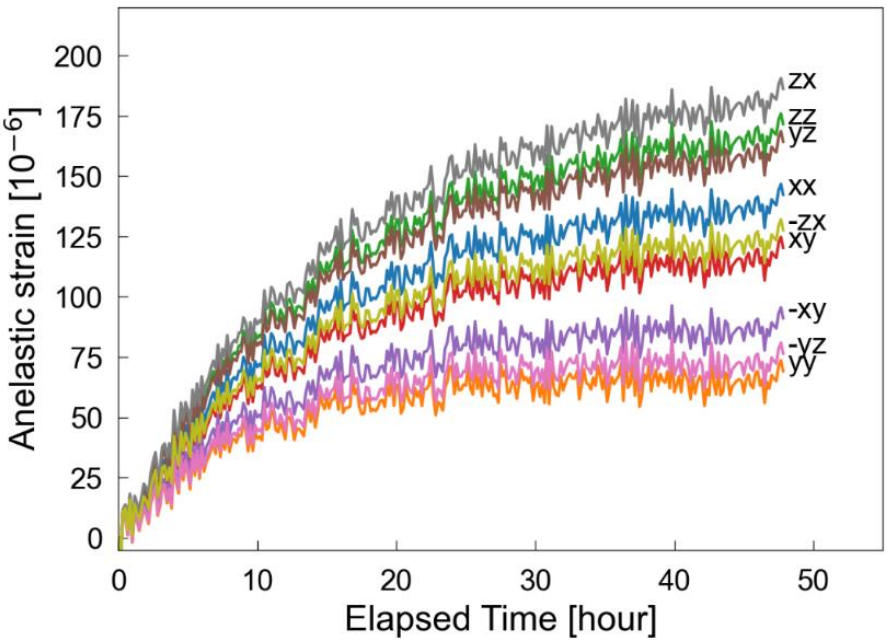

Fig. 5-3 Simulated ASR data developed by using (5-5) and values shown in Table 5-1. The labels (*xx*, *xy*, and so on) correspond to those shown in Fig. 5-1 (b).

Table 5-1 Parameters, values for simulated data, and prior distributions for each case. U[a, b] denotes a uniform distribution from a to b, and N[c, d] denotes a normal distribution with mean c and standard deviation d, respectively.

Parameter		Symbol	Value	Prior distribution	
				Case-1	Case-2
Stress tensor [MPa]		σ_{11}	35	U[0, 100]	U[0, 100]
		σ_{22}	30	U[0, 100]	U[0, 100]
		σ_{33}	37	N[37, 5]	N[37, 5]
		σ_{12}	1	U[0, 100]	U[0, 100]
		σ_{13}	2	U[0, 100]	U[0, 100]
		σ_{23}	3	U[0, 100]	U[0, 100]
Pore pressure [MPa]		p_0	15	N[15, 5]	N[15, 5]
Shear modulus [GPa]		G	30	U[0, K]	30
Bulk modulus [GPa]		K	50	U[0, 100]	50
Retardation time [hour]	Volumetric	τ_V	13.33	U[0, 100]	U[0, 100]
	Shear	τ_S	22.68	U[0, 100]	U[0, 100]
Variance [10^{-12}]		s		U[0, 100]	U[0, 100]

5.5 Results of novel procedure

The MCMC in this study was performed using a supercomputer owned by Kyoto University, and a single simulation took approximately two hours. Fig. 5-4 and Fig. 5-5 show the inference results of σ_{11} and σ_{12} in Case-1. Fig. 5-4 (a) and Fig. 5-5 (a) show the three sample sequences, programmed to start from different initial values, obtained by MCMC, and Fig. 5-4 (b) and Fig. 5-5 (b) show the resulting MPD. The initial values are the samples selected using a random number (independent of the probability model in use), and the number of steps is counted with the initial value as the first. Each sample sequence consisted of 1500 samples, giving a total of 4500 samples for each parameter. In Fig. 5-4 (a) and Fig. 5-5 (a), it can be seen that the sampling depends on the initial values up to approximately 100 steps. In general, samples up to several hundred steps are not used in the analysis because they are dependent on the initial values. This part of the sample is called the warm-up. In this study, I decided to define the warm-up as the samples up to 500 steps and not to use them for further analysis. Therefore, the following analysis was performed with 3000 samples for each parameter. The estimation results for Case-1 and Case-2 are shown in Table 5-2. The table lists the mean (Mean), standard deviation (SD), left (2.5%) and right (97.5%) end of credible interval and $\hat{R}$ values calculated using 3000 samples, excluding the warm-up of each parameter.

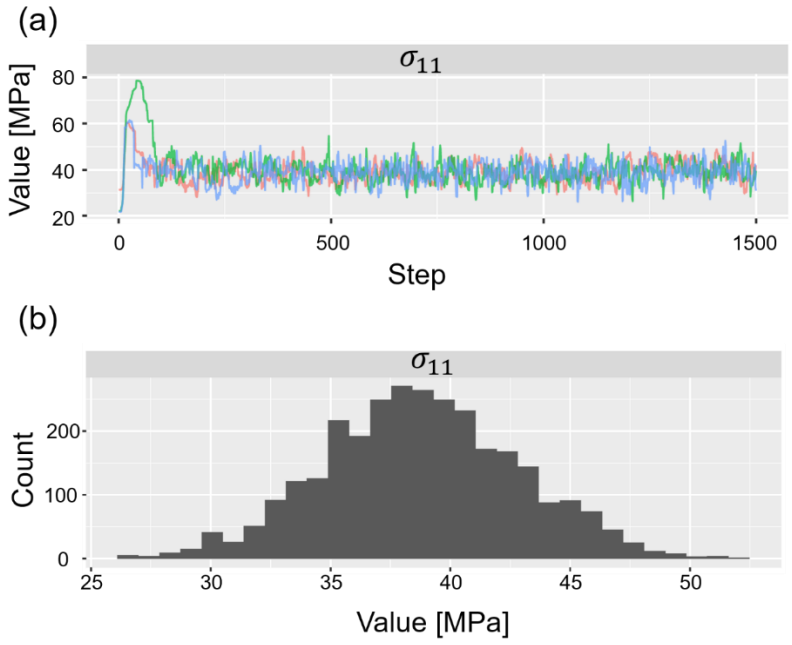

Fig. 5-4 Results of inference for σ_{11} in Case-1. (a) Three Markov chains with different initial values. Each chain consists of 1500 samples. (b) Marginal posterior distribution obtained from three chains in (a).

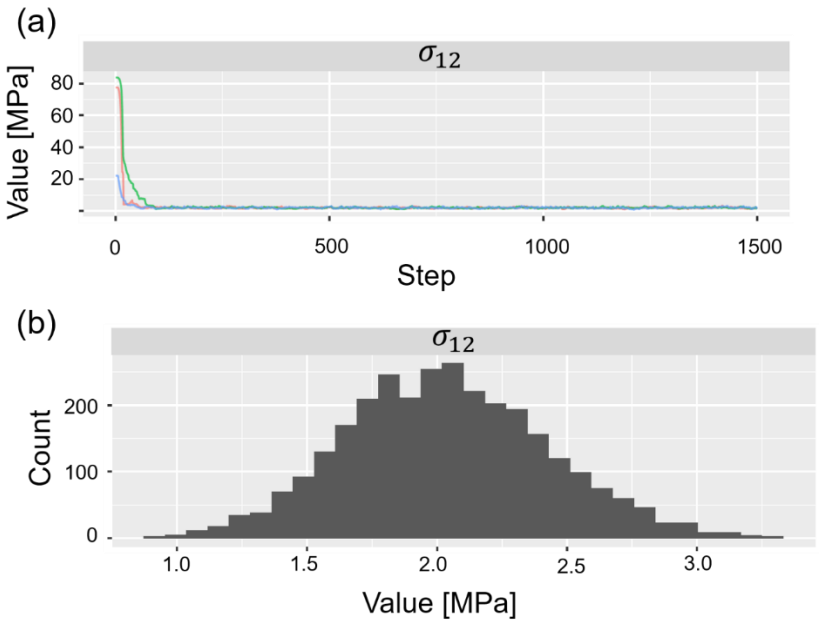

Fig. 5-5 Results of inference for σ_{12} in Case-1. (a) Three Markov chains with different initial values. Each chain consists of 1500 samples. (b) Marginal posterior distribution obtained from three chains in (a).

In this study, I discussed the estimation results from two points of view: (i) the uncertainty of the estimation results and (ii) the difference between the estimated value and the true value. The standard deviation of the MPD (SD in Table 5-2) is used as the measure of (i), and the difference between the mean and true values (the difference between the true value and Mean in Table 5-2) is used as the measure of (ii). In this chapter, I call the former uncertainty and the latter deviance, and I evaluate the estimation in which both uncertainty and deviance are small as good estimations.

In Case-1, the elastic moduli are assumed to be unmeasured and are parameters for estimation. The estimation results of the stress tensor (Table 5-2) show that the uncertainty of the non-diagonal elements (σ_{12}, σ_{13}, and σ_{23}) are smaller than those of the diagonal elements (σ_{11}, σ_{22}, and σ_{33}), while there is no significant difference in deviance between the diagonal and non-diagonal elements. The results of the estimates of the shear and bulk moduli show that both uncertainty and deviance are greater than the other parameters. Conversely, the retardation times, which represent the viscoelastic properties, are estimated to be better than other parameters.

I next examined the results of Case-2, where the elastic moduli are no longer parameters for estimation because it is assumed to be given in Case-2. The results of the stress tensor estimation show that the uncertainty of the non-diagonal elements is significantly less than that of the diagonal elements. Furthermore, unlike Case-1, the non-diagonal elements of the deviance are smaller, indicating that I can estimate the true value more accurately.

Comparing the two cases, I conclude that the deviances are smaller in Case-2 than in Case-1 for all parameters. In other words, the probability model in this study provides a more accurate estimate of the true value by providing the elastic moduli as prior information. This is an intuitively valid result. In contrast, uncertainty in the non-diagonal element of the stress tensor decreases from Case-1 to Case-2, yet the decrease is hardly observed in the diagonal element and the pore pressure compared to the non-diagonal element. In the estimation results of retardation times, there is almost no difference between Case-1 and Case-2, and both are considered to exhibit good estimation.

These results indicate that the quality of the estimation differs from one

parameter to another. A possible reason for the differences between parameters is the difference in the roles of the parameters in (5-5), which is the basis of the estimation. In other words, the differences in the importance of each parameter in (5-5) are supposed to result in different estimation results. Sensitivity analysis provides a framework to quantitatively evaluate the importance of parameters. In the next section, the differences in each parameter are discussed based on the sensitivity analysis.

Table 5-2 Results of inference. True values are the same as those shown in Table 5-1. Mean and SD are the mean values and standard deviations calculated using the three chains excluding the warm-up samples.

Symbol	Unit	True value	Case-1						Case-2					
			Mean	SD	2.5%	97.5%	Deviance	Rhat	Mean	SD	2.5%	97.5%	Deviance	Rhat
σ_{11}	[MPa]	35	38.77	4.07	30.54	46.66	3.77	1.01	35.07	3.42	28.24	41.61	0.07	1.00
σ_{22}		30	28.60	3.93	21.55	36.87	1.40	1.02	30.07	3.42	23.19	36.58	0.07	1.00
σ_{33}		37	42.84	4.37	34.18	51.41	5.84	1.01	37.07	3.42	30.26	43.58	0.07	1.00
σ_{12}		1	2.03	0.39	1.29	2.84	1.03	1.02	1.00	0.02	0.96	1.04	0.00	1.00
σ_{13}		2	4.07	0.78	2.59	5.65	2.07	1.02	2.00	0.03	1.95	2.06	0.00	1.00
σ_{23}		3	6.10	1.17	3.85	8.49	3.10	1.02	3.00	0.04	2.93	3.08	0.00	1.00
p_0	[MPa]	15	9.28	3.88	1.94	16.68	5.72	1.02	15.14	3.42	8.30	21.67	0.14	1.00
G	[GPa]	30	60.95	11.71	53.75	94.38	30.95	1.02						
K		50	72.50	10.50	38.65	85.11	22.50	1.01						
τ_V	[hour]	13.33	13.23	0.07	13.08	13.38	0.10	1.00	13.23	0.08	13.09	13.38	0.10	1.00
τ_S		22.68	22.74	0.54	21.69	23.79	0.06	1.00	22.74	0.53	21.73	23.80	0.06	1.00
s	[10^{-12}]		22.53	0.62	21.36	23.78		1.00	22.48	0.60	21.30	23.68		1.00

5.6 Sensitivity analysis

First, an overview of the sensitivity analysis is briefly described. A detailed explanation is presented elsewhere (e.g., Saltelli et al. (2008)). Given the function $y = f(\mathbf{x})$, where $\mathbf{x} = \left(x_1, x_2 \cdots, x_q\right)^{\mathrm{T}}$ is a parameter of this model. Sensitivity analysis provides a framework for quantitatively assessing the contribution of $\mathbf{x}$ to the variation in y caused by variation in the parameter $\mathbf{x}$. It has been pointed out that when performing parameter estimation, parameters with higher sensitivity can be estimated better than those with lower sensitivity (Farchmin et al., 2019). In this section, I present an analysis using the Sobol' method (Sobol', 1990), a widely used sensitivity analysis in which the contribution of the variance of x_i to the variance of y is used as a sensitivity index. In this study, I use the Total Sensitivity Indices S_{T} (Homma & Saltelli, 1996), which are used in Sobol' method and considers both cases where there is interaction between the parameters and where there is not. In particular, I conducted a sensitivity analysis of Case-2, which shows a significant difference in uncertainty. Fig. 5-6 shows the S_{T} of each parameter calculated using (5-5). Fig. 5-6 (a) and (b) show the results when $\mathbf{n} = (1, 0, 0)^{\mathrm{T}}$ is substituted in (5-5) (direction xx), and $\mathbf{n} = (\cos 45°, \sin 45°, 0)^{\mathrm{T}}$ is substituted in (5-5) (direction xy), respectively. The horizontal axis is the time elapsed since the start of measurement, and the figures show the value of sensitivity at each time.

For each element of the stress tensor and the pore pressure, the sensitivity of the diagonal element (in this case, σ_{11}) is large in absolute value in the xx direction, but the sensitivity of the pore pressure is relatively large compared to that of σ_{11}. Conversely, for the data in the xy direction, the sensitivity of the non-diagonal element (in this case, σ_{12}) is relatively greater than the sensitivity of the other parameters. In this xx direction, the sensitivity of parameters other than the diagonal element is also relatively large, which indicates that the uncertainty is greater than that of the non-diagonal element. Because the retardation time represents the time constant of the strain recovery curve, it can be expected that the sensitivity increases in the early part of the measurement, where the curvature is large. In fact, the sensitivity of τ_{S} increases at the beginning of the measurement. However, it can be observed that the sensitivity of τ_{V} is zero most of the

time. This suggests that low sensitivity is not necessarily associated with high uncertainty in the estimation by BSM. The different role of parameters in (5-5) is a possible reason why sensitivity and uncertainty do not necessarily correspond to each other. The retardation times τ_S and τ_V represent the time constants of the strain recovery curve and are responsible for determining the curvature. On the other hand, the stress tensor and pore pressure are coefficients of the curve and are responsible for determining the final amount of recovery. The relationship between BSM and sensitivity analysis has not been fully elucidated. Further researches are needed in this regard.

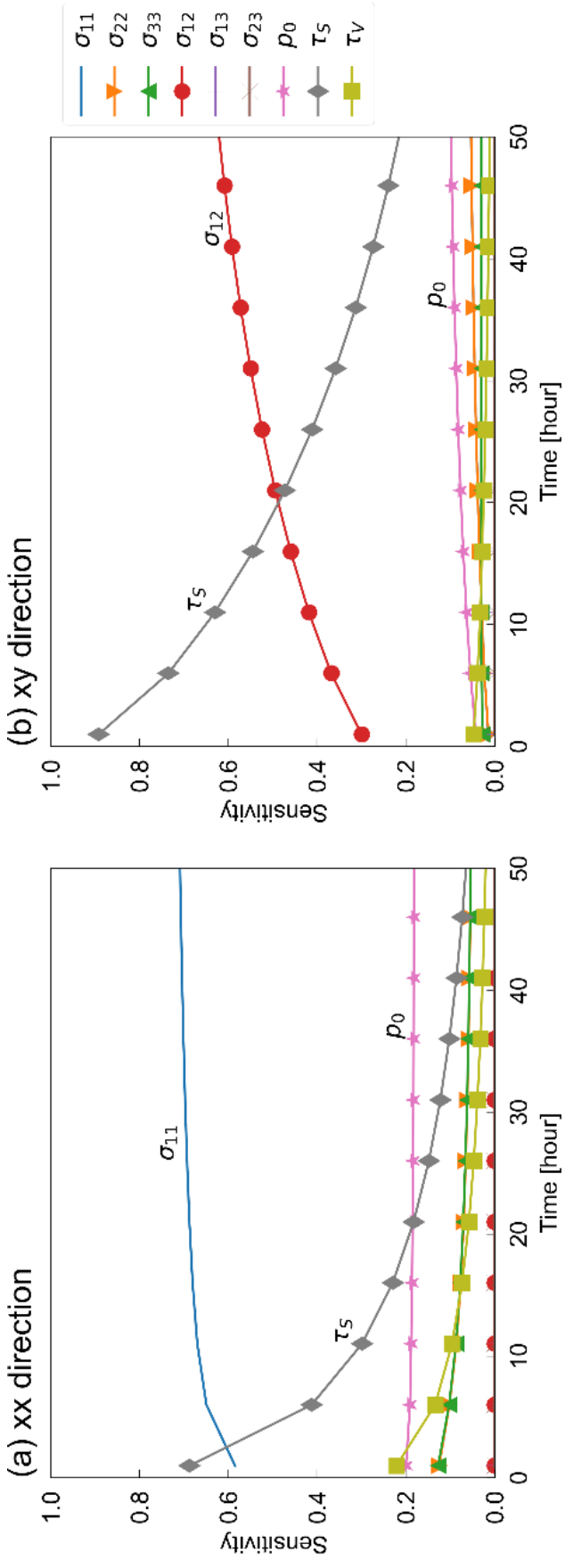

Fig. 5-6 Total sensitivity indices for each parameter in Case-2. (a) Sensitivities calculated using anelastic normal strain recovery in the *xx* direction in Fig. 5-1(b). (b)Sensitivities calculated using anelastic normal strain recovery in the *xy* direction in Fig. 5-1 (b).

5.7 Summary

In this study, I proposed a novel ASR analytic procedure that enables us to quantify the uncertainty of the measurement results and examined it using simulated data. I demonstrated that BSM can be used to quantitatively evaluate measurement error as the standard deviation of MPD. The results obtained by the novel method revealed that the uncertainty of the estimation results varies with each parameter. In particular, the uncertainty of the non-diagonal elements of the stress tensor (σ_{12}, σ_{13}, and σ_{23}) was smaller than that of the other parameters in the estimation (Case-2) with the known elastic moduli. Sensitivity analysis revealed that this difference is partially impacted by parameter sensitivity. The results suggest that there is not necessarily a correspondence between the results of BSM estimates and sensitivity analysis. Further studies on the relationship between sensitivity and estimation uncertainty are required.

In this method, the stress tensor obtained by other methods can be used as an input to obtain the pore pressure more accurately and flexibly. This is especially effective when the pore pressure is not released instantaneously but gradually. Moreover, anisotropy can be incorporated into the compliance model, which makes it possible to perform measurements based on more accurate assumptions for rock samples such as sedimentary rocks where orthotropic anisotropy is prevalent.

References

Aladejare, A. E., & Wang, Y. (2019). Probabilistic characterization of Hoek–Brown constant m_i of rock using Hoek's guideline chart, regression model and uniaxial compression test. *Geotechnical and Geological Engineering*, *37*(6), 5045–5060. https://doi.org/10.1007/s10706-019-00961-7

Amadei, B., & Stephansson, O. (1997). Rock stress and its measurement. In *Springer Science & Business Media*. https://doi.org/10.1007/978-94-011-5346-1

Atkins, S., Valentine, A. P., Tackley, P. J., & Trampert, J. (2016). Using pattern recognition to infer parameters governing mantle convection. *Physics of the Earth and Planetary Interiors*, *257*, 171–186. https://doi.org/10.1016/j.pepi.2016.05.016

Bishop, C. M. (2006). Pattern recoginiton and machine learning. *Springer-Verlag*, 738.

Brooks, S. P., & Gelman, A. (1998). General Methods for Monitoring Convergence of Iterative Simulations. *Journal of Computational and Graphical Statistics*, *7*(4), 434–455. https://doi.org/10.1080/10618600.1998.10474787

Byrne, T. B., Lin, W., Tsutsumi, A., Yamamoto, Y., Lewis, J. C., Kanagawa, K., Kitamura, Y., Yamaguchi, A., & Kimura, G. (2009). Anelastic strain recovery reveals extension across SW Japan subduction zone. *Geophysical Research Letters*, *36*(23), 1–6. https://doi.org/10.1029/2009GL040749

Carpenter, B., Gelman, A., Hoffman, D. M., Lee, D., Goodrich, B., Betancourt, M., Brubaker, M., Guo, J., Li, P., & Riddell, A. (2017). Stan : A probabilistic programming language. *Journal of Statistical Software*, *76*(1). https://doi.org/10.18637/jss.v076.i01

Contreras, L. F., Brown, E. T., & Ruest, M. (2018). Bayesian data analysis to quantify the uncertainty of intact rock strength. *Journal of Rock Mechanics and Geotechnical Engineering*, *10*(1), 11–31. https://doi.org/10.1016/j.jrmge.2017.07.008

Farchmin, N., Hammerschmidt, M., Schneider, P.-I., Wurm, M., Bodermann, B., Bär, M., & Heidenreich, S. (2019). Efficient global sensitivity analysis for silicon line gratings using polynomial chaos. *Proc. SPIE 11057, Modeling Aspects in Optical*

Metrology VII. https://doi.org/10.1117/12.2525978

Feng, X., & Jimenez, R. (2014). Bayesian prediction of elastic modulus of intact rocks using their uniaxial compressive strength. *Engineering Geology*, *173*, 32–40. https://doi.org/10.1016/j.enggeo.2014.02.005

Flügge, W. (1975). Viscoelasticity. *Springer-Verlag*, 203. https://doi.org/10.1007/978-3-662-02276-4

Gelman, A., Carlin, J. B., Stern, H. S., Dunson, D. B., Vehtari, A., & Rubin, D. B. (2013). Bayesian data analysis. *Chapman and Hall/CRC*, 675.

Gelman, A., & Rubin, D. B. (1992). Inference from iterative simulation using multiple sequences. *Statistical Science*, *7*(4), 457–472.

Hoffman, M. D., & Gelman, A. (2014). The No-U-Turn sampler: Adaptively setting path lengths in Hamiltonian Monte Carlo. *Journal of Machine Learning Research*, *15*(1), 1593–1623.

Homma, T., & Saltelli, A. (1996). Importance measures in global sensitivity analysis of nonlinear models. *Reliability Engineering & System Safety*, *52*(1), 1–17. https://doi.org/https://doi.org/10.1016/0951-8320(96)00002-6

Kobayashi, Y., & Ito, H. (1982). Researches on dynamic properties of rock and tectonic problems. *Journal of the Society of Materials Science*, *31*(347), 790–798. https://doi.org/10.2472/jsms.31.790

Kumagai, N., Ito, H., & Sasajima, S. (1986). Long-term creep of rocks. *Journal of the Society of Materials Science*, *35*(392), 484–489. https://doi.org/10.2472/jsms.35.484

Lin, W., Yeh, E. C., Ito, H., Hirono, T., Soh, W., Wang, C. Y., Ma, K. F., Hung, J. H., & Song, S. R. (2007). Preliminary results of stress measurement using drill cores of TCDP Hole-A: An application of anelastic strain recovery method to three-dimensional in-situ stress determination. *Terrestrial, Atmospheric and Oceanic Sciences*, *18*(2), 379–393. https://doi.org/10.3319/TAO.2007.18.2.379(TCDP)

Matsuki, K, & Takeuchi, K. (1993). Three-dimensional in situ stress determination by anelastic strain recovery of a rock core. *International Journal of Rock Mechanics and Mining Sciences & Geomechanics Abstracts*, *30*(7), 1019–1022.

https://doi.org/https://doi.org/10.1016/0148-9062(93)90064-K

Matsuki, Koji. (2008). Anelastic strain recovery compliance of rocks and its application to in situ stress measurement. *International Journal of Rock Mechanics and Mining Sciences*, *45*(6), 952–965. https://doi.org/https://doi.org/10.1016/j.ijrmms.2007.10.005

Nagano, Y., Lin, W., & Yamamoto, K. (2014). In-situ stress analysis using the anelastic strain recovery (ASR) method at the first offshore gas production test site in the eastern Nankai Trough, Japan. *Marine and Petroleum Geology*, *66*, 418–424. https://doi.org/10.1016/j.marpetgeo.2015.02.027

Ripley, B. D. (1987). Stochastic simulation. *John Wiley & Sons*, 238.

Saltelli, A., Ratto, M., Andres, T., Campolongo, F., Cariboni, J., Gatelli, D., Saisana, M., & Tarantola, S. (2008). Global sensitivity analysis: The primer. In *John Wiley & Sons*. John Wiley & Sons.

Scheidt, C., Li, L., & Caers, J. (2018). Quantifying uncertainty in subsurface systems. In *John Wiley & Sons*. John Wiley & Sons, Inc.

Sobol', I. M. (1990). On sensitivity estimation for nonlinear mathematical models. *Matematicheskoe Modelirovanie*, *2*(1), 112–118.

Stein, R. S. (1999). The role of stress transfer in earthquake occurrence. *Nature*, *402*(6762), 605–609. https://doi.org/10.1038/45144

Sun, D., Sone, H., Lin, W., Cui, J., He, B., Lv, H., & Cao, Z. (2017). Stress state measured at ~7 km depth in the Tarim Basin, NW China. *Scientific Reports*, *7*(1), 1–10. https://doi.org/10.1038/s41598-017-04516-9

Watanabe, S. (2012). Theory and method of Bayes statistics. In *Corona Publishing*.

Watanabe, S. (2018). Mathematical theory of Bayesian statistics. In *Chapman and Hall/CRC*. https://doi.org/10.1201/9781315373010

Yamamoto, Y., Lin, W., Oda, H., Byrne, T., & Yamamoto, Y. (2013). Stress states at the subduction input site, Nankai Subduction Zone, using anelastic strain recovery (ASR) data in the basement basalt and overlying sediments. *Tectonophysics*, *600*, 91–98. https://doi.org/10.1016/j.tecto.2013.01.028

Zoback, M. D. (2007). Reservoir geomechanics. In *Cambridge University Press*.

Chapter 6

A Novel Analyzing Procedure of ASR Method: Application

6.1 Introduction

In this chapter, the novel analysis procedure proposed in Chapter 5 is applied to real ASR data. The used ASR data were measured from rock core samples obtained from a borehole near the Nojima Fault, which is the source fault of the 1995 Mw 6.9 Kobe earthquake. Stress measurements by hydraulic fracturing and borehole breakout methods have been carried out at the depth where the samples were taken. In the discussion, I compare the results of the novel ASR method with those of other methods to examine the validity of the present method. In this chapter, the same variable symbols as in Chapter 5 are used.

6.2 Core sample information

This section describes the borehole where the used rock core samples were collected and the rock core samples themselves.

6.2.1 Drilling site

The rock core samples used in this study were obtained from a borehole located near the Nojima Fault, which is the source fault of the 1995 Mw 6.9 Kobe earthquake (also called

Hyogo-ken Nanbu earthquake). The Nojima Fault is a right-lateral strike-slip fault with minor thrust component. Its strike and dip are NE–SW and 75–80° southeast, respectively (Lin & Uda, 1996). The drilling was carried out from May 2017 to March 2018 for the purpose of collecting samples near the fault plane (Kyoto University, 2018). A total of five boreholes were drilled in this project, and the rock core samples used in this study were collected from the deepest borehole, called NFD-1. The locations of the boreholes and the geological map around the NFD-1 borehole are shown in Fig. 6-1. The NFD-1 borehole was drilled to a maximum depth of about 1000 m and penetrated the fault plane at a depth of about 500 m.

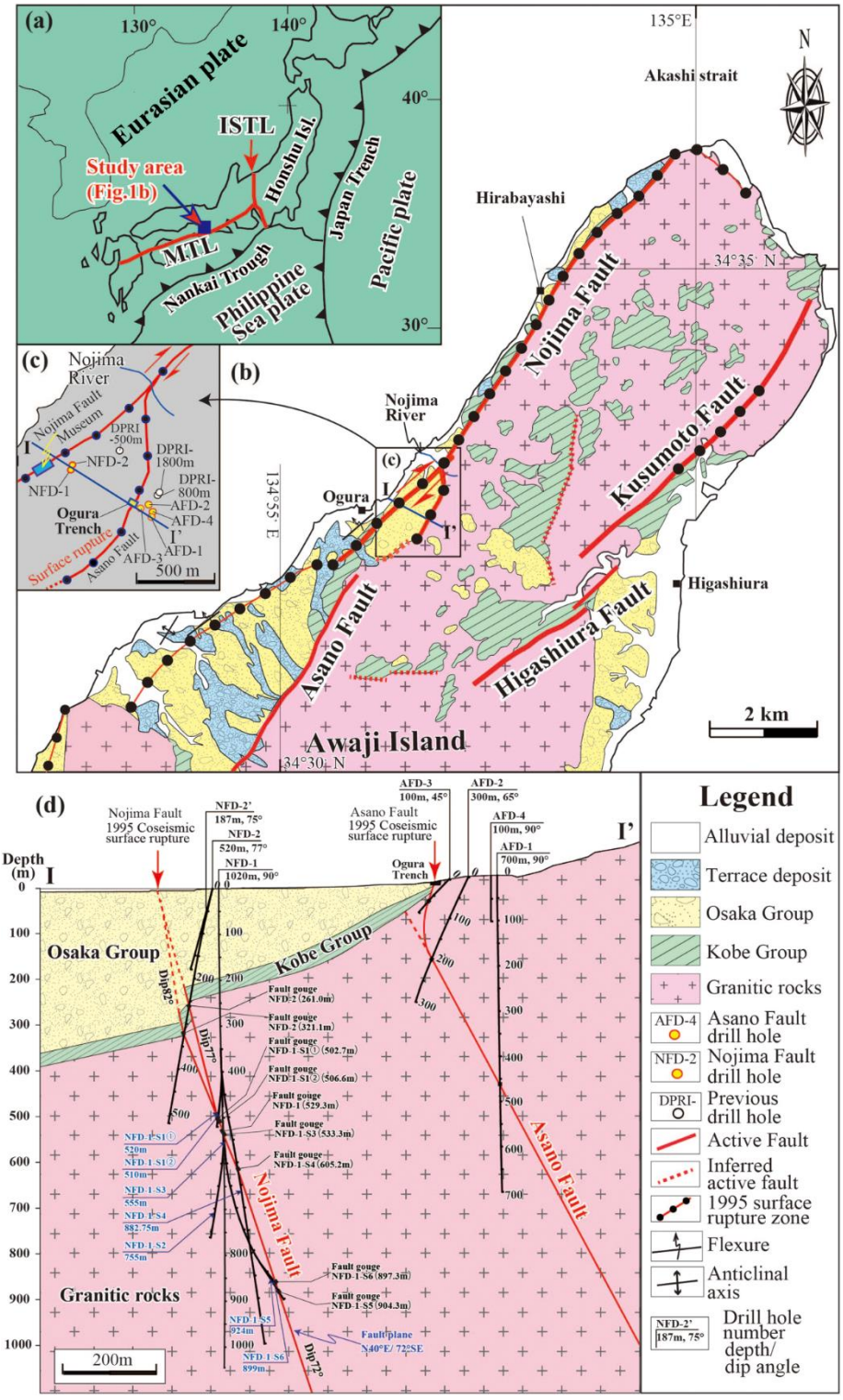

Fig. 6-1 Maps of the tectonic setting and geological structures around the NFD-1. (a) Tectonic setting of Japanese Islands. (b) Geological map of the northern part of Awaji Island. (c)Location of the NFD-1. (d) Geological section, fracture density and composite logging profiles of NFD-1 (After Nishiwaki & Lin, 2019).

6.2.2 Core samples

The rock core samples used for analysis were eight and Table 6-1 shows their basic information. The rock core samples were all composed of granite and were retrieved in the depth range of 700 m~730 m. The depth is on the foot wall of the Nojima Fault.

In order to determine the principal stress directions using a core sample, it is necessary to reorient the rock core sample. In this study, rock core samples were reoriented by matching the crack on the core surface with borehole images. The reference line orientation in the table is the position of the reference line taken at an arbitrary position on the core, measured eastward from north.

Table 6-1 Core sample information.

Sample ID	Core Top Depth (m)	Lithology	Reference line orientation (°)
ASR-17	710.78	granite	218.94
ASR-18	710.50	granite	252.22
ASR-19	711.34	granite	75.66
ASR-20	726.03	granite	243.74
ASR-21	726.24	granite	18.74
ASR-22	727.48	granite	179.12
ASR-23	727.61	granite	269.12
ASR-24	730.11	granite	147.83

6.3 ASR data

The used real ASR data were measured for each core sample using the same measurement system as described in Chapter 7. The measurement duration was about one month on average for each sample. However, considering the computational cost and the results in Chapter 5, the data up to about 48 hours after the start of measurement were used for the simulation. The anelastic normal strain recovery measurements using strain gauges were performed for the nine directions shown in Chapter 5, and two strain gauges were used in

each direction. In this study, the data in the same direction were arithmetically averaged and the averaged values were used as the measured values for each direction. Data with obvious measurement errors such as strain gage breakage during the measurement interval were excluded. In addition, data variation due to temperature change was removed by simple moving average filter using 11 data points.

Fig. 6-2 shows the measurement results of ASR-17 (depth 710.78 m) as an example. The data used in this study show a clear strain recovery curve, with recovery amounts ranging from a few hundred strains to several hundred strains in all directions.

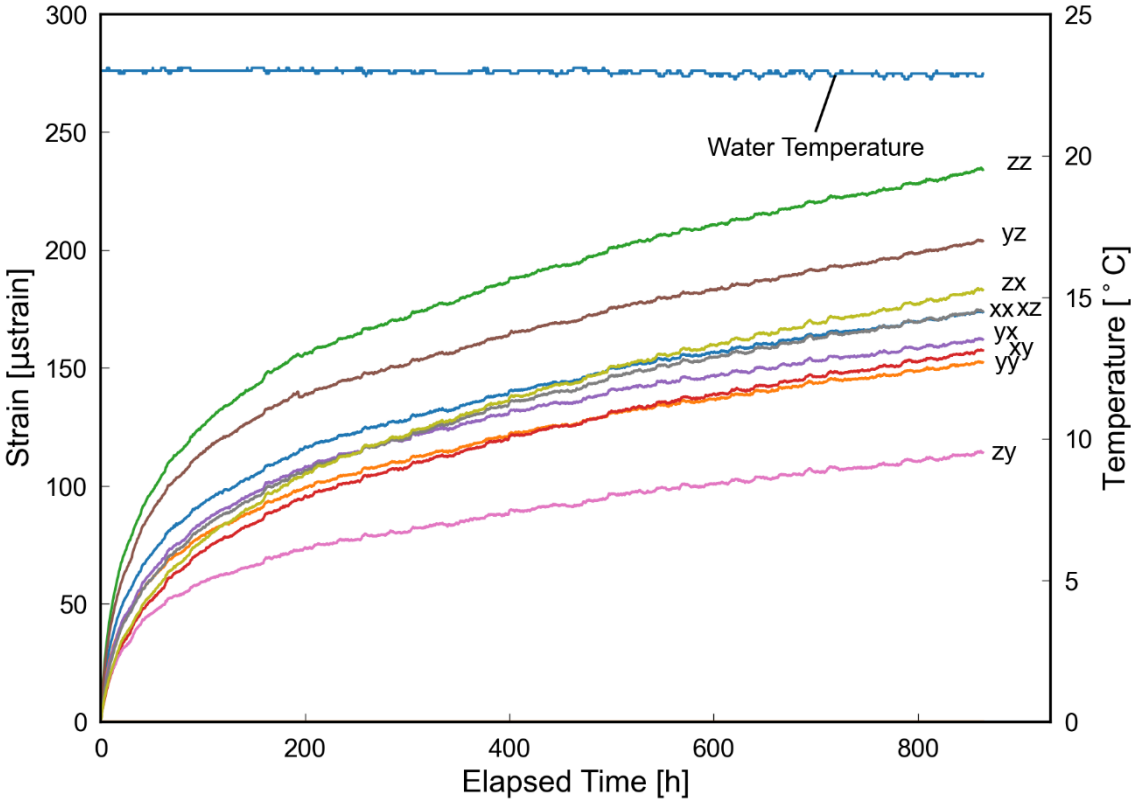

Fig. 6-2 ASR data of ASR-17 filtered by simple moving average using 11 data points (depth 710.78 m).

6.4 Probability model used for inference

6.4.1 Likelihood function

The likelihood function used in this study is the same as the one described in Chapter 5, except for one difference. The difference is in the handling of the measurement start time. The actual measurement starts about three hours after the stress release by drilling. Therefore, it is necessary to incorporate this fact into the model. In this study, the theoretical equation for anelastic normal strain was defined by

$$\bar{\boldsymbol{\varepsilon}}'(t_i, t_\mathrm{d}) = \bar{\boldsymbol{\varepsilon}}(t_i + t_\mathrm{d}) - \bar{\boldsymbol{\varepsilon}}(t_\mathrm{d}) \tag{6-1}$$

to incorporate the delay time into the model. The delay in starting the measurement was approximately 3 hours for all samples, thus the value $t_\mathrm{d} = 3$ hour. The likelihood function and other equations used are listed again below:

Likelihood function

$$\begin{aligned} L(D|\mathbf{w}) = &\prod_{i=1}^{9} \frac{1}{\sqrt{(2\pi)^9 |\boldsymbol{\Sigma}|}} \\ &\times \exp\left[-\frac{1}{2}\left(\boldsymbol{\varepsilon}_i - \bar{\boldsymbol{\varepsilon}}'(t_i, t_\mathrm{d})\right)^\mathrm{T} \boldsymbol{\Sigma}^{-1} \left(\boldsymbol{\varepsilon}_i - \bar{\boldsymbol{\varepsilon}}'(t_i, t_\mathrm{d})\right)\right] \end{aligned} \tag{6-2}$$

Constitutive equation of ASR

$$\varepsilon(t, \mathbf{n}) = \left(\sigma_{ij} n_i n_j - \sigma_\mathrm{m}\right) J_\mathrm{S}(t) + (\sigma_\mathrm{m} - p_0) J_\mathrm{V}(t) \tag{6-3}$$

Real ASR data

$$\boldsymbol{\varepsilon}_i = (\varepsilon_i^1, \varepsilon_i^2, \cdots, \varepsilon_i^9)^\mathrm{T} \tag{6-4}$$

ASR compliances

$$\begin{aligned} J_\mathrm{S}(t) &= \frac{1}{2G}\left(1 - \exp\left(-\frac{t}{\tau_\mathrm{s}}\right)\right) \\ J_\mathrm{V}(t) &= \frac{1}{3K}\left(1 - \exp\left(-\frac{t}{\tau_\mathrm{v}}\right)\right) \end{aligned} \tag{6-5}$$

6.4.2 Prior information

Uniaxial compression tests were conducted on two core samples taken from the same lithology and depth as the eight samples used in this study. From the results, the Young's modulus and the Poisson's ratio were calculated to be approximately 10 GPa and 0.25, respectively. Because the samples used in this study were retrieved from the same lithology and the same depth as two samples used for uniaxial compression tests, the elastic moduli are considered to be almost the same. Based on this consideration, these values were used as the elastic moduli for the eight samples used in this study. In addition, the overburden weight, which was calculated from the density profile of the rock, and the pore pressure, which was calculated from the groundwater level assuming a hydrostatic pressure condition, were also used as prior information. Therefore, the prior information 1, 2 and 3 defined in Chapter 5 can be used, and the simulations were performed in the same conditions as in Case-2 in Chapter 5. The prior distributions of vertical stress and pore pressure were set to a normal distribution with mean $\rho_{\mathrm{r}}gh$, $\rho_{\mathrm{w}}gh_{\mathrm{w}}$, and standard deviation of 5 MPa, as in Chapter 5.

6.5 Results

MCMC sampling was performed under the same conditions as in Chapter 5. Specifically, three independent MCMC sampling sequences consisting of 1500 samples were generated, and the first 500 samples were not used in subsequent analyses as a warm-up. The convergence of the simulation was verified using $\hat{R}$.

Fig. 6-3 shows the posterior distribution of σ_{11} for ASR-17 as an example of the inferred results. The distribution has a symmetrical unimodal shape. Similar results were obtained for the other inferred parameters for the other core samples.

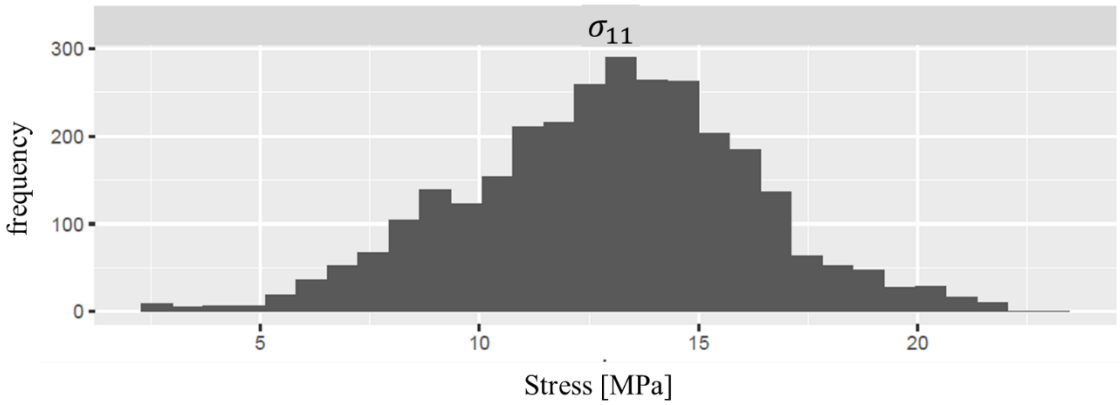

Fig. 6-3 Prior distribution of σ_{11} obtained from ASR-17 data.

Table 6-2 to Table 6-6 show the inferred results for the all parameters for the all core samples. The tables show the mean, left (2.5%) and right (97.5%) end of credible interval, and $\hat{R}$ of the inferred posterior distributions. The n_x, n_y, and n_z shown in Table 6-4 to Table 6-6 represent each component of the directional cosine vector indicating the principal stress directions in the core coordinate system. The simulation results showed that $\hat{R} < 1.1$ for all parameters for all samples, indicating that the simulation converged.

The standard deviation of each parameter shows that, as in the results for the simulated data in Chapter 5, the standard deviations are larger for the diagonal component of the stress tensor, while it is close to zero for the non-diagonal elements. For the diagonal elements, the standard deviation is 3 - 4 MPa, and this value is considered as the measurement error.

Table 6-2 Inference results (Part 1).

Sample ID	σ_{11} [MPa]				σ_{22} [MPa]				σ_{33} [MPa]				σ_{12} [MPa]				σ_{13} [MPa]				σ_{23} [MPa]			
	Mean	2.5%	97.5%	Rhat	Mean	2.5%	97.5%	Rhat	Mean	2.5%	97.5%	Rhat	Mean	2.5%	97.5%	Rhat	Mean	2.5%	97.5%	Rhat	Mean	2.5%	97.5%	Rhat
ASR-17	12.93	6.44	19.41	1.05	12.94	6.44	19.43	1.05	13.17	6.68	19.66	1.05	0.00	0.00	0.00	1.00	0.04	0.03	0.05	1.00	0.20	0.19	0.22	1.00
ASR-18	13.03	5.53	19.89	1.00	13.79	6.28	20.57	1.00	13.55	6.03	20.37	1.00	0.00	0.00	0.01	1.00	0.00	0.00	0.01	1.00	0.00	0.00	0.01	1.00
ASR-19	13.24	5.60	20.40	1.00	14.57	7.45	21.60	1.01	14.77	7.66	21.92	1.01	0.00	0.00	0.00	1.00	0.20	0.12	0.31	1.02	0.02	0.00	0.06	1.01
ASR-20	13.90	6.98	21.02	1.01	13.22	6.28	20.33	1.01	14.35	7.42	21.46	1.01	0.00	0.00	0.00	1.00	0.30	0.28	0.32	1.00	0.00	0.00	0.00	1.00
ASR-21	13.84	5.92	20.75	1.06	13.86	5.93	20.77	1.06	13.93	6.00	20.84	1.06	0.02	0.01	0.02	1.01	0.00	0.00	0.00	1.01	0.24	0.22	0.25	1.00
ASR-22	14.42	7.84	20.95	1.00	16.64	10.04	23.15	1.00	16.19	9.63	22.73	1.00	0.00	0.00	0.00	1.00	0.32	0.27	0.36	1.00	0.58	0.53	0.63	1.00
ASR-23	15.16	7.30	22.15	1.01	13.97	6.09	20.97	1.01	14.84	6.96	21.83	1.01	0.00	0.00	0.00	1.00	0.21	0.18	0.25	1.00	0.00	0.00	0.01	1.00
ASR-24	16.94	12.97	22.43	1.02	18.20	14.23	23.68	1.02	22.75	18.76	28.23	1.02	0.23	0.17	0.29	1.00	0.00	0.00	0.01	1.00	0.32	0.26	0.39	1.00

Table 6-3 Inference results (Part 2).

Sample ID	p_0 [MPa]				τ_V [h]				τ_S [h]				s [10^{-12}]			
	Mean	2.5%	97.5%	Rhat	Mean	2.5%	97.5%	Rhat	Mean	2.5%	97.5%	Rhat	Mean	2.5%	97.5%	Rhat
ASR-17	11.43	4.93	17.91	1.05	18.59	17.69	19.50	1.00	14.91	11.76	18.85	1.00	63.23	59.80	66.97	1.01
ASR-18	11.67	4.14	18.49	1.00	13.92	12.05	15.99	1.00	17.38	9.85	31.10	1.00	764.34	720.95	812.22	1.00
ASR-19	10.28	3.19	17.35	1.01	9.44	8.62	10.24	1.00	5.70	2.76	8.89	1.00	1465.28	1386.18	1550.33	1.00
ASR-20	10.88	3.94	18.01	1.01	15.72	15.01	16.47	1.00	13.26	11.28	15.35	1.00	237.55	224.11	251.72	1.00
ASR-21	12.13	4.20	19.02	1.06	19.04	18.21	19.90	1.00	16.39	12.86	20.86	1.01	53.82	50.79	57.06	1.01
ASR-22	9.93	3.33	16.47	1.00	13.75	12.94	14.61	1.00	10.16	8.22	12.39	1.00	1684.28	1591.13	1785.78	1.00
ASR-23	10.35	2.48	17.35	1.01	13.30	12.51	14.14	1.00	14.34	10.61	19.30	1.00	850.39	803.75	900.78	1.00
ASR-24	4.34	0.37	9.78	1.02	6.23	5.98	6.45	1.00	7.16	6.38	7.98	1.00	2610.46	2459.66	2762.70	1.00

Table 6-4 Inference result for the maximum principal stress σ_1.

Sample ID	σ_1															
	Magnitude [MPa]				n_x				n_y				n_z			
	Mean	2.5%	97.5%	Rhat	Mean	2.5%	97.5%	Rhat	Mean	2.5%	97.5%	Rhat	Mean	2.5%	97.5%	Rhat
ASR-17	13.29	6.79	19.78	1.05	-0.50	-0.52	-0.49	1.00	0.00	-0.02	0.01	1.00	0.86	0.86	0.87	1.00
ASR-18	13.79	6.28	20.57	1.00	0.00	0.00	0.01	1.00	-1.00	-1.00	-1.00	1.00	0.00	-0.02	0.02	1.00
ASR-19	14.80	7.69	21.94	1.01	0.07	-0.15	0.16	1.00	0.00	-0.13	0.25	1.00	-0.99	-1.00	-0.96	1.00
ASR-20	14.50	7.58	21.61	1.01	0.00	0.00	0.00	1.00	0.45	0.43	0.47	1.00	0.89	0.88	0.90	1.00
ASR-21	14.13	6.20	21.03	1.06	0.46	-0.66	0.66	1.01	0.06	-0.04	0.10	1.02	-0.75	-0.76	-0.74	1.00
ASR-22	17.05	10.45	23.56	1.00	-0.19	-0.21	-0.16	1.00	0.80	0.78	0.82	1.00	0.57	0.55	0.60	1.00
ASR-23	15.27	7.41	22.27	1.01	0.00	-0.01	0.00	1.00	0.89	0.87	0.92	1.00	0.45	0.39	0.49	1.00
ASR-24	22.78	18.79	28.26	1.02	-0.01	-0.01	-0.01	1.00	0.07	0.06	0.08	1.00	-1.00	-1.00	-1.00	1.00

Table 6-5 Inference result for the intermediate principal stress σ_2.

Sample ID	σ_2															
	Magnitude [MPa]				n_x				n_y				n_z			
	Mean	2.5%	97.5%	Rhat	Mean	2.5%	97.5%	Rhat	Mean	2.5%	97.5%	Rhat	Mean	2.5%	97.5%	Rhat
ASR-17	12.93	6.44	19.41	1.05	0.85	0.84	0.86	1.00	0.18	0.13	0.23	1.01	0.49	0.48	0.51	1.00
ASR-18	13.55	6.03	20.37	1.00	0.00	0.00	0.01	1.00	0.01	0.00	0.03	1.00	0.03	-1.00	1.00	1.00
ASR-19	14.56	7.45	21.60	1.01	0.00	0.00	0.00	1.00	0.55	-0.99	1.00	1.00	-0.08	-0.25	0.00	1.00
ASR-20	13.75	6.82	20.87	1.01	1.00	1.00	1.00	1.00	0.00	-0.01	0.00	1.00	0.00	0.00	0.00	1.00
ASR-21	13.84	5.92	20.75	1.06	-0.54	-0.76	0.76	1.01	-0.02	-0.04	0.01	1.01	-0.65	-0.67	-0.64	1.00
ASR-22	15.84	9.25	22.38	1.00	0.05	0.04	0.06	1.00	-0.58	-0.60	-0.55	1.00	0.82	0.80	0.83	1.00
ASR-23	14.73	6.85	21.74	1.01	1.00	1.00	1.00	1.00	0.00	0.00	0.01	1.00	0.00	0.00	0.00	1.00
ASR-24	18.22	14.24	23.70	1.02	0.18	0.13	0.22	1.00	-0.98	-0.99	-0.97	1.00	-0.07	-0.08	-0.06	1.00

Table 6-6 Inference result for the minimum principal stress σ_3.

Sample ID	σ_3															
	Magnitude [MPa]				n_x				n_y				n_z			
	Mean	2.5%	97.5%	Rhat	Mean	2.5%	97.5%	Rhat	Mean	2.5%	97.5%	Rhat	Mean	2.5%	97.5%	Rhat
ASR-17	12.81	6.33	19.30	1.05	0.16	0.11	0.20	1.01	-0.98	-0.99	-0.97	1.00	0.09	0.07	0.11	1.00
ASR-18	13.03	5.53	19.89	1.00	-1.00	-1.00	-1.00	1.00	0.00	-0.01	0.00	1.00	0.00	-0.01	0.00	1.00
ASR-19	13.22	5.56	20.38	1.00	-0.54	-1.00	0.99	1.00	0.00	-0.02	0.04	1.00	-0.12	-0.16	-0.09	1.00
ASR-20	13.22	6.28	20.33	1.01	0.00	-0.01	0.00	1.00	-0.89	-0.90	-0.88	1.00	0.45	0.43	0.47	1.00
ASR-21	13.65	5.73	20.57	1.06	0.05	-0.05	0.10	1.01	-0.85	-1.00	1.00	1.02	-0.04	-0.06	-0.02	1.01
ASR-22	14.36	7.79	20.89	1.00	0.98	0.98	0.99	1.00	0.18	0.15	0.20	1.00	0.07	0.06	0.08	1.00
ASR-23	13.97	6.09	20.97	1.01	0.00	0.00	0.00	1.00	-0.45	-0.49	-0.39	1.00	0.89	0.87	0.92	1.00
ASR-24	16.90	12.92	22.39	1.02	-0.98	-0.99	-0.97	1.00	-0.18	-0.22	-0.13	1.00	0.00	-0.01	0.00	1.00

Fig. 6-4 shows the lower hemisphere equal area projections of the reoriented three principal stresses for each core sample. The figure shows all 3000 samples excluding the warm-up samples for each principal stress. The maximum principal stresses (σ_1) are represented by red circles, the intermediate principal stresses (σ_2) by green circles, the minimum principal stresses (σ_3) by blue circles, respectively.

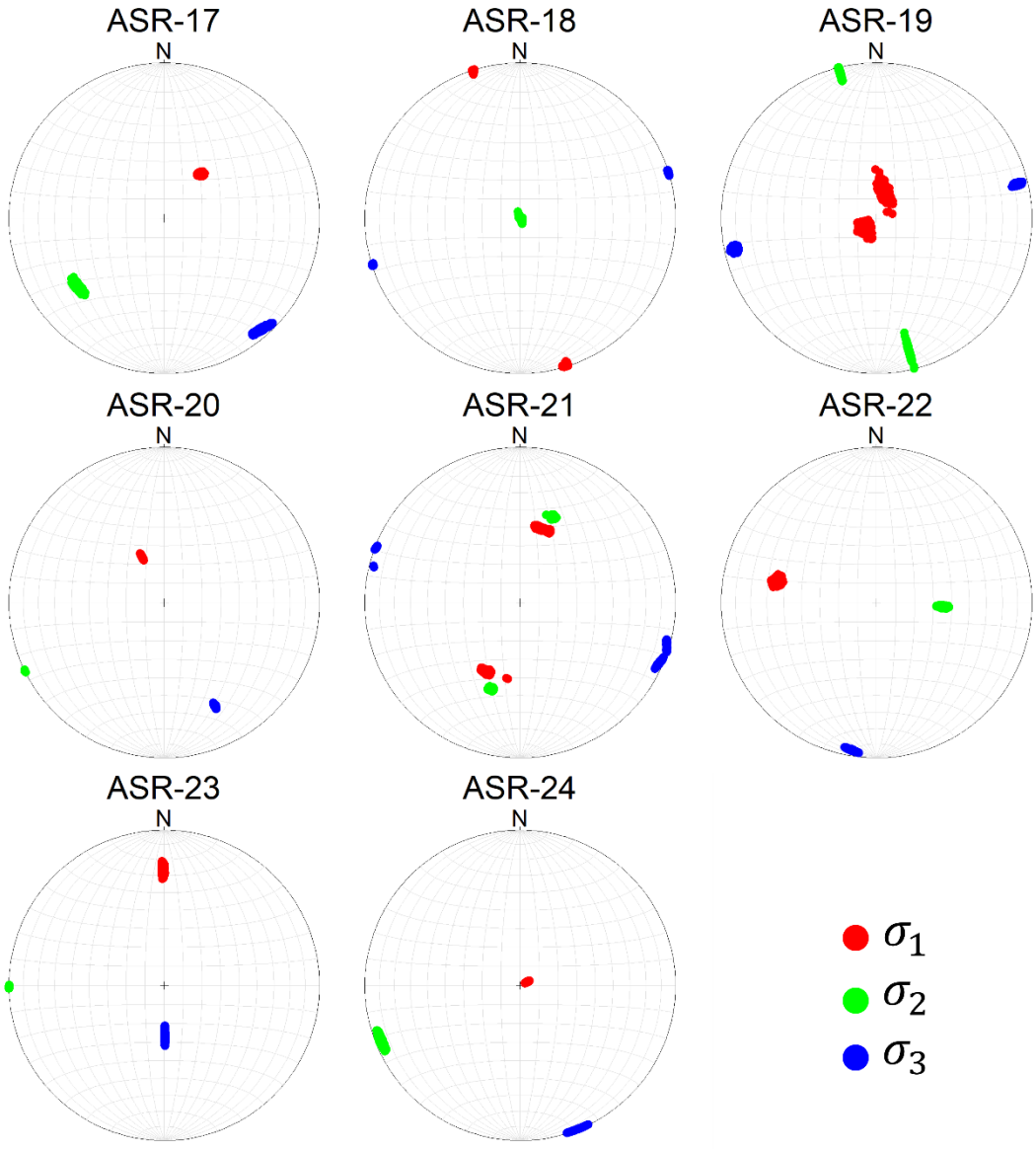

Fig. 6-4 Lower hemisphere equal area projection of the three principal stresses of each sample.

Rose diagrams showing the maximum horizontal principal stress orientations obtained from the inferred stress tensors are shown in Fig. 6-5, and the maximum and minimum horizontal principal stress orientations and magnitudes are shown in Table 6-7. From Fig. 6-5, it can be seen that there are two trends in the direction of the maximum horizontal principal stress; ASR-17 20, 21, 22, 24, show the orientations of NE-SW to E-W, which is subparallel to the fault plane of the Nojima Fault; .ASR-18, 19, 23 show the orientation of NW-SE to N-S, which is almost perpendicular to the fault plane.

The reason for these results is that the values of $S_{\mathrm{Hmax}} - S_{\mathrm{hmin}}$ are very small. For all the rock core samples, $S_{\mathrm{Hmax}} - S_{\mathrm{hmin}}$ values close to 1 MPa, which is less than the measurement uncertainty based on the novel analysis. In other words, the maximum and minimum horizontal principal stresses are easily exchangeable.

In the next section, the validity of this method is discussed by comparing the results of stress measurements by the hydraulic fracturing method and the borehole breakout method.

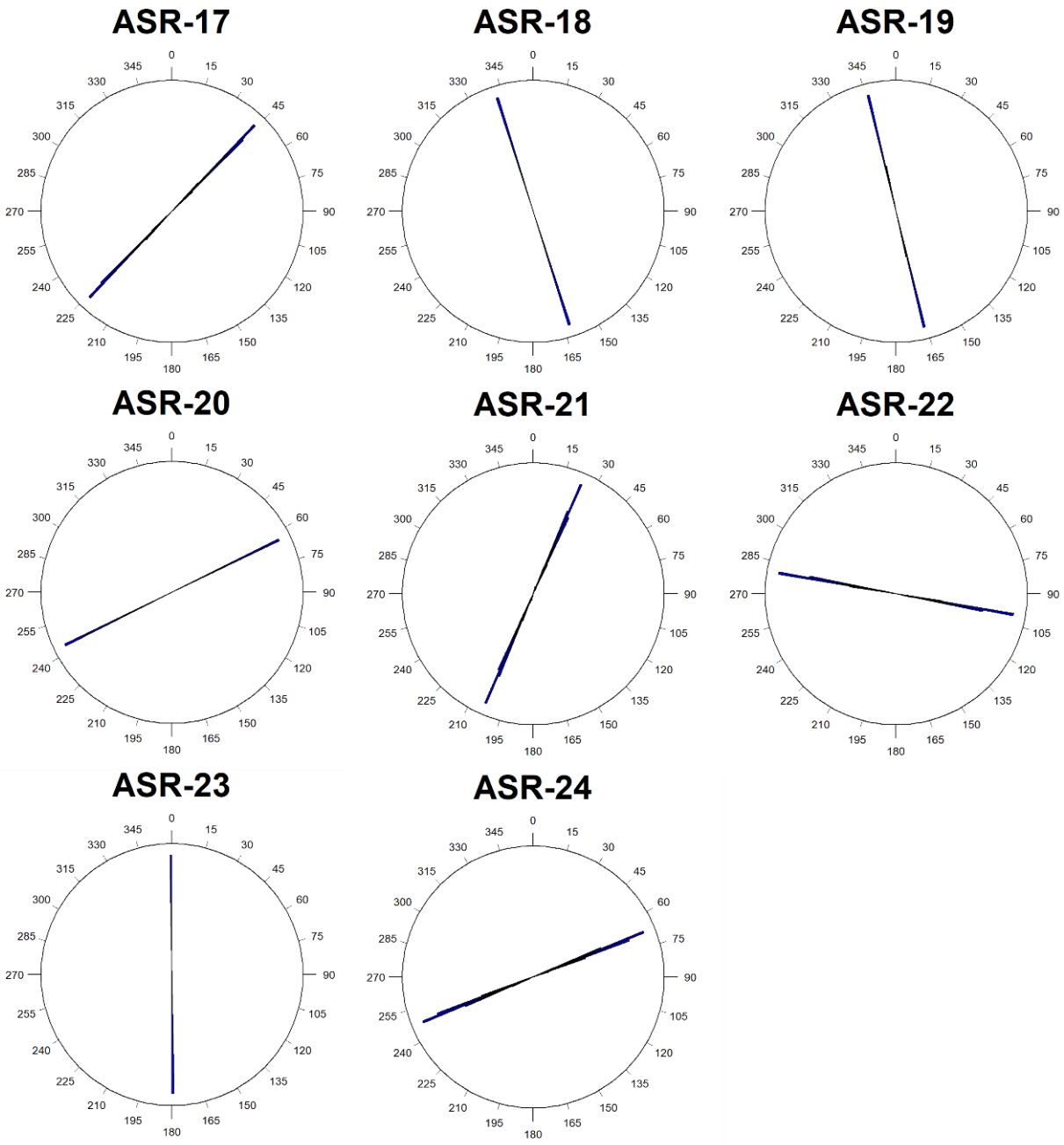

Fig. 6-5 Rose diagrams showing S_{Hmax} orientation obtained by the procedure proposed in this study. The north is located 0°.

Table 6-7 Inference results of horizontal stresses.

Sample ID	Core Top Depth (m)	S_{Hmax}						S_{hmin}					
		Magnitude (MPa)			Orientation (°)			Magnitude (MPa)			Orientation (°)		
		Mean	2.5%	97.5%	Mean	2.5%	97.5%	Mean	2.5%	97.5%	Mean	2.5%	97.5%
ASR-17	710.78	13.0	6.5	19.5	224.2	222.5	226.0	12.8	6.3	19.3	314.2	312.5	316.0
ASR-18	710.50	13.8	6.3	20.6	342.2	342.0	342.8	13.0	5.5	19.9	252.2	252.0	252.8
ASR-19	711.34	14.6	7.5	21.6	166.7	166.0	168.4	13.2	5.6	20.4	76.7	76.0	78.4
ASR-20	726.03	13.7	6.8	20.9	243.9	243.5	244.0	13.5	6.6	20.6	333.9	333.5	334.0
ASR-21	726.24	14.0	6.0	20.9	23.0	15.0	26.0	13.7	5.7	20.6	113.0	105.0	116.0
ASR-22	727.48	16.6	10.1	23.2	280.3	278.7	282.0	14.4	7.8	20.9	190.3	188.7	192.0
ASR-23	727.61	15.0	7.2	22.0	359.3	359.0	360.0	14.7	6.8	21.7	269.3	269.0	270.0
ASR-24	730.11	18.2	14.3	23.7	248.2	245.5	250.8	16.9	12.9	22.4	158.2	155.5	160.8

6.6 Discussion

In this drilling project, the borehole breakout method has been carried out in the NFD-1 borehole (Nishiwaki et al., 2018) and the hydraulic fracturing method has been conducted around 700 m depth in the AFD-1 borehole (Kyoto University, 2018; Yokoyama et al., 2019). In this study, the applicability of the novel analysis procedure to real data was examined by comparing the results of the two stress measurements with those inferred by the novel analysis procedure. First, the validity of the novel procedure is examined based on the maximum horizontal principal stress directions calculated by Kyoto University (2018) and Nishiwaki et al. (2018).

Fig. 6-6 shows the rose diagram showing S_{Hmax} orientation obtained by the borehole breakout method. This measurement was carried out in the NFD-1 borehole. The results show that the maximum horizontal principal stress direction is NE-SW at depths between 600 m and 1000 m.

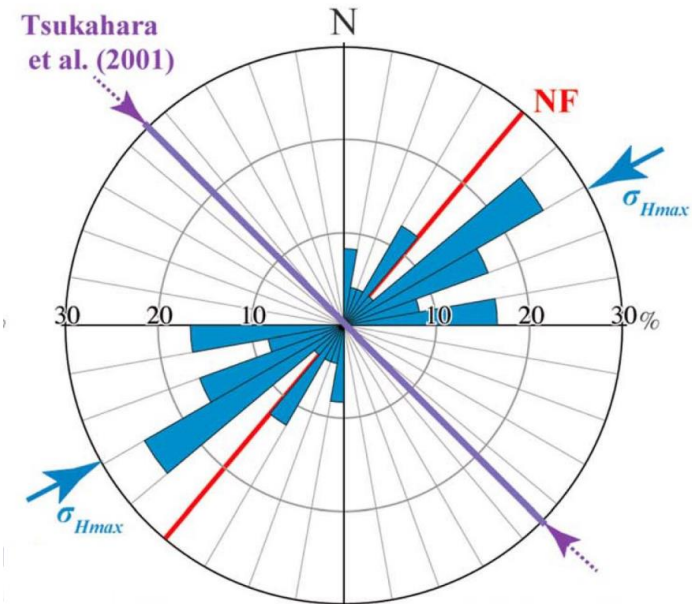

Fig. 6-6 S_{Hmax} orientations obtained by borehole breakout method. (After Nishiwaki et al., 2018).

Fig. 6-7 shows the maximum horizontal principal stress direction obtained by the hydraulic fracturing method. The fracture orientation was measured using a packer.

The results were measured in the AFD-1 borehole, and measurements were carried out in three sections from 725 m to 770 m depth. The results show that two orthogonal trends (NE-SW and NW-SE) have been obtained.

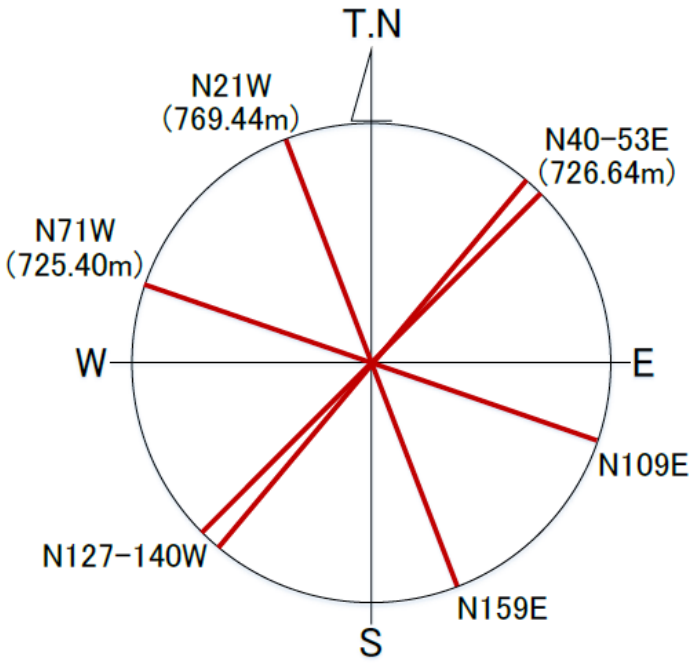

Fig. 6-7 S_{Hmax} orientations obtained by hydraulic fracturing method. (After Kyoto University, 2018).

The reason why the hydraulic fracturing results show such two different trends is not described in Yokoyama et al. (2019). However, as shown in Table 6-8, the maximum horizontal principal stress direction can be easily rotated by 90° because the value of $S_{\mathrm{Hmax}} - S_{\mathrm{hmin}}$ in the 769 m section is very small.

Based on these two results, the true maximum horizontal principal stress orientations at the depth of 700 m is assumed to be NE-SW or NW-SE. Considering the fact that $S_{\mathrm{Hmax}} - S_{\mathrm{hmin}}$ is very small in the novel analysis procedure, the results are in very good agreement with the inference results of the maximum horizontal principal stress direction shown in Fig. 6-5.

Next, the magnitudes of the maximum and minimum horizontal principal stresses obtained by the hydraulic fracturing method and those obtained by the novel

analysis procedure are compared. The minimum horizontal principal stress values obtained by the hydraulic fracturing method are 12-15 MPa in the 725 m and 726 m sections, which are in good agreement with the values obtained by the novel procedure. On the other hand, the maximum horizontal principal stress values of 19-26 MPa were obtained by the hydraulic fracturing method. These values are larger than the results of the novel procedure considering the uncertainty. This point requires further investigation, considering the reliability of the maximum horizontal principal stress value obtained by the hydraulic fracturing method.

Table 6-8 Hydraulic fracturing results obtained in the AFD-1 borehole. (After Yokoyama et al., 2019).

Depth (m)	P_b (MPa)	P_s (MPa)	P_r (MPa)	P_p (MPa)	S_h (MPa)	S_H (MPa)	σ_z (MPa)	θ	Q (ml/min)
725.40	13.5	–	7.5	6.9	–	–	18.7	N41E N109E	10
		12.0	8.2		12.0	19.6			50
		11.8	8.4		11.8	18.6			80
		11.8	8.2		11.8	19.0			50
		12.0	8.2		12.0	19.6			50
			Average		11.9	19.2			–
726.64	17.2	14.7	8.1	6.9	14.7	27.9	18.7	N40E N233E	50
		14.6	8.2		14.6	27.4			80
		15.3	9.1		15.3	27.7			100
		15.0	9.0		15.0	27.0			100
		14.8	9.5		14.8	25.4			100
		14.8	10.2		14.8	24.0			150
		14.8	10.2		14.8	24.0			150
			Average		14.9	26.2			–
769.44	13.9	9.1	7.7	7.5	9.1	11.9	19.8	N21W	10
		9.0	7.7		9.0	11.6			10
		9.1	7.7		9.1	11.9			10
		9.1	7.7		9.1	11.9			10
			Average		9.1	11.8			–

Depth :Depth of test interval
P_b :Break down pressur
P_s :Shut-in pressure
P_r :Reopening pressure
P_p :Pore pressure
S_h :Minimum principal stress
S_H :Maximum principal stress
σ_z :Over burden pressure
θ :Azimuth of principal maximum stress
Q :Flow rate

6.7 Summary

In this chapter, the novel analysis procedure for ASR data proposed in Chapter 5 is applied to the real ASR data of core samples obtained in the vicinity of the Nojima Fault, and examined the validity of the procedure. The simulation converged for all eight samples used in the simulation, and the standard deviation inferred showed the same trend as the results for the simulated data in Chapter 5. This indicates that the simulations on the real data were successful.

By comparing the stress estimates obtained by the novel procedure with those obtained by the hydraulic fracturing and borehole breakout methods, the maximum and minimum horizontal principal stress orientations were agreed with each other. The validity of this method should be further examined by applying it to other regions and various rock types for future work.

References

Kyoto University. (2018). *FY29 Commissioned for the disaster prevention on nuclear facilities (Dating Analyses of Drilling cores at the Futagawa fault), Technical Report (in Japanese)*. 208. https://www.nsr.go.jp/nra/chotatsu/yosanshikou/itaku_houkoku_h29.html

Lin, A., & Uda, S. (1996). Morphological characteristics of the earthquake surface ruptures on Awaji Island, associated with the 1995 Southern Hyogo Prefecture Earthquake. *Island Arc*, *5*(1), 1–15. https://doi.org/https://doi.org/10.1111/j.1440-1738.1996.tb00008.x

Nishiwaki, T., & Lin, A. (2019). Fractures and Subsidiary Faults Developed in the Active Strike-Slip Nojima Fault Zone, Japan, and Tectonic Implications. *Tectonics*, *38*(12), 4290–4300.

Nishiwaki, T., Lin, A., & Lin, W. (2018). Recovery of Stress During the Interseismic Period Around the Seismogenic Fault of the 1995 Mw 6.9 Kobe Earthquake, Japan. *Geophysical Research Letters*, *45*(23). https://doi.org/10.1029/2018GL079317

Yokoyama, T., Murakami, M., Danjo, T., Ogawa, K., Lin, A., Lin, W., & Ito, T. (2019). Rock stresses around active faults measured by using the high stiffness hydraulic fracturing technique. *Rock Dynamics Summit - Proceedings of the 2019 Rock Dynamics Summit*, 616–621.

Chapter 7

Stress State Around the Source Fault of the 2016 Kumamoto Earthquakes

7.1 Introduction

The relationship between earthquakes and stresses has been extensively studied (e.g., (Hardebeck, 2004, 2012; Hardebeck & Hauksson, 2001; Lin et al., 2013; Nishiwaki et al., 2018; Stein, 1999; Toda et al., 1998). These studies revealed that the stress state in the fault zone influences the rupture process of the fault, and that the stress state in the fault zone is significantly changed by the motion of the fault during an earthquake. On the other hand, there is still much that remains to be clarified. In particular, there are few detailed in-situ stress measurements in the vicinity of the source fault, and more actual measurement results are needed for more accurate discussion.

The 2016 Kumamoto earthquake consisted of a series of earthquakes that began with an M_{JMA} 6.5 earthquake (henceforth referred to as the foreshock) with an epicenter on April 14, 2016 at 21:26 JST. on the northern part of the Hinagu Fault (Japan Meteorogilcal Agency, 2016). On April 16, 2016, at 1:25 JST., approximately 28 hours after the previous earthquake, an earthquake with an M_{JMA} of 7.3 (hereafter referred to as the mainshock) occurred. Asano & Iwata (2016) and Kubo et al. (2016) pointed out that this series of earthquakes was generated by a complex mechanism where the rupture of the mainshock started from the deep portion of a northwest-dipping fault plane along the

Hinagu Fault and continued to be transferred to the Futagawa Fault and propagated northeastward and upward to generate significant slips with surface breaks. Matsumoto et al. (2015), Yoshida et al. (2016), Matsumoto et al. (2018), Yu et al. (2019) and Mitsuoka et al. (2020) determined the stress state around the epicenter area (10-20 km depth) before and after the earthquakes based on the focal mechanism solution, and they found that, between the foreshock and the mainshock, the direction and absolute value of the principal stress varied greatly in time and space.

Although the determination of the stress state by the seismic mechanism is useful for determining the regional stress field, more detailed in-situ stress measurements such as hydraulic fracturing, analysis of borehole breakout, and in-situ stress measurements using rock core samples are required to determine the in-situ stress near the fault. In this study, in-situ stress measurements in the vicinity of the fault were carried out by applying inelastic strain recovery method, one of the stress measurement methods using core samples, to rock core samples taken during scientific drilling (Kyoto University, 2018) near the source fault after the 2016 Kumamoto earthquakes.

7.2 Drilling site

In this study, ASR method was applied to the core samples collected during scientific drilling (Kyoto University, 2018) that took place between September 2017 and March 2018. The drilling site is located at the southwest part of the Futagawa Fault (32°48'22" N, 130°51'36" E, Fig. 7-1), and a vertical borehole with a maximum depth of about 700 m was drilled. The hole was drilled down to 666 m, and then branch drilling was carried out from 450 m down to 691 m (slope of about 1°). The former is called FDB-1 and the latter is called FDB-1R, and they are collectively called FDB.

The depth of the FDB-1R borehole is strictly the drilling depth, but since the inclination of the borehole is small (about 1°), it is considered the same as the vertical depth in this paper. FDB-1 penetrates faults at depths of 354 m, 461 m, and 576 m, and the similar fault to the one at 576 m has been identified in FDB-1R at a depth of 598 m (Kyoto University, 2018; Shibutani et al., 2019).

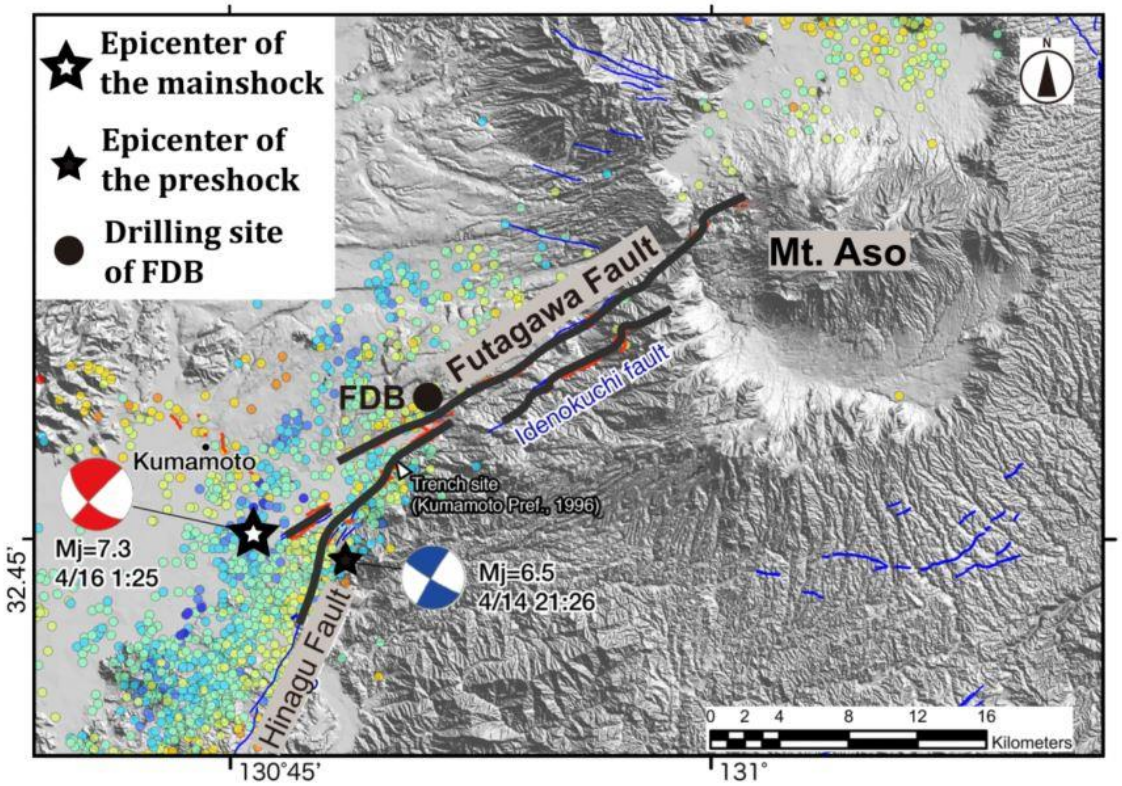

Fig. 7-1 Map around the drilling site. A black circle (FDB) in the figure indicates the location of the borehole, and black and white stars indicate the epicenter of the foreshock (April 14, 2016) and the mainshock (April 16, 2016), respectively. Small circles in the figure indicate the epicenters of earthquakes of magnitude 2.0 or greater that occurred between the mainshock and May 4, 2016. (Modified from Toda et al. 2016).

7.3 Core samples

The core samples were taken in the interval between the FDB-1 and FDB-1R boreholes at a depth of 302 m to 691 m (Fig. 7-2). A total of 20 core samples collected from the FDB were used for ASR measurements. For 14 samples above 505 m depth, the maximum ASR was less than 100 μstrain, which is comparable to the noise caused by room temperature changes, and it was difficult to accurately distinguish the strain recovery from the noise. Therefore, core samples shallower than about 505 m in depth could not be used

for in-situ stress analysis.

The six core samples shown in Table 7-1 and Fig. 7-2 were used in the analysis, collected in the range of 518-667 m depth. FDB-11, 12, and 13 were sampled from the upper part of Fault 576 (Fault 598), and FDB-16, 17, and 19 were sampled from the lower part of Fault 576.

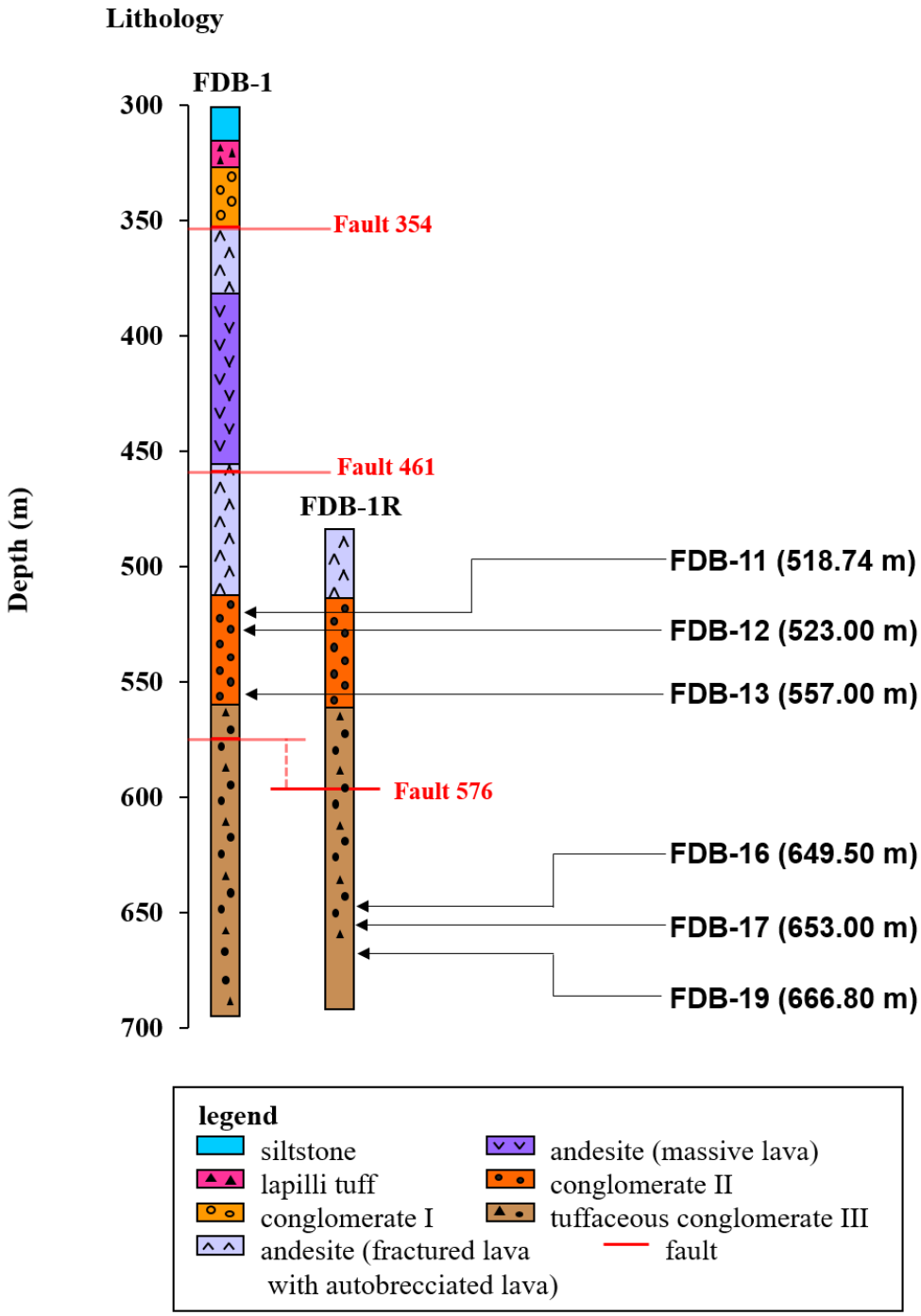

Fig. 7-2 Figure showing the geological column of the FDB. Fault depths and sampling locations are also indicated in Fig. 7-1. The depth of the lithological boundary was confirmed by FDB-1, and fault 598 is the same fault as fault 576, which was confirmed by FDB-1R. (Modified from Shibutani et al., 2021).

Table 7-1 Information of the core samples.

Sample ID	Borehole	Core Top Depth (m)	Wet bulk density (10^3 kg/m^3)	Porosity (%)	Lithology
FDB-11		518.74	2.42	11.5	andesite block in conglomerate
FDB-12	FDB-1	523.00	2.01	39.0	siltstone
FDB-13		557.00	1.93	49.3	sandstone
FDB-16		649.50	2.29	26.1	conglomerate
FDB-17	FDB-1R	653.00	2.63	10.5	andesite
FDB-19		666.80	1.90	48.1	conglomerate

7.4 Measuring System

A schematic diagram and picture of the measuring system used in this study are shown in Fig. 7-3 and Fig. 7-4. The anelastic normal strain recovery of each core sample was measured continuously by strain gauges with an accuracy of less than ±10 μstrain over a period of at least two weeks. Tokyo Measuring Instruments Laboratory's FLA-10-11 (single-gauge) and FCA-10-11 (cross-gauge) strain gages were used, and Kyowa Dengyo's UCAM-60B-AC and USB-70B-10s were used as data loggers and scanning boxes, respectively. The sampling interval is set to be 10 minutes.

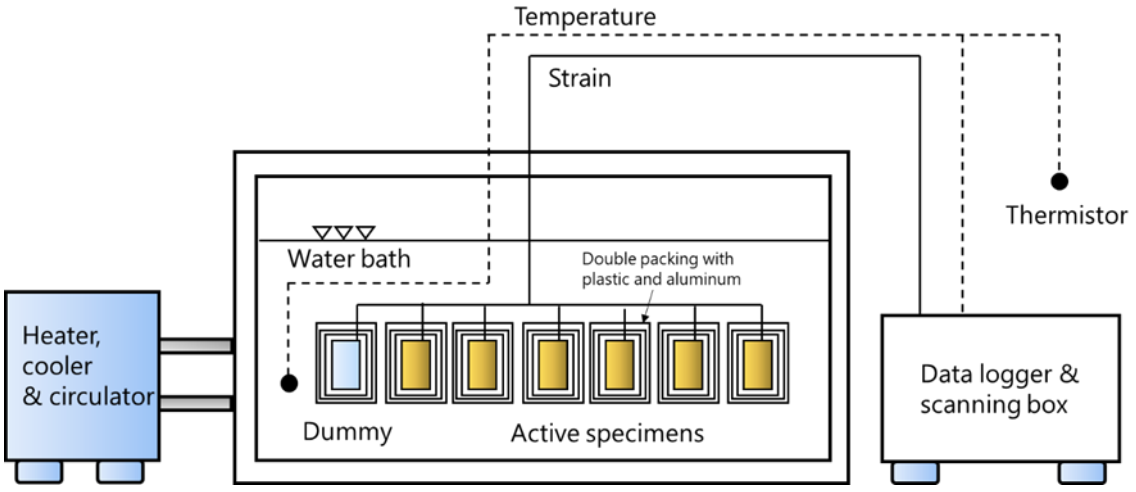

Fig. 7-3 Schematic diagram of ASR meausring system.

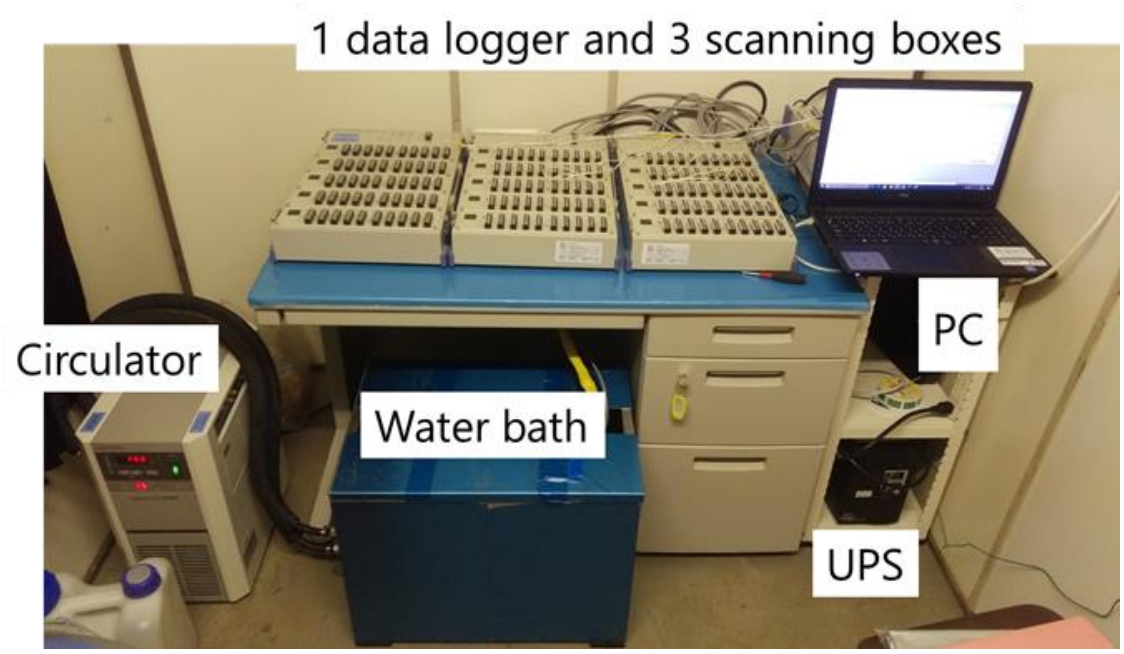

Fig. 7-4 ASR measuring system.

The measurements were performed in a measurement room on-site because it is desirable to perform the measurements as soon as possible after drilling. Measurements of anelastic normal strain recovery for each core sample in this study were initiated within 2-3 hours after drilling. The strain gages were attached to the core samples using adhesive before pore water dries up. In order to consider the possibility of measurement defects such as strain gauge breakage during the measurement period, the anelastic normal strain recovery in 9 directions (shown in Fig. 7-5), including 6 independent directions was measured using two strain gages in each direction, with a total of 18 strain gages. By using the least-squares method for the obtained inelastic vertical strain recovery in nine directions, $\varepsilon_{ij}(t)$ is calculated. Fig. 7-6 shows the used core sample (FDB-11).

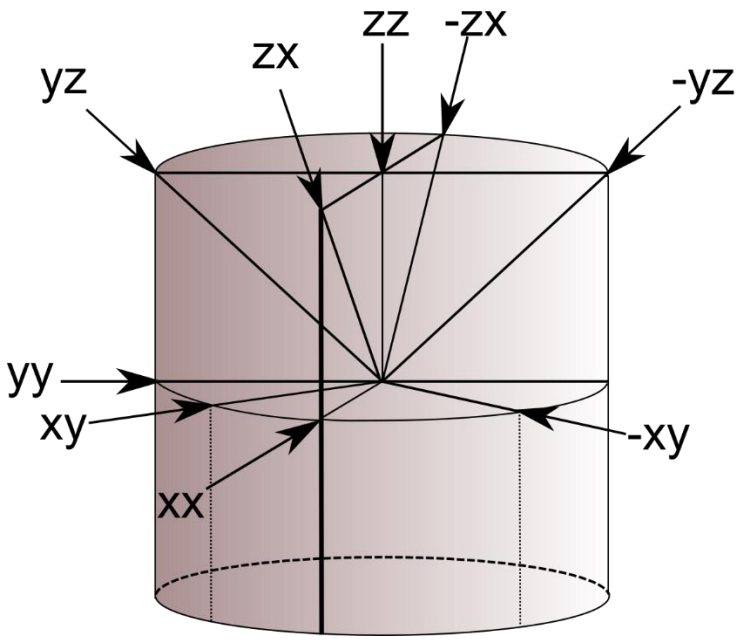

Fig. 7-5 Nine directions in which anelastic normal strains are measured with strain gauges.

To prevent thermal expansion and shrinkage, the core samples to which strain gauges were attached were placed in a sealed waterproof plastic and aluminum bag and placed in a thermostatic bath (Fig. 7-7). The water temperature in the thermostatic bath was controlled by the temperature control system to be within the range of 15.0±0.2 °C, and the system was continuously checked by a thermometer to ensure proper operation. In this study, we will not consider thermal expansion and contraction because $\Delta T(t) \approx 0$.

The strains were measured using a three-wired connection method that allows self-temperature compensation of the strain gauge leads. If the room temperature variation is large and the effect on the measuring device cannot be ignored, the measured values are corrected based on the strain data of a dummy sample (core sample for which ASR is already finished) that is being measured at the same time as the measured sample (e.g., Lin et al. (2007)). In this study, we did not perform this correction because there were no samples that could be corrected by a dummy sample.

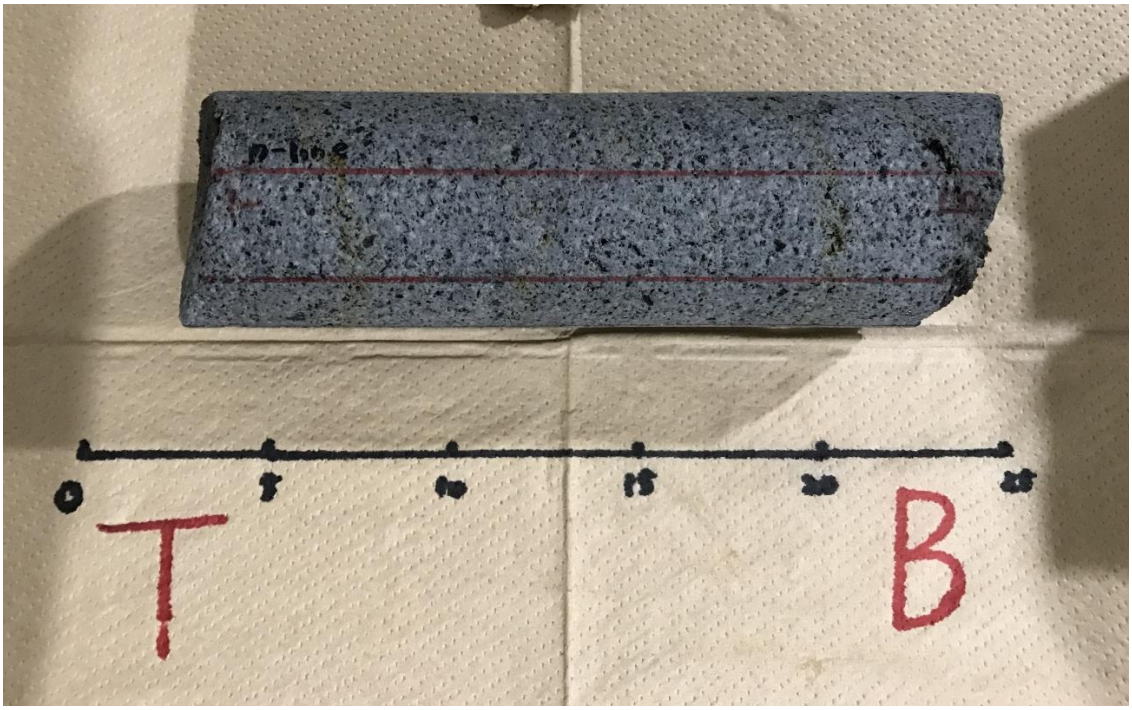

Fig. 7-6 Picture of used core sample (FDB-11).

Fig. 7-7 Core sample packed by aluminium bag.

7.5 Result

7.5.1 Result of ASR measurement

Fig. 7-8 shows the ASR results for FDB-12 taken from the 523.00 m depth of the FDB-1 hole (all sampling depths are represented by the depth of the top of the core sample). The measurement period for this data was 35 days.

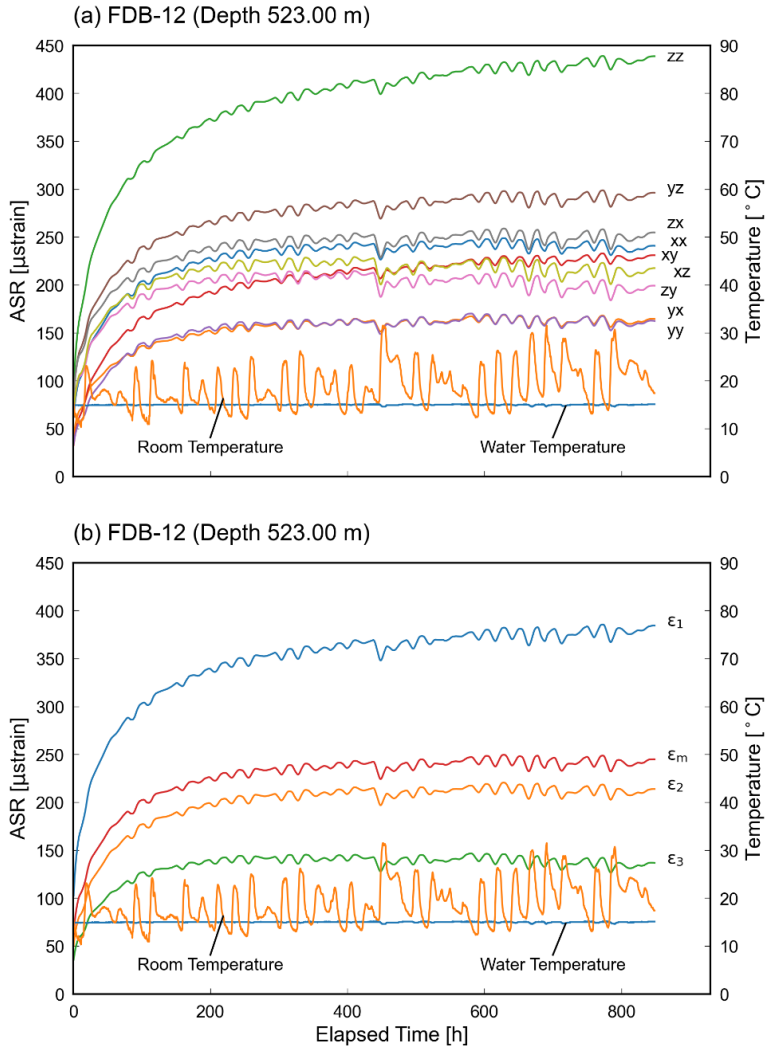

Fig. 7-8 ASR results for sample FDB-12 (FDB-1 hole, 523.00 m depth). (a) Anelastic normal strain recovery in nine directions and room and water temperatures with time. (b) ASR in the three principal strain directions and mean normal strain direction, as well as changes in room and water temperature with time.

Fig. 7-8 (a) shows the ASR in the nine directions, and Fig. 7-8 (b) shows the ASR in the three principal strain directions and average anelastic normal strain recovery obtained from the anelastic normal strain recovery shown in Fig. 7-8 (a). The letters such as xx in Fig. 7-8 (a) indicate the direction, and ε_1, ε_2, ε_3, and ε_{m} in Fig. 7-8 (b) represent the maximum, intermediate, minimum, and mean normal strain recovery, respectively. Fig. 7-8 shows the temperature in the water bath and the room temperature in the measurement room during the measurement period. The water temperature variation was kept within ±0.2 °C, confirming that the temperature control system was working properly.

The final anelastic normal strain recovery was in the range of 100-400 μstrain in all nine directions, which was greater than the accuracy of the measurement system (±10 μstrain), and the clear trend of ASR made it possible to use these data for three-dimensional stress analysis.

A fluctuation of a few to dozens of μ strains was observed in the strain data. However, as shown in Fig. 7-8, the correlation with the daily variation of room temperature above 10°C was observed, which indicates that this was due to the effect of temperature change to which the recording system was subjected. These effects were confirmed to be negligible because there was no significant difference between the stress results obtained from unprocessed ASR data and those obtained from the moving-averaged ASR data.

On the other hand, for samples shallower than 505 m, for which stress analysis was not possible, the ASR curve was obscured by noise from room temperature changes because the ASR was as small as ~60 μstrain, as shown in Fig. 7-9. The sample in Fig. 7-9 (a) were collected from a depth of 336.84 m. Due to a power outage that occurred at the drilling site during the measurement period of this sample, the temperature could not be properly controlled for about 60-140 hours after the start of measurement.

The sample in Fig. 7-9 (b) was collected from a depth of 505.53 m. There was a tendency to increase the strain due to ASR, but it was comparable to the noise from room temperature changes. Both samples could not be used for stress analysis because the ASR was unclear. The cause of this small ASR can be due to the small absolute value of in-situ

stress and the small ASR compliance of the rock.

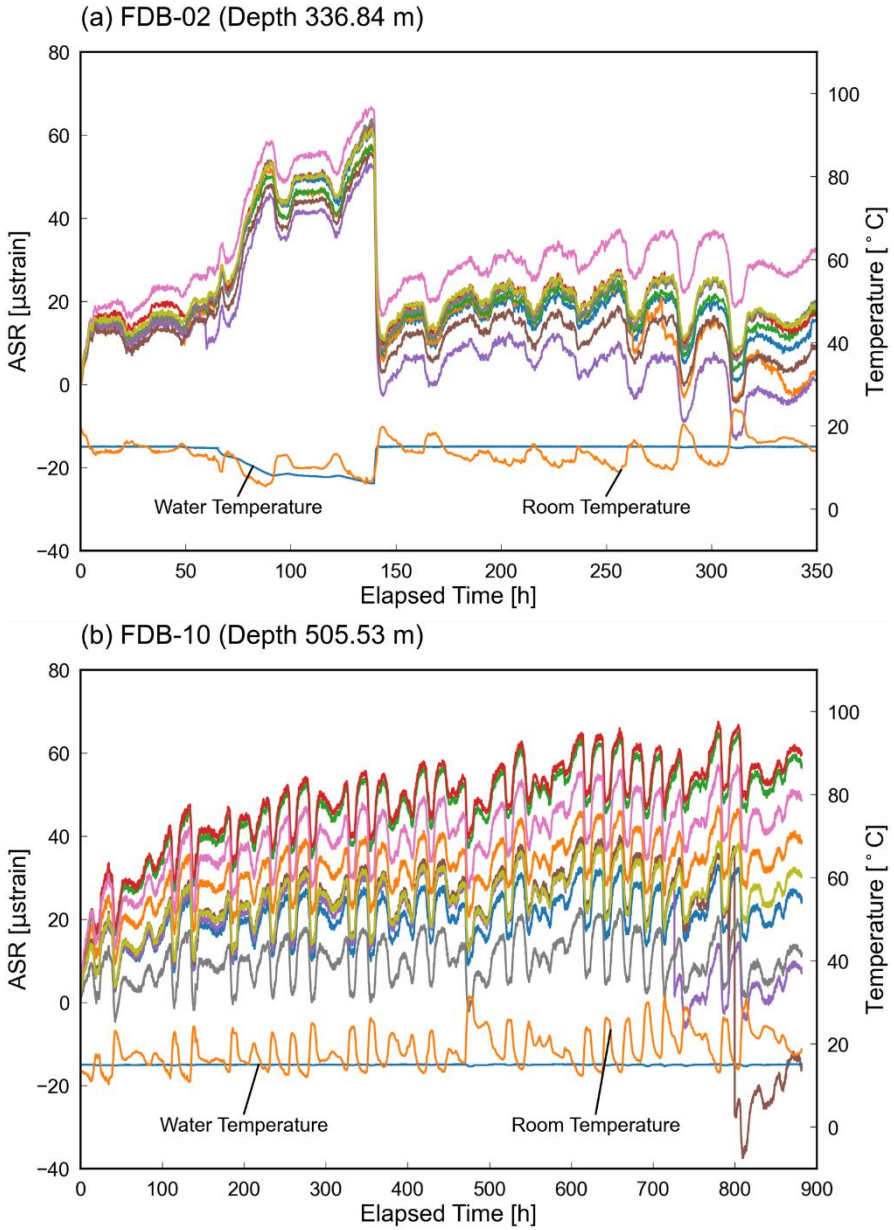

Fig. 7-9 Examples of ASR measurement results for which stress analysis was not possible. (a) FDB-02 (FDB-1 hole, depth 336.84 m). (b) FDB-10 (FDB-1 hole, depth 505.53 m).

7.5.2 Orientations of principal stresses

Fig. 7-10 shows the results of reorientation of FDB-12 and FDB-19 using rock remanent magnetization detailed in Chapter 4. Fig. 7-10 (a) and (c) is called the Zijderveld diagram,

which projects the endpoints of the remanent magnetization vectors obtained by progressive demagnetization of the remanent magnetization recorded in the core sample (Butler, 1992).

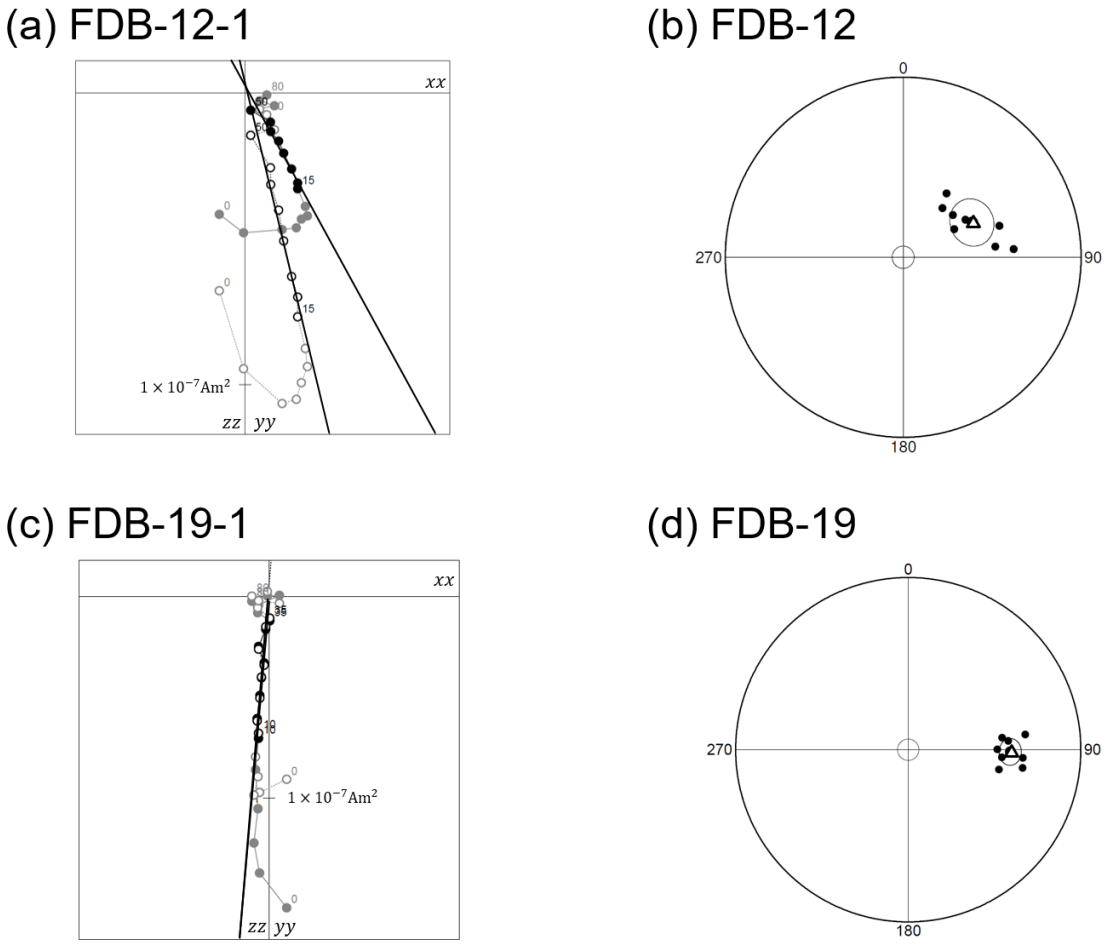

Fig. 7-10 Results of FDB-12(a, b) and FDB-19(c, d) reorientation. (a, c) Projection of the progressive demagnetization onto Zijderveld diagrams. The xx, yy, and zz axes in the figure are those of the core coordinate system shown in Fig. 7-5. The numbers in the figure indicate the number of steps for progressive demagnetization. (b, d) Schmidt net lower hemisphere projection of the orientation results of eight cut-out specimens. The angles in the figure are measured clockwise with the reference line on the core sample set at 0°. Triangles are the average orientation of the eight specimens and circles are the α_{95} confidence limits.

Black circles and black open circles project the endpoints of the remanent

magnetization vectors obtained at each demagnetization step from three-dimensional space onto the x_1x_2 and x_1x_3 planes. The solid straight line in the figure is an approximate line for the primary remanent magnetization component. The angle between the approximate line to the black circle and the x_1 axis is the declination angle, and the angle between the approximate line to the white circle and the x_1 axis is the inclination angle. Light black and white circles indicate secondary remanent magnetization components.

Fig. 7-10 (b) shows the results of the remanent magnetization measurements for eight specimens cut out of FDB-12 and projected into a Schmidt net in the lower hemisphere. The triangles represent the averaged orientation of the eight specimens, and this averaged orientation was used for the orientation of the samples. The circle in the figure represents the 95% confidence limit angle α_{95}.

Table 7-2 shows the results of the reorientation of each sample. The measurement accuracy (Rank) of the remanent magnetization was determined by applying a statistical treatment to the remanent magnetization orientation of eight specimens cut from a single core sample. Details are described in Chapter 4. The treatment of a sample with a Rank B is decided based on the significance of the sample and other factors. In this study, each rock core sample was considered to be of high importance because they are representative of the depth where the samples are retrieved, and we decided to use samples with a Rank of up to B to determine the direction of the principal stress.

Table 7-2 Results of reorientation.

Sample ID	Declination (°)	Inclination (°)	Azimuth for ASR (°)	α_{95} (°)	Rank
FDB-11	208.9	10.1	208.9	3.4	A
FDB-12	54.4	63.4	54.4	10.3	B
FDB-13	358.7	44.9	358.7	5.7	B
FDB-16	38.0	-51.7	218.0	37.0	B
FDB-17	52.5	-1.5	232.5	2.6	A
FDB-19	91.2	40.7	91.2	5.8	B

The two samples shown in Fig. 7-10 (FDB-12, 19) are both Rank B samples. For FDB-16 and FDB-17, the inclinations are negative in both cases. The reason for this is that the two samples were taken from reversed polarity intervals. FDB-16 is a conglomerate, and each conglomerate that makes up the sample could have a different remanent magnetization direction. However, since the remanent magnetization is relatively coherent, with an α_{95} of 37.0° obtained from eight specimens, the remanent magnetization was evaluated to point to the current true south direction. For such a sample, since the remanent magnetization vector points to the current true south, we use the value of the declination plus 180° to perform the reorientation. Azimuth for ASR in Table 7-2 represents the angle between true north and the reference line of the core sample, and the value of declination is used for positive inclination and 180° plus declination for negative inclination.

Using the results of reorientation, the direction of the principal strain is transformed from the core coordinate system to a geographic coordinate system and projected into a Schmidt net in the lower hemisphere, as shown in Fig. 7-11. Since the directions of principal strains coincide with the directions of principal stresses, these figures represent the direction of principal stresses. Each Schmidt net describes not only the three principal stress directions, but also the maximum and minimum horizontal principal stress directions. For all samples except FDB-11, the maximum principal

stresses were almost vertical, and the directions of the maximum horizontal stresses were NNE-SSW to ENE-WSW, which were almost parallel to the strike of the Futagawa Fault (N60°E) at this study site. The samples in FDB-11 and FDB-17 are andesite conglomerates in the conglomerate phase, and the elastic moduli of the core samples are considered to be significantly different from those of the surrounding substrate. Therefore, the measured stresses are considered to be representative of the conglomerate's condition and not of its stress state. Thermal remanent magnetization records the direction of the magnetic field at the moment the rock reaches a temperature below the Curie point.

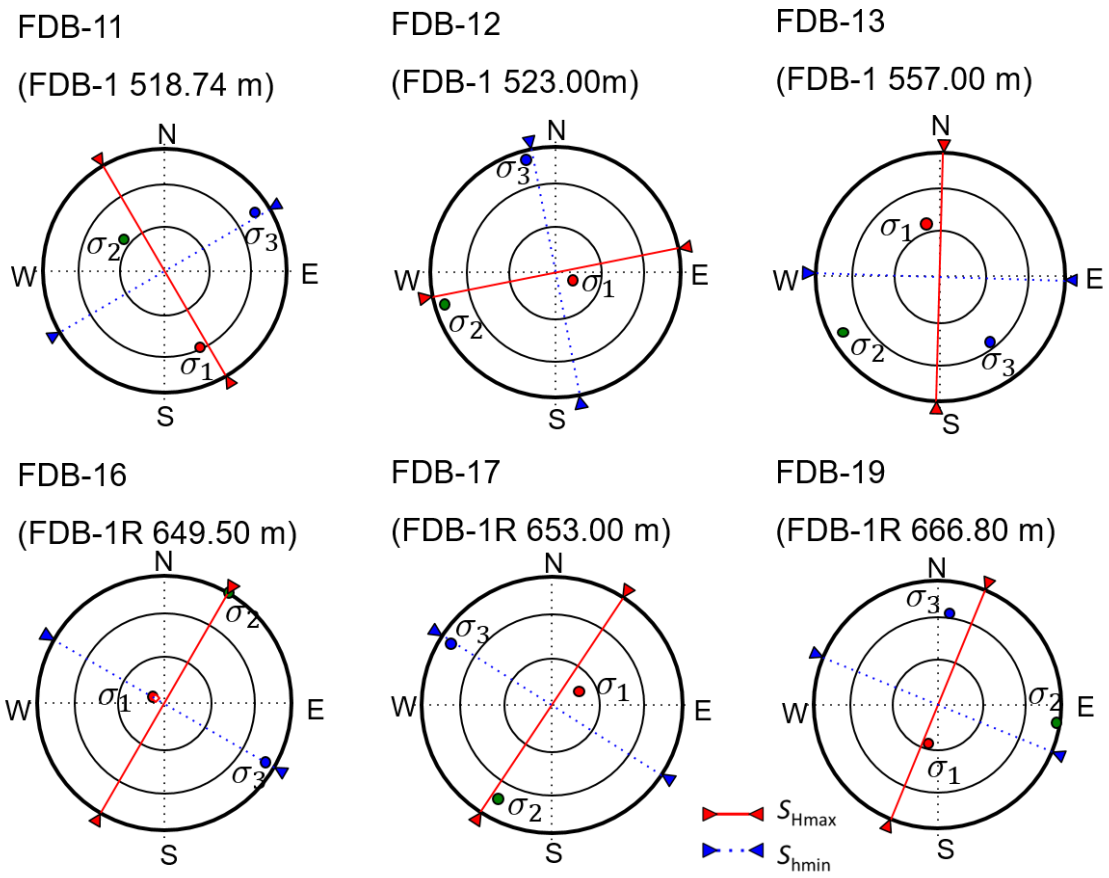

Fig. 7-11 Projection of the principal stress directions. Schmidt net lower hemisphere projection is shown. The three principal stresses and the maximum and minimum horizontal stresses are described in the figure.

Therefore, FDB-11 and FDB-17, which are andesite conglomerates in the conglomerate,

would have been affected by the original magnetization of the conglomerates if they had not been heated above the Curie point during deposition and it was possible that the orientation of the earth's magnetic field was not properly evaluated. However, in this study, all samples except FDB-11 show a similar trend in the direction of principal stresses, suggesting that they have been successfully reoriented.

7.5.3 Magnitudes of principal stresses

The magnitudes of principal stresses were determined according to the method described in Chapter 3.

The vertical stress σ_{v} was assumed to be equal to the overburden stress calculated from the average density of the rocks above the measurement point (sampling depth), and $\sigma_{\mathrm{v}} = \rho_{\mathrm{r}}\, gh$. The pore pressure p_0 was assumed to be equal to the hydrostatic pressure, and $p_0 = \rho_{\mathrm{w}}\, gh_{\mathrm{w}}$. $g = 9.8\ \mathrm{m/s^2}$ is the gravitational acceleration, h is the depth of the measurement point, h_{w} is the distance between the measurement point and the groundwater surface, and ρ_{r} and ρ_{w} are the average density of the rock and the density of water, respectively. In this study, $\rho_{\mathrm{w}} = 1.0 \times 10^3\ \mathrm{kg/m^3}$ and the average density was set to $\rho_{\mathrm{r}} = 2.3 \times 10^3\ \mathrm{kg/m^3}$ based on density measurements by the buoyancy method (about 300-660 m, 45 samples) (Sano et al., 2019). The ideal water level for the pore pressure calculation was that at the time of sample stress relief (at the time of drilling), but it was difficult to obtain the exact groundwater level at the time of drilling. In the FDB, groundwater levels have been measured for about two years after the completion of the drilling, and it has been reported that the groundwater level ranges from 41 to 44 m in depth32). Because the FDB boreholes were drilled during the dry season (January-March), the pore pressure was determined using a value of 44 m, where the groundwater level is relatively low.

The magnitudes of principal stresses calculated on the basis of the above conditions are shown in Table 7-3. The values of the overburden stress and hydrostatic pressure used to calculate the principal stresses are also shown in the table. The results show that the maximum principal stress (σ_1) ranges from 11.9 MPa to 16.5 MPa, the

intermediate principal stress (σ_2) from 9.6 MPa to 14.7 MPa, and the minimum principal stress (σ_3) from 8.5 MPa to 11.0 MPa. The horizontal differential stress $S_{\mathrm{Hmax}} - S_{\mathrm{hmin}}$ ranged from 0.5 MPa to 4.7 MPa.

Table 7-3 Magnitudes of stresses.

Sample ID	Depth (m)	σ_V (MPa)	p_0 (MPa)	σ_1 (MPa)	σ_2 (MPa)	σ_3 (MPa)	S_{Hmax} (MPa)	S_{hmin} (MPa)	S_{Hmax}-S_{hmin} (MPa)	Stress Regime
FDB-11	518.74	11.7	4.7	13.4	11.3	8.5	12.8	8.7	4.1	Strike slip faulting
FDB-12	523.00	11.8	4.7	11.9	9.6	8.5	9.7	8.6	1.1	Normal faulting
FDB-13	557.00	12.6	5.0	13.6	11.6	10.7	11.9	11.4	0.5	Normal faulting
FDB-16	649.50	14.6	5.9	15.2	14.7	10.1	15.1	10.4	4.7	Normal faulting
FDB-17	653.00	14.7	6.0	15.9	14.5	11.0	15.5	11.3	4.2	Normal faulting
FDB-19	666.80	15.0	6.1	16.5	10.2	9.4	10.8	10.2	0.6	Normal faulting

The southeast side of the FDB was hilly and the topography could affect the results of the stress measurements. However, the largest difference in height was about 120 m within a 500 m radius around the borehole and the depths at which the stress measurements were successful were greater than about 520 m. This suggests that the topography did not significantly affect the measured stress results at the measurement depths of this study.

7.6 In-situ stress state after 2016 Kumamoto earthquake sequence

The results of the in-situ stress measurements in this study were obtained using samples collected between January 2018 and March 2018. Thus, the resulting stress tensor is about 2 years after the earthquake.

The ASR results show that the maximum principal stress (σ_1) was approximately vertical in the 523-667 m depth range. In-situ stress measurements have been conducted in FDB boreholes using hydraulic fracturing method at a depth of 400 m (Kyoto University, 2018). The results of the hydraulic fracturing tests at 411.5 m and 431.6 m showed that the maximum principal stresses were directed in the vertical direction.

These results indicate that the normal faulting stress regime was dominant in the section of 412-667 m depth around the Futagawa Fault. The surface ruptures, which occurred at the time of the 2016 Kumamoto earthquake's main shock, were found to be purely right-lateral, with a maximum displacement of 2.2 m (Shirahama et al., 2016) and almost no vertical displacement was observed at the study site. Therefore, it is suggested that the maximum horizontal principal stress (σ_1) was significantly reduced with the earthquake, although the strike-slip faulting regime was dominant before the earthquake in this study area. The fact that the post-seismic stress state was of the normal faulting stress regime, as revealed by this study, supports this interpretation. Furthermore, this study found that the maximum principal stress (σ_1), which was horizontal before the earthquake, was less than the vertical stress (intermediate principal stress (σ_2) before the earthquake) governed by the density of the formation after the earthquake.

The results of the normal faulting stress regime after the earthquake and the

change in the stress state from the strike-slip faulting stress regime to the normal faulting stress regime before and after the earthquake were also confirmed by the focal mechanism analysis at the hypocenter depth (Mitsuoka et al., 2020; Yoshida et al., 2016; Yu et al., 2019). In this study, these results were also confirmed by stress measurements using the ASR method.

In all samples except FDB-11, the minimum horizontal principal stress (S_{hmin}) in the horizontal plane was oriented in the NNW-SSE to WNW-ESE direction, which was almost orthogonal to the strike of the Futagawa Fault (N60°E) at this survey site. In other words, results of horizontal principal stress measurements made about two years after the 2016 Kumamoto earthquake suggest that the shear stresses that cause strike-slip on the Futagawa Fault plane were small. This result is also consistent with the post-seismic stress state determined by Yoshida et al. (2016) and Yu et al. (2019). As pointed out by Yu et al. (2019), the direction of the minimum principal stress (σ_3) was subparallel to the N-S direction, which is the expansion direction of the Okinawa Trough (Tada, 1985). These results indicate that the post seismic stress state in relatively shallow areas, obtained by the ASR method, was dominated by the same stress state as the regional stress field inferred from the focal mechanism analysis and the plate motion. These results suggest that the same changes in stress state occurred in the shallow part as in the deep part, which is determined by the focal mechanism analysis.

7.7 Results obtained by the novel analysis procedure

In this section, results of the application of the novel analysis procedure proposed in Chapter 5 to the measurement data collected from the FDB samples are described.

7.7.1 Prior information

The prior information used was the same as in Case-2 described in Chapter 5. The values of vertical stress σ_{v} and pore pressure p_0 used in the analysis of each sample are listed in Table 7-3.

Because there were no measured elastic moduli for FDB samples, in this study, the elastic moduli were calculated using the longitudinal elastic velocities V_P and the Poisson's ratio ν as follows.

First, the transverse wave velocity V_S is calculated based on the relation between the ratio of elastic wave velocity and Poisson's ratio

$$\frac{V_P}{V_S} = \sqrt{2\frac{1-\nu}{1-2\nu}}. \tag{7-1}$$

The elastic moduli of the rock core sample were determined by substituting the calculated transverse wave velocity and the measured longitudinal wave velocity into the equations

$$\begin{aligned} K &= \rho\left(V_{\mathrm{P}}^2 - \frac{4}{3}V_{\mathrm{S}}^2\right) \\ G &= \rho V_{\mathrm{S}}^2 \end{aligned} \tag{7-2}$$

The longitudinal velocity V_P was obtained by sonic logging (Kyoto University, 2018). The Poisson's ratio ν was set to 0.25 based on literature values (Schön, 2015).

7.7.2 Results of inference

The inference results are shown in Table 7-4 to Table 7-8. The tables show the results for both converged and non-converged results. The results show that the MCMC simulation converged for four samples, FDB-11, 13, 16, and 19, while FDB-12 and FDB-17 did not converge according to the convergence method in Chapter 5 because $\hat{R} \geq 1.1$ for some parameters.

Table 7-4 Inference results (Part 1).

Sample ID	σ_{11} [MPa]				σ_{22} [MPa]				σ_{33} [MPa]				σ_{12} [MPa]				σ_{13} [MPa]				σ_{23} [MPa]			
	Mean	2.5%	97.5%	Rhat	Mean	2.5%	97.5%	Rhat	Mean	2.5%	97.5%	Rhat	Mean	2.5%	97.5%	Rhat	Mean	2.5%	97.5%	Rhat	Mean	2.5%	97.5%	Rhat
FDB-11	8.87	2.83	15.08	1.03	9.25	3.24	15.46	1.03	9.28	3.26	15.48	1.03	0.00	0.00	0.00	1.00	0.25	0.23	0.26	1.00	0.00	0.00	0.00	1.00
FDB-12	8.73	5.30	14.78	1.19	8.33	4.89	14.37	1.19	10.15	6.70	16.17	1.19	0.10	0.08	0.12	1.01	0.13	0.11	0.15	1.19	0.23	0.22	0.26	1.14
FDB-13	2.85	0.09	8.46	1.02	9.31	5.16	13.92	1.01	16.91	9.53	24.14	1.00	0.07	0.00	0.24	1.00	0.68	0.05	1.82	1.01	0.04	0.00	0.18	1.00
FDB-16	10.51	4.08	17.19	1.01	10.67	4.23	17.34	1.01	11.83	5.40	18.54	1.01	0.00	0.00	0.00	1.00	0.66	0.63	0.70	1.01	0.20	0.18	0.22	1.01
FDB-17	7.94	2.05	16.64	1.54	8.41	2.53	17.12	1.54	8.55	2.67	17.27	1.54	0.08	0.07	0.09	1.00	0.09	0.08	0.10	1.00	0.00	0.00	0.01	1.00
FDB-19	11.93	6.13	18.21	1.03	12.21	6.42	18.49	1.03	14.48	8.68	20.76	1.03	0.00	0.00	0.00	1.00	0.00	0.00	0.00	1.00	1.45	1.43	1.48	1.00

Table 7-5 Inference results (Part 2).

Sample ID	p_0 [MPa]				τ_V [h]				τ_S [h]				s [10^{-12}]			
	Mean	2.5%	97.5%	Rhat	Mean	2.5%	97.5%	Rhat	Mean	2.5%	97.5%	Rhat	Mean	2.5%	97.5%	Rhat
FDB-11	7.13	1.12	13.37	1.03	8.42	7.82	9.04	1.00	11.62	8.33	15.80	1.00	125.46	118.12	132.99	1.00
FDB-12	4.41	0.97	10.45	1.19	11.27	10.93	11.60	1.01	8.62	7.62	9.36	1.17	212.63	203.80	226.89	1.21
FDB-13	7.66	3.48	12.05	1.01	12.74	11.85	13.67	1.00	0.71	0.63	0.88	1.00	249.74	236.05	264.99	1.00
FDB-16	8.73	2.28	15.40	1.01	17.26	16.15	18.46	1.00	7.64	6.77	8.60	1.01	114.99	108.20	122.56	1.00
FDB-17	6.36	0.48	15.06	1.54	8.77	8.28	9.28	1.00	14.79	11.90	18.16	1.00	49.81	46.90	52.84	1.01
FDB-19	6.56	0.78	12.85	1.03	16.18	15.82	16.53	1.00	16.51	15.69	17.39	1.00	171.59	161.62	181.41	1.00

Table 7-6 Inference results for the maximum principal stress.

Sample ID	σ_1															
	Magnitude [MPa]				n_x				n_y				n_z			
	Mean	2.5%	97.5%	Rhat	Mean	2.5%	97.5%	Rhat	Mean	2.5%	97.5%	Rhat	Mean	2.5%	97.5%	Rhat
FDB-11	9.39	3.38	15.60	1.03	0.38	-0.43	0.45	1.00	0.00	-0.02	0.02	1.00	-0.91	-0.92	-0.89	1.00
FDB-12	10.19	6.75	16.22	1.19	-0.11	-0.12	-0.10	1.03	0.12	0.11	0.13	1.16	0.99	0.98	0.99	1.23
FDB-13	16.96	9.54	24.19	1.00	0.03	-0.07	0.10	1.01	0.00	-0.02	0.01	1.01	-1.00	-1.00	-0.99	1.01
FDB-16	12.13	5.69	18.83	1.01	-0.39	-0.40	-0.38	1.00	0.05	0.04	0.06	1.00	0.92	0.91	0.92	1.00
FDB-17	8.56	2.68	17.28	1.54	-0.14	-0.16	-0.12	1.00	0.10	-0.12	0.16	1.01	-0.98	-0.99	-0.98	1.00
FDB-19	15.19	9.39	21.48	1.03	-0.44	-0.44	-0.44	1.00	0.00	0.00	0.00	1.00	-0.90	-0.90	-0.90	1.00

Table 7-7 Inference results for the intermediate principal stress.

Sample ID	σ_2															
	Magnitude [MPa]				n_x				n_y				n_z			
	Mean	2.5%	97.5%	Rhat	Mean	2.5%	97.5%	Rhat	Mean	2.5%	97.5%	Rhat	Mean	2.5%	97.5%	Rhat
FDB-11	9.25	3.24	15.46	1.03	0.00	0.00	0.00	1.00	0.89	-1.00	1.00	1.00	-0.01	-0.03	0.00	1.00
FDB-12	8.74	5.30	14.78	1.19	0.98	0.97	0.98	1.00	-0.17	-0.21	-0.13	1.01	0.13	0.12	0.14	1.09
FDB-13	9.31	5.16	13.92	1.01	0.00	-0.03	0.02	1.01	0.59	-1.00	1.00	1.02	-0.01	-0.02	0.00	1.00
FDB-16	10.66	4.22	17.33	1.01	0.17	0.15	0.20	1.00	-0.98	-0.98	-0.97	1.00	0.12	0.11	0.14	1.00
FDB-17	8.42	2.54	17.13	1.54	-0.15	-0.18	-0.13	1.00	-0.84	-0.99	0.98	1.01	-0.09	-0.14	-0.07	1.00
FDB-19	11.93	6.13	18.21	1.03	0.90	0.90	0.90	1.00	0.00	0.00	0.01	1.00	-0.44	-0.44	-0.44	1.00

Table 7-8 Inference results for the minimum principal stress.

Sample ID	σ_3															
	Magnitude [MPa]				n_x				n_y				n_z			
	Mean	2.5%	97.5%	Rhat	Mean	2.5%	97.5%	Rhat	Mean	2.5%	97.5%	Rhat	Mean	2.5%	97.5%	Rhat
FDB-11	8.75	2.73	14.95	1.03	-0.80	-0.92	0.90	1.00	0.00	-0.01	0.02	1.00	-0.42	-0.45	-0.40	1.00
FDB-12	8.29	4.85	14.33	1.19	-0.19	-0.23	-0.15	1.00	-0.98	-0.98	-0.97	1.00	0.10	0.09	0.11	1.16
FDB-13	2.80	0.02	8.43	1.02	-0.65	-1.00	1.00	1.03	0.00	-0.04	0.02	1.01	-0.05	-0.11	0.00	1.01
FDB-16	10.22	3.79	16.90	1.01	0.90	0.90	0.91	1.00	0.21	0.19	0.23	1.00	0.38	0.36	0.39	1.00
FDB-17	7.91	2.03	16.61	1.54	0.98	0.97	0.98	1.00	-0.11	-0.16	0.16	1.01	-0.15	-0.17	-0.13	1.00
FDB-19	11.50	5.71	17.78	1.03	0.00	-0.01	0.00	1.00	-0.15	-1.00	1.00	1.00	0.00	0.00	0.00	1.00

Fig. 7-12 shows the lower hemisphere equal area projections of principal stresses obtained from each sample.

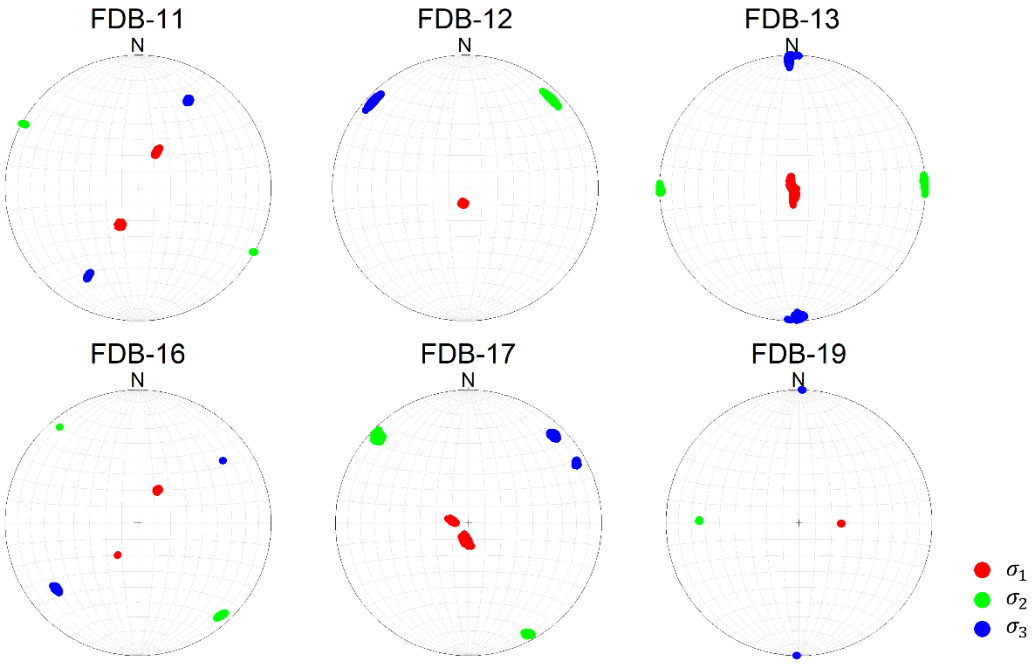

Fig. 7-12 Lower hemisphere equal area projection of the three principal stresses of each sample.

7.8 Summary

In this study, stress measurements were performed in the vicinity of the Futagawa Fault, which was the source fault of the 2016 Kumamoto earthquakes, using ASR method. The in-situ stress state obtained in this study is about two years after the earthquakes. The results show that a normal faulting stress regime, in which the maximum principal stress (σ_1) is oriented vertically, is dominant in the vicinity of the Futagawa Fault after the earthquakes. It is suggested that the maximum principal stress (σ_1), which was in the horizontal plane before the earthquake, was significantly reduced by the fault motion during the earthquake. The results obtained in this study support the hypothesis that the dominant post-seismic stress state is of normal faulting stress regime. It is necessary to continue to measure stress in the source region by using various methods that are complementary to each other, because there is no definitive stress measurement method at present.

References

Asano, K., & Iwata, T. (2016). Source rupture processes of the foreshock and mainshock in the 2016 Kumamoto earthquake sequence estimated from the kinematic waveform inversion of strong motion data. *Earth, Planets and Space*, *68*(147). https://doi.org/10.1186/s40623-016-0519-9

Butler, R. F. (1992). *Paleomagnetism: magnetic domains to geologic terranes*. *Paleomagnetism: magnetic domains to geologic terranes*. Boston: Blackwell Scientific Publications. https://doi.org/10.5860/choice.29-5708

Hardebeck, J. L. (2004). Stress triggering and earthquake probability estimates. *Journal of Geophysical Research: Solid Earth*, *109*(B4). https://doi.org/10.1029/2003JB002437

Hardebeck, J. L. (2012). Coseismic and postseismic stress rotations due to great subduction zone earthquakes. *Geophysical Research Letters*, *39*(21). https://doi.org/10.1029/2012GL053438

Hardebeck, J. L., & Hauksson, E. (2001). Crustal stress field in southern California and its implications for fault mechanics. *Journal of Geophysical Research: Solid Earth*, *106*(B10), 21859–21882. https://doi.org/10.1029/2001JB000292

Japan Meteorogilcal Agency. (2016). The 2016 Kumamoto Earthquake -Portal-. Retrieved December 14, 2020, from https://www.jma.go.jp/jma/en/2016_Kumamoto_Earthquake/2016_Kumamoto_Earthquake.html

Kubo, H., Suzuki, W., Aoi, S., & Sekiguchi, H. (2016). Source rupture processes of the 2016 Kumamoto, Japan, earthquakes estimated from strong-motion waveforms. *Earth, Planets and Space*, *68*(161). https://doi.org/10.1186/s40623-016-0536-8

Kyoto University. (2018). FY29 Commissioned for the disaster prevention on nuclear facilities (Dating Analyses of Drilling cores at the Futagawa fault), Technical Report (in Japanese), 208. Retrieved from https://www.nsr.go.jp/nra/chotatsu/yosanshikou/itaku_houkoku_h29.html

Lin, W., Yeh, E. C., Ito, H., Hirono, T., Soh, W., Wang, C. Y., et al. (2007). Preliminary

results of stress measurement using drill cores of TCDP Hole-A: An application of anelastic strain recovery method to three-dimensional in-situ stress determination. *Terrestrial, Atmospheric and Oceanic Sciences*, *18*(2), 379–393. https://doi.org/10.3319/TAO.2007.18.2.379(TCDP)

Lin, W., Conin, M., Moore, J. C., Chester, F. M., Nakamura, Y., Mori, J. J., et al. (2013). Stress state in the largest displacement area of the 2011 Tohoku-Oki earthquake. *Science*, *339*(6120), 687–690. https://doi.org/10.1126/science.1229379

Matsumoto, S., Nakao, S., Ohkura, T., Miyazaki, M., Shimizu, H., Abe, Y., et al. (2015). Spatial heterogeneities in tectonic stress in Kyushu, Japan and their relation to a major shear zone. *Earth, Planets and Space*, *67*(1), 172. https://doi.org/10.1186/s40623-015-0342-8

Matsumoto, S., Yamashita, Y., Nakamoto, M., Miyazaki, M., Sakai, S., Iio, Y., et al. (2018). Prestate of Stress and Fault Behavior During the 2016 Kumamoto Earthquake (M7.3). *Geophysical Research Letters*, *45*(2), 637–645. https://doi.org/10.1002/2017GL075725

Mitsuoka, A., Shito, A., Matsumoto, S., Yamashita, Y., Nakamoto, M., Sakai, S., et al. (2020). Spatiotemporal Change in the Stress State Around the Hypocentral Area of the 2016 Kumamoto Earthquake Sequence. *Journal of Geophysical Research: Solid Earth*, *125*(e2019JB018515). https://doi.org/https://doi.org/10.1029/2019JB018515

Nishiwaki, T., Lin, A., & Lin, W. (2018). Recovery of Stress During the Interseismic Period Around the Seismogenic Fault of the 1995 Mw 6.9 Kobe Earthquake, Japan. *Geophysical Research Letters*, *45*(23). https://doi.org/10.1029/2018GL079317

Sano, T., Lin, W., Shibutani, S., & Hirose, T. (2019). Measurements of thermal properties of core samples for interpreting an abnormal temperature depth profile observed in Futagawa fault drilling. In *AGU Fall Meeting 2019*.

Schön, J. H. (2015). *Physical properties of rocks: Fundamentals and principles of petrophysics*. Elsevier.

Shibutani, S., Lin, W., Sado, K., & Aizawa, A. (2019). Discussion on groundwater flow

around the active Futagawa Fault based on geological structure and physical properties. In *AGU Fall Meeting 2019*.

Shibutani, S., Lin, W., Sano, T., Fujii, M., & Sado, K. (2021). Well logging in a borehole penetrated through an activve fault and porosity estimation from the log data. *15th Japan Symposium on Rock Mechanics*.

Shirahama, Y., Yoshimi, M., Awata, Y., Maruyama, T., Azuma, T., Miyashita, Y., et al. (2016). Characteristics of the surface ruptures associated with the 2016 Kumamoto earthquake sequence, central Kyushu, Japan. *Earth, Planets and Space*, *68*(1), 191. https://doi.org/10.1186/s40623-016-0559-1

Stein, R. S. (1999). The role of stress transfer in earthquake occurrence. *Nature*, *402*(6762), 605–609. https://doi.org/10.1038/45144

Tada, T. (1985). Spreading of the Okinawa Trough and Its Relation to the Crustal Deformation in the Kyushu(2). *Zisin*, *38*(1), 1–12.

Toda, S., Stein, R. S., Reasenberg, P. A., Dieterich, J. H., & Yoshida, A. (1998). Stress transferred by the 1995 Mw = 6.9 Kobe, Japan, shock: Effect on aftershocks and future earthquake probabilities. *Journal of Geophysical Research: Solid Earth*, *103*(B10), 24543–24565. https://doi.org/10.1029/98JB00765

Toda, S., Kaneda, H., Okada, S., Ishimura, D., & Mildon, Z. K. (2016). Slip-partitioned surface ruptures for the Mw 7.0 16 April 2016 Kumamoto, Japan, earthquake. *Earth, Planets and Space*, *68*(1), 188. https://doi.org/10.1186/s40623-016-0560-8

Yoshida, K., Hasegawa, A., Saito, T., Asano, Y., Tanaka, S., Sawazaki, K., et al. (2016). Stress rotations due to the M6.5 foreshock and M7.3 main shock in the 2016 Kumamoto, SW Japan, earthquake sequence. *Geophysical Research Letters*, *43*(19), 10,10-97,104. https://doi.org/10.1002/2016GL070581

Yu, Z., Zhao, D., Li, J., Huang, Z., Nishizono, Y., & Inakura, H. (2019). Stress Field in the 2016 Kumamoto Earthquake (M 7.3) Area. *Journal of Geophysical Research: Solid Earth*, *124*(3), 2638–2652. https://doi.org/10.1029/2018JB017079

Chapter 8

Conclusions

In this study, the conventional analysis technique of ASR data was applied to some real fields including active fault drilling projects at Futagawa Fault ruptured during the 2016 Mw 7.0 Kumamoto earthquake mainshock to investigate stress state in the vicinity of the fault after the earthquake. Next, a novel analysis procedure of ASR (Anelastic Strain Recovery) data based on Bayesian statistical modeling was proposed, and the core sample reorientation method was improved in order to improve the ASR method. The main results of each study are described below.

In Chapter 2, an overview of existing stress measurement methods was given, classifying them into core-based and non core-based methods. We found that each method of stress measurement is applicable only under certain conditions and that there is no universal method for stress measurement. The ASR method is a promising method that can be used complementarily with other stress measurement methods.

In Chapter 3, existing ASR data analysis technique was reviewed, and the ASR method was found to be one of the few stress measurement methods that can determine the three dimensional stress tensors by itself. Existing ASR analysis method determines in-situ stress based on several assumptions that should be verified by measurements and simulations. Further research is needed to verify the validity of these assumptions and the constitutive equations used. In addition, research on quantitative evaluation of the accuracy of measurement results is also desired.

In Chapter 4, improvement of the reorientation method of core samples, which

is necessary when using the core-based method, was described. In order to evaluate the accuracy of the reorientation results, this study proposes a method to cut out nine specimens from a single core sample and measure the remanent magnetization of eight of them in order to evaluate the reliability of the measurement results. In addition, the effects of secondary remanent magnetization due to drilling on core reorientation were examined, and efforts to evaluate data quality were described.

In Chapter 5, a novel analysis method based on Bayesian statistical modeling for the ASR method was proposed. In this chapter, the validity of the method was verified using simulated ASR data. The results show that the uncertainty of the diagonal component of the stress tensor is larger than that of the non-diagonal component. In order to investigate the cause of this, an analysis based on sensitivity analysis was conducted. Sensitivity analysis indicated that there was a certain correlation between the sensitivity of the parameter and the uncertainty of the parameter inference.

In Chapter 6, the results of applying the new analysis method described in Chapter 5 to a real ASR data set obtained from the Nojima Fault drilling project were described. The simulations converged for the data of all core samples, and the results show a similar trend to the inferred results for the simulated ASR data obtained in Chapter 5. The results of stress measurements by borehole breakout and hydraulic fracturing method were compared with the results obtained in this study, and similar results of horizontal maximum stress (S_{Hmax}) were obtained by all three methods. The comparison of the magnitude of minimum horizontal principal stress obtained by the hydraulic fracturing method with the results obtained in this study also shows consistent results. These results indicate that the method can be applied to real ASR data.

In Chapter 7, stress measurements using the conventional ASR method were performed near the Futagawa Fault, one of the source faults of the 2016 Kumamoto earthquakes, and in-situ stress measurements after the earthquake were successfully carried out on six rock core samples including a conglomerate rock. The result that the post-earthquake stress state is the normal faulting stress regime is consistent with the results of stress measurements in the area, which were obtained using hydraulic fracturing and focal mechanism analysis. Furthermore, the direction of the minimum horizontal

principal stress is almost orthogonal to the strike of the Futagawa Fault, indicating that the horizontal shear stress that causes lateral slip on the fault plane is small. The last section describes the application of the novel analysis procedure to the same ASR data used for conventional ASR method in this chapter.

By applying the ASR method, I determined a dominant normal faulting stress regime in the vicinity of the Futagawa Fault ruptured during the 2016 Kumamoto earthquake. In addition, the application of Bayesian statistical modeling to the ASR method provides, for the first time, an effective approach to quantitatively evaluate the uncertainty of the measurement and to significantly improve the reliability of the measurement results. The knowledge gained in this study is expected to contribute to research and practice in various fields of earth engineering such as underground resource development and a wide range of earth sciences such as structural geology.

Ph D. Dissertation

Anelastic Strain Recovery Methods for In-situ Stress Measurements: A novel analysis procedure based on Bayesian statistical modeling and application to active fault drilling

Tatsuhiro Sugimoto

Laboratory of Earth and Resource System,
Department of Urban Management,
Graduate School of Engineering,
Kyoto University

Kyoto University, Room C1–1–118
Kyotodaigaku-Katsura, Nishikyo-ku, Kyoto, 615–8540, Japan
